

**BENCHMARKING AND CHEMICAL DOPING TECHNIQUES FOR  
NANOSCALE GRAPHENE INTERCONNECTS**

A Thesis  
Presented to  
The Academic Faculty

by

Kevin A. Brenner

In Partial Fulfillment  
of the Requirements for the Degree  
Doctor of Philosophy in the  
School of Electrical and Computer Engineering

Georgia Institute of Technology  
May 2013

# **BENCHMARKING AND CHEMICAL DOPING TECHNIQUES FOR NANOSCALE GRAPHENE INTERCONNECTS**

Approved by:

Dr. James D. Meindl, Advisor  
School of Electrical and Computer  
Engineering  
*Georgia Institute of Technology*

Dr. Jeff Davis  
School of Electrical and Computer  
Engineering  
*Georgia Institute of Technology*

Dr. Muhannad Bakir  
School of Electrical and Computer  
Engineering  
*Georgia Institute of Technology*

Dr. Hua Wang  
School of Electrical and Computer  
Engineering  
*Georgia Institute of Technology*

Dr. Hamid Garmestani  
School of Material Science and  
Engineering  
*Georgia Institute of Technology*

Date Approved: March 05, 2013

*To my parents,*

*Jeff and Lori Brenner,*

*And the belief that every generation should have it better than the one before.*

## ACKNOWLEDGEMENTS

This thesis has stemmed from the support of family, long hours with colleagues, and good times with friends. It is a certainty that without their support, this work would have never been possible. I would like to extend my warmest thanks to all who contributed, and the following specific people:

- **Professor James D. Meindl:** An advisor such as you was both a privilege and a rarity. One thing that I have come to value is individuals who have broken the mold of a “PhD,” provide a vision of what is possible, and ultimately become type person that I can admire. Dr. Meindl, you were all three. In regards to my research, you were an incredible force. In regards to where I go from here, you will always be the type of person that I strive to be. Thank you for all that you have done.
- **My Parents and Family:** Jeff, Lori (Splore), and Madison, your support has been the single greatest contributor to this work – thank you for everything you have done. Greg, thank you for always reminding me to have fun. Kim, Erik, Nikki, and Alli, thank you for all of your love and support. Lynn, thank you for always joining us on our getaways. Dave, thank you for always providing a push.
- **My Committee:** Dr. Jeff Davis, Dr. Muhannad Bakir, Dr. Hua Wang, and Dr. Hamid Garmestani, thank you for your time and support in the crafting of this work.
- **My Colleagues:** TJ Beck, Sarah Bryan, Ian Yang, and Rama Ravindran, thank you for all the long hours together that made this work possible. Every single contribution made here has had your hand in it – what a ride!

- **My Friend:** Romeil Sandhu, very few people have been a force in both the “good times with friends” and the “long hours with colleagues” that have made this work possible – you are one of them. Thank you for all the good memories and in crafting our own vision of how to move forward. You’ve seen it all buddy, and one couldn’t ask for more in a friend or a colleague.
- **My Friend:** Wesley Roy, thank you for all the good times we have had together over the years, especially in Auburn, and all those that are still to come. I will always remember the fun we had.
- **Tina Moseley:** Thank you for helping me to work through all the hurdles that it took to get to this point. My understanding is that obtaining a PhD is never meant to be a smooth process, but with your help, the bumps we hit long the way were hardly noticeable.
- **Eli Gomez:** Thank you for all the support.
- **My Crew:** Xavier LeFaucher, Shawn Lankton, and Romeil Sandhu, you guys are the best. There are far too many great memories to mention here – Vegas, Marlow’s, nights on the town – but I will always think back on them. Let’s make sure to keep them coming.
- **The Cleanroom Staff:** Gary Spinner, Devin Brown, Charlie Suh, Vinhy Nguyen, and Erik Woods, thank you for all the support on the fabrication and processing that made this thesis possible.

# TABLE OF CONTENTS

	Page
ACKNOWLEDGEMENTS	iv
LIST OF TABLES	viii
LIST OF FIGURES	ix
LIST OF SYMBOLS AND ABBREVIATIONS	xv
SUMMARY	xix
 <u>CHAPTER</u>	
I      INTRODUCTION	1
1.1 Contributions and Organization of this Thesis	1
1.2 Justification of the Research	4
1.3 Literature Review for Graphene	7
II     BENCHMARKING OF INTRINSIC GNRS	18
2.1 Motivation for the Chapter	18
2.2 Experimental Procedure	19
2.2 Extraction of Resistivity for GNR Sets	22
2.2 Demonstration of Comparable Resistivity to Cu	24
III    BASAL PLANE DOPING	29
3.1 Motivation for the Chapter	29
3.2 Experimental Procedure	30
3.3 Demonstration of Tunable/Complimentary Basal Doping via E-Beam	31
3.4 Demonstration of Tunable/Complimentary Basal Doping via Plasma	34
3.5 Demonstration of the First Chemically Doped P-N Junction	35
3.6 Investigation of P-N Junction Interconnect Waveguides	38

IV	COMPARISON OF BASAL AND DEFECT DOPING	43
	4.1 Motivation for the Chapter	43
	4.2 Experimental Procedure	45
	4.3 Explanation of Basal and Defect Doping Techniques	48
	4.4 Observation of Scaling Trend for Edge Defect Passivation	54
	4.5 Extraction of Doping Efficiencies per Basal and Edge C-Atom	56
V	DEMONSTRATION OF EDGE-DEFECT DOPING	63
	5.1 Motivation for the Chapter	63
	5.2 Experimental Procedure	64
	5.3 Scaling of Edge Doped Interconnects	65
	5.4 Identification of Techniques for In Situ Edge Doping	68
	5.5 Extrapolation and Modeling of Edge Doping	70
VI	PERIPHERAL APPLICATION IN NON-VOLATILE MEMORY	75
	6.1 Motivation for the Chapter	75
	6.2 Experimental Procedure	76
	6.3 Demonstration of Room-Temperature Hysteresis	77
	6.4 Explanation of the Hysteresis Mechanism	79
VII	CONCLUDING REMARKS AND FUTURE RESEARCH	83
	References	88

## LIST OF TABLES

	Page
<b>Table 1</b> Summary of our approach to the chemical doping GNR interconnects	87



## LIST OF FIGURES

	Page
<b>Figure 1</b>	Sources of increasing electrical resistivity of Cu as the interconnect linewidth is scaled below 50 nm. The influence of grain boundary and side wall scattering are illustrated.
	5
<b>Figure 2</b>	Illustration of the contrast between an atomically smooth interconnect edge and LER. LER is indicated by the dark outline and limits the mobility of graphene nanoribbon interconnects. The flow of carriers is indicated with an arrow.
	7
<b>Figure 3</b>	Linear E-k dispersion in graphene at the six corners of the Brillouin Zone. This dispersion gives rise to many of the desirable electrical properties of graphene.
	10
<b>Figure 4</b>	Gated electrical testing of a graphene device. The devices in this thesis are exfoliated onto 300 nm of SiO <sub>2</sub> , which functions as a gate dielectric. As the gate voltage is modulated, the Fermi level is swept through the DOS in the graphene and a minimum conductivity point is clearly visible at V <sub>min</sub> .
	12
<b>Figure 5</b>	Optical image of a monolayer of exfoliated graphene amongst a graphitic debris field on 300 SiO <sub>2</sub> . The lighter region indicates monolayer graphene with darker few-layer graphene to the right.
	19
<b>Figure 6</b>	Raman spectrum of monolayer exfoliated graphene. No D-peak is observable at 1,350 cm <sup>-1</sup> , indicating a pristine basal plane.
	20
<b>Figure 7</b>	Optical image of the four-point contact metallization, post-development, that is patterned using EBL.
	20
<b>Figure 8</b>	SEM image of the four-point contact metallization fingers atop a flake of exfoliated graphene.
	21
<b>Figure 9</b>	Set of ten GNRs in parallel fabricated between the four-point contact metallization. The interconnects are still coated by the

	HSQ etch mask.	21
<b>Figure 10</b>	Setup for the four-point electrical testing that is performed on all graphene devices in this thesis. An excitation current (nA) is injected through the outer fingers and the voltage bias of the graphene channel is read across the inner fingers. This technique removes contact resistance from our measurements.	22
<b>Figure 11</b>	Resistivity of our GNR sets in comparison to previous works. We demonstrate one of the largest experimental collections and some of the lowest resistivities yet shown.	24
<b>Figure 12</b>	Demonstration of comparable resistivity between sub-50 nm GNRs and 1:1 aspect ratio Cu interconnects. The lowest and highest resistivity from each GNR set is extracted using a burnout technique	26
<b>Figure 13</b>	Demonstration of p-type and n-type doping via coating the graphene basal plane with a film of HSQ. (a) Three pristine devices show low intrinsic doping prior to coating. (b) Devices are coated with HSQ, baked, and developed. A strong n-type doping is observed. (c) Devices are coated with HSQ that is heavily cross-linked via e-beam irradiation. A strong p-type doping is observed.	32
<b>Figure 14</b>	SEM image showing a graphene device coated with a 20 $\mu\text{m}$ diameter film of HSQ. The film is patterned using EBL.	33
<b>Figure 15</b>	Demonstration of tunable complimentary doping of graphene via HSQ films on the basal plane. The cross-linking in the HSQ is controlled through the incident irradiation delivered by the EBL. At low cross-linking (low dose), a strong n-type doping is observed. As the cross-linking is increased (higher dose) a smooth transition to strong p-type doping is observed. Error bars indicate doping levels beyond the gate bias of $\pm 100$ V.	34
<b>Figure 16</b>	Demonstration of tunable complimentary improvements in conductance via plasma-induced cross-linking of HSQ films on graphene. Controlling the exposure time to the plasma, the carrier density is tuned from strong n-type to strong p-type,	35

while preserving the mobility in the graphene.

- Figure 17** Structural and chemical changes to the HSQ film during cross-linking. (a) The cage-like network of HSQ with H (tan), O (blue), and Si (black) atoms. (b) Out-gassing of the H with moderate cross-linking. (c) Complete removal of H and collapsing to a dense network-like structure after advanced cross-linking. 36
- Figure 18** Demonstration of the first chemically doped p-n junction in graphene. (a) An SEM of the p-n junction. Two metallization fingers span a region of bare (p-type) graphene and HSQ-coated (n-type) graphene. (c) Gated electrical testing of the device reveals two distinct minimum conductivity points to the left and right of zero gate bias, confirming the formation of a true p-n junction. 37
- Figure 19** Experimental investigation of waveguided interconnects based on p-n junctions in graphene. The interconnect paths (solid arrow) are electrically decoupled (dotted arrow) through the formation of p-n junctions. The p-n junctions are indicated by the lighter stripes of HSQ. Two architectures are presented with a (a) A single p-n junction and (b) with multiple p-n junctions. 40
- Figure 20** Gated electrical testing of the preliminary waveguided interconnects based on p-n junctions. The interconnect path (blue curve) shows a higher drain current with a single minimum conductivity point. The decoupled path (red arrows) shows an order of magnitude reduction in the drain current, and signs of p-n junction formation via the two local minimum conductivity points. 41
- Figure 21** Illustration of NNG and PNG sheets. (a) An NNG sheet has an n-type basal plane from physisorption of molecular hydrogen ( $H_2$ ) and an n-type edge from  $sp^2$  passivation with H. (b) A PNG sheet has an n-type basal plane from physisorption of  $H_2$  and a p-type edge from passivation with O. The O along the edge is provided by a cross-linked film of HSQ along the edge region. 47

- Figure 22** Raman spectrum on the basal plane and edge of graphene sheets. (a) The Raman spectrum verifies monolayer graphene with a defect free basal plane. The edge region displays a D-peak at  $1,350\text{ cm}^{-1}$  indicating defect passivation. (b) Mapping of the positions where the Raman spectrum are taken. A thin film of HSQ is seen along the edge of the PNG sheet. 48
- Figure 23** Gated electrical testing of an NNG and PNG sheet. (a) The NNG sheet exhibits a strong n-type doping resulting in a shift of  $V_{\min}$  by  $-35\text{V}$  from its pristine value. (b) The PNG sheet exhibits a suppressed n-type doping resulting in a shift of  $V_{\min}$  by only  $-8\text{V}$  from its pristine value. The suppressed doping for the PNG sheet is attributed to the p-type doping from the edge. 49
- Figure 24** SEM image of a PNG sheet. An HSQ strip with  $200\text{ nm}$  overlap is clearly visible along the sheet edge. The HSQ is used to transition the edge doping to p-type doping. 50
- Figure 25** Demonstration of NNG and PPG functionality on the same graphene sheet. (a) Gated electrical testing reveals low intrinsic doping in the pristine sheet. Upon converting the sheet to NNG, a negative shift of  $V_{\min}$  by  $-25\text{ V}$  is observed, indicating n-type doping. Upon converting the NNG sheet to a PNG sheet, a positive shift of  $V_{\min}$  by  $13\text{ V}$  is observed, indicating p-type doping from the edge. (b) SEM image of the NNG sheet. (c) SEM image of the same sheet after being transitioned to PNG. 51
- Figure 26** Initial observation of the scaling trend associated with edge doping. The ask-cleaved graphene flakes have an intrinsic n-type edge doping (due to H-passivation from the ambient environment) and a p-type basal plane (from physisorption and process residue). As the width of the graphene flake is decreased, a transition from p-type devices to increasingly stronger n-type devices is observed as the edge begins to dominate the carrier density. 56
- Figure 27** Extraction of the carriers donated per C-atom in the graphene lattice for vacancy defect passivation and physisorption. Based on the experimentally observed shift of  $V_{\min}$  for multiple NNG and PNG sheets, a curve representing all pairs of  $\chi_E$  and  $\chi_B$  that could produce the observed doping level in the sheet are

plotted. NNG sheets are plotted for the experimentally observed shifts from -40 to -28 V, with the mean falling at -34 V. PNG sheets are plotted for experimentally observed shifts from -15 to -3 V, with the mean falling at -9 V. The intersection of the NNG and PNG curves, outlined in bold, represents the possible values for  $\chi$ . The true values for  $\chi_E$  and  $\chi_B$  are taken as the intersection of the mean curves, marked with a dot. It is found that charge donation for physisorption atop a basal atom is on the order of  $5.5 \times 10^{-4}$  carriers per C-atom and 0.85 carriers per C-atom for edge atoms. This indicates that edge atoms, or C-atoms residing adjacent to vacancy defects, are over three orders of magnitude more efficient than basal plane atoms as a route towards chemical doping. 60

**Figure 28** Gated electrical testing of two graphene sheets exfoliated in a nitrogen-rich environment. Having the dopant specie present as the interconnect is freshly cleaved results in efficient passivation of the edge. (a) Testing of the two devices reveals two different levels of n-type doping. (b) SEM imaging reveals that the narrower of the two sheets exhibits a larger n-type doping. 66

**Figure 29** Raman spectroscopy of a graphene sheet exfoliated in a  $N_2$  glovebox reveals a pristine basal plane. No D-peak is observed, indicating a basal plane free of defects. 66

**Figure 30** Experimental verification of the scaling trend associated with edge doped interconnects. (a) Gated electrical testing of multiple interconnects with varying linewidth. (b) A plot of the carrier density of these devices versus the interconnect width reveals increasing n-type doping with scaled dimensions. Positive values of the carrier density represent n-type carriers. 67

**Figure 31** Modeling of the scaling trend for the carrier density in efficiently edge doped GNRs. 71

**Figure 32** Resistivity scaling of intrinsic and edge doped GNRs based on simplified graphene models. The onset of LER-limited mobility is applied at linewidth below 50 nm. Edge doped GNRs show orders of magnitude lower resistivity than intrinsic GNRs, while outperforming Cu for a narrow window of linewidth. 73

**Figure 33** Demonstration of a non-volatile graphene memory device. (a) Gated electrical testing of a pristine graphene sheet atop an SiO<sub>2</sub> dielectric reveals no hysteresis. Pulsed-gate testing is used to remove charge trapping in adsorbates. (b) An overlying screening dielectric is applied and a room-temperature hysteresis of nearly one order of magnitude is observed. 78

**Figure 34** Explanation of the mechanism of hysteresis. (1) At large positive values of the gate voltage, electrons are emitted from the graphene channel and embed at shallow depths in the underlying gate dielectric. (2) These embedded electrons disrupt the dielectric screening process, and function as charged impurities working to lower the conductivity. (3) At large negative values of the gate voltage, the electrons are released from the oxide. (4) Once the electrons are released, a return to the high conductance state is observed. 81

## LIST OF SYMBOLS AND ABBREVIATIONS

2D	Two-Dimensional
2DEG	Two-Dimensional Electron Gas
3D	Three-Dimensional
$\chi_B$	Charge Donation Efficiency for Basal C-Atoms
$\chi_E$	Charge Donation Efficiency for Edge C-Atoms
$e$	Elementary Charge
$h$	Planck Constant
K	Dielectric Constant
$k_F$	Fermi Wave Vector
$\lambda$	Thomas-Fermi Screening Length
$\mu$	Carrier Mobility
$n$	Carrier Density
$n_B$	Carrier Density from Basal C-Atoms
$n_E$	Carrier Density from Edge C-Atoms
$n_i$	Impurity Density
$n_{\text{sheet}}$	Carrier Density from Basal and Edge C-Atoms

$\rho$	Electrical Resistivity
$\rho_{3D}$	3D Electrical Resistivity
$\sigma$	Electrical Conductivity
AFM	Atomic Force Microscopy
AR	Interconnect Aspect Ratio
$atoms_B$	Number of C-atoms on the basal plane of a graphene sheet
$atoms_E$	Number of C-atoms along the edge of a graphene sheet
BEOL	Back End of the Line
$C_{line}$	Interconnect Line-to-Line Capacitance
CMOS	Complimentary Metal Oxide Semiconductor
CNT	Carbon Nanotube
$C_{ox}$	Oxide Capacitance
CVD	Chemical Vapor Deposition
$d_{int}$	Interfacial Spacing between Graphene and the Dielectric
DMF	Dimthylformamide
DOS	Density of States
EBL	Electron Beam Lithography



$E_{\text{int}}$	Interfacial Electric Field between Graphene and the Dielectric
FEOL	Front End of the Line
$f_T$	Cut-off Frequency
GNR	Graphene Nanoribbon
GR	Graphene Ribbon
HSQ	Hydrogen Silsesquioxane
IC	Integrated Circuit
ILD	Interlayer Dielectric
ITRS	International Technology Roadmap for Semiconductors
JFoM	Johnson Figure of Merit
LER	Line-Edge Roughness
MOSFET	Metal-Oxide-Semiconductor Field-Effect Transistor
NNG	Graphene Sheet with an N-Type Edge and N-Type Basal Plane
PNG	Graphene Sheet with a P-Type Edge and N-Type Basal Plane
SCCM	Standard Cubic Centimeters
$r_c$	Contact Resistance
SEM	Scanning Electron Microscope

STM	Scanning Tunneling Microscope
TEM	Tunneling Electron Microscope
TMAH	Tetramethylammonium Hydroxide
$V_{BD}$	Breakdown Voltage
$V_g$	Value of the Gate Voltage
$V_{min}$	Gate Voltage at the Minimum Conductivity Point

## SUMMARY

The interconnect fabric that provides electrical connectivity to active devices is an essential component to modern semiconductor chips. As the dimensions of these devices are scaled to improve performance and keep pace with Moore’s Law, the local Cu interconnects must scale in parallel. Intrinsic material properties of Cu result in spiking resistivity with scaling and present a looming bottleneck to chip performance.

In this thesis, we introduce graphene as a replacement material to Cu interconnects in support of future chip scaling. In particular, we focus on establishing the fundamental mechanisms for chemically doping graphene, with broad contributions that extend beyond the focus of local interconnects. Our approach is outlined as follows:

- First, we benchmark intrinsic graphene nanoribbon (GNR) interconnects and demonstrate comparable resistivity to Cu at similar linewidth [3,4].
- Second, we develop a non-invasive tunable/complimentary doping technique via the graphene basal plane. This technique is used to demonstrate the first chemically doped p-n junction in graphene [5].
- Third, we use this basal technique to extract the doping efficiency (per C-atom) of surface physisorption and defect passivation in graphene [6].
- Fourth, we demonstrate defect passivation along the edge of graphene interconnects with an advantageous scaling trend [7]. We extrapolate this trend to benchmark “edge doped” graphene interconnects.
- Fifth, we describe a novel mechanism of producing hysteresis in graphene. We leverage this mechanism to demonstrate a non-volatile graphene memory device capable of room-temperature operation [8].

# **CHAPTER 1**

## **INTRODUCTION**

Since the first introduction of an integrated circuit (IC), scaling has defined the success that the microelectronics, and now nanoelectronics, industry has enjoyed. It is this very scaling, typically captured through Moore's Law, which has fostered the introduction of ICs into an incredible variety of technologies including mobile computing, implantable biomedical devices, satellites, and communications. This being said, the significance of providing avenues for the continued scaling of ICs cannot be overstated. Whereas the scaling of front-end-of-the-line (FEOL) transistors results in improvements to system-level performance, the back-end-of-the-line (BEOL) local interconnect fabric becomes more electrically resistive and will ultimately be a bottleneck to future IC scaling [1]. This rapidly increasing resistivity is a result of intrinsic material properties to Cu – the material of choice for local interconnects – and places the forward focus on new materials in replacement of Cu. Fortunately, this is a transition familiar to Complementary Metal Oxide Semiconductor (CMOS) chips as the local interconnects previously underwent a change from Al to Cu [2].

This thesis explores graphene as a replacement material for Cu, with a focus on establishing fundamental chemical doping techniques. The atomically thin sp<sup>2</sup> carbon found in graphene is the first, ever, 2-dimensional (2D) conducting material. As such, graphene requires a departure from traditional chemical doping techniques and a re-inventing of how we dope nanoscale devices; interconnects included. Our approach to chemical doping is outlined below along with the contributions made and conclusions drawn on the scalability of nanoscale graphene interconnects. Peripheral contributions to the realm of non-volatile graphene memory devices are also included.

### **1.1 Contributions and Organization of this Thesis**

We begin this work by providing an experimental benchmarking of the electrical resistivity of intrinsic graphene nanoribbon (GNR) interconnects. The foundation for this thesis was laid through a wealth of theoretical work that demonstrates graphene interconnects can outperform Cu. However, a thorough experimental demonstration of GNR interconnects at linewidth below 50 nm was previously absent.

In Chapter 2 we begin with two experimental demonstrations on intrinsic GNR interconnects with no intentional chemical doping applied [3, 4]. We fabricate GNR with a linewidth between 15 nm and 50 nm and demonstrate comparable electrical resistivity to Cu. In addition, we benchmark the current carrying capacity of these GNRs and demonstrate breakdown current densities nearly three orders of magnitude larger than Cu. Lastly, we show that graphene can be extended to meet its theoretical ( $\text{SiO}_2$  phonon-limited) resistivity of  $\sim 1.2 \mu\Omega\cdot\text{cm}$  through the application of chemical doping.

In Chapter 3, we begin our approach to chemical doping through non-invasive physisorption on the graphene basal plane (surface) [5]. Basal plane techniques have the advantage of not disrupting the crystallinity of the graphene sheet. As such, increases in the carrier density need not necessarily come at the cost of major reductions to mobility, resulting in improved electrical conductivity. Using coatings of Hydrogen Silsesquioxane (HSQ), we demonstrate the first basal doping technique that is complimentary, tunable, and capable of ultrahigh resolution without the need for masking. This technique is used to demonstrate an order of magnitude increase in conductivity for both p-type and n-type carriers. Lastly, this technique is used to demonstrate the first chemically doped p-n junction in graphene.

In Chapter 4, we use the HSQ technique of Chapter 3 to explore the limitations of basal plane doping [6]. To this end, we provide the first direct comparison between two fundamental techniques of chemically doping graphene: (1) surface physisorption and (2) vacancy defect passivation. We demonstrate that the passivation of such defects is over three orders of magnitude more efficient for chemical doping than physisorption, in terms

of carriers donated per available C-atom in the graphene lattice. In addition, we provide the first observation of a scaling trend when passivating naturally occurring defects along the edge of cleaved graphene interconnects - increasing carrier density with reduced dimensions.

In Chapter 5, we experimentally demonstrate “edge doped” graphene interconnects [7]. Motivated by the doping efficiencies identified in Chapter 4 for vacancy defects, we target the passivation of naturally occurring defects along the edge of cleaved graphene. Moreover, we confirm the scaling trend of increased carrier density with reduced dimensions that is inherent to edge doped devices. In regards to edge doping, we present the first indication that edge passivation must combat the C-C edge reconstructions that readily occur the moment the edge is cleaved. The implications of this are two fold: (1) the doping specie must be present at the moment the edge is cleaved/etched and (2) the doping specie must provide an energetically favorable option to C-C edge reconstructions. These are both addressed through the experimental demonstration of in situ edge doping via N-passivation. Lastly, we extrapolate our edge doping to provide an initial benchmarking of edge doped nanoscale graphene interconnects. Specifically, we identify (1) the carrier densities possible via edge doped nanoscale interconnects and (2) the linewidth at which edge doping dominates over basal doping. Through this extrapolation, we provide a preliminary assessment of the electrical resistivity of edge doped graphene interconnects against Cu at sub-50 nm linewidth.

In Chapter 6, we provide peripheral contributions to non-volatile memory devices [8]. While exploring techniques of increasing graphene interconnect conductivity via dielectric screening, we unearthed a novel technique of producing hysteresis in graphene sheets. We leverage this mechanism to experimentally demonstrate a device capable of a room-temperature hysteresis of nearly an order of magnitude; something not possible for previous carbon nanotube (CNT) and graphene floating-gate designs. Additional contributions made are discussed elsewhere [9-11].

Thus, the contributions of this thesis are organized as follows:

- **Chapter 2:** Present the first complete experimental demonstration that intrinsic GNR interconnects can be comparable to Cu resistivity below 50 nm linewidth [3]. Demonstrate breakdown current densities in GNRs three orders of magnitude larger than Cu [4].
- **Chapter 3:** Present a novel basal plane doping technique that is tunable/complimentary and capable of an order of magnitude improvement in both p-type and n-type electrical conductivity. We use this technique to demonstrate the first chemically doped p-n junction in graphene [5].
- **Chapter 4:** Present the first experimental comparison of the chemical doping efficiency of basal plane physisorption and vacancy defect passivation. We demonstrate that the passivation of such defects is three orders of magnitude more efficient, using a metric of carriers donated per available C-atom in the graphene lattice [6]. We present the first experimental observation of a scaling trend for edge defect passivation. This trend exhibits increasing carrier density with reduced interconnect linewidth.
- **Chapter 5:** Present the first efficiently (in situ) edge doped graphene interconnect. We experimentally verify the scaling trend associated with edge doping, and extrapolate this trend to benchmark the resistivity of nanoscale graphene interconnects [7].
- **Chapter 6:** We identify a novel mechanism for tailoring the hysteresis of graphene devices at room temperature. We use this mechanism to experimentally demonstrate a room-temperature non-volatile graphene memory device capable of an order of magnitude hysteresis gap [8].

Additional peripheral contributions that were made to graphene devices are published elsewhere [9-11].

## 1.2 Justification of the Research

The thrust for this research is the necessity of continued scaling in CMOS ICs. Specifically, the scaling of local Cu interconnects faces immediate concerns as their electrical resistivity aggressively increases when the linewidth is scaled below 50 nm [1]. This increasing resistivity is a result of intrinsic material properties of Cu, mainly sidewall and grain boundary scattering. These scattering mechanisms in Cu interconnects are shown in **Figure 1**. Unlike FEOL transistors that can be improved through redesigns of the device (i.e., Intel's transition from planar transistors to FinFETs), the interconnects must undergo a material transition away from Cu to support future IC scaling. It should be noted that before Cu is abandoned, there are a variety of changes that can be made to the local interconnect fabric as a temporary fix, none of which provide a permanent solution for interconnect scaling. These include air-gapped and/or low-K interlayer dielectrics (ILD) [12, 13], thinning of the Cu diffusion barrier [14], and scaling of the capping layer [15]. However, these are only temporary fixes in a CMOS industry that is facing tremendous pressure to chart scaling roadmaps for the next few decades. As such, a transition in the local interconnect material is necessary for the continued scaling of ICs and commercial success of the technology. Fortunately, this transition is familiar to the CMOS industry as the local interconnects previously underwent a change from Al to Cu interconnects in 1997 via IBM/Motorola [2].



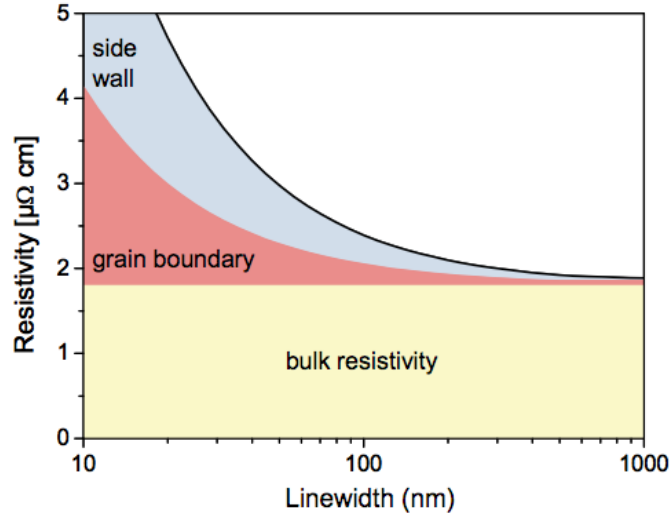


**Figure 1.** Sources of increasing electrical resistivity of Cu as the interconnect linewidth is scaled below 50 nm. The influence of grain boundary and side wall scattering are illustrated [1].

Graphene, the 2-dimensional (2D) and atomically thin allotrope of carbon [16], has garnered tremendous attention as a candidate material for nanoscale electrical conduction devices; interconnects included. The theoretical properties of graphene, which are described in detail below, can overwhelm the electrical performance of metals and semiconductor materials at the local interconnect level [17]. These properties include orders of magnitude improvements in carrier mobility, breakdown current density, and highly prized novel ballistic mechanisms entirely unique to graphene. As such, graphene provides the opportunity to advance electronic devices in a way that no other material can [18], given that an adaption can be made from traditional 3D bulk materials to the 2D graphene sheet.

As graphene sheets are tailored into nanoscale devices, a number of non-idealities set in that deteriorate these theoretical electrical properties of the material. These non-idealities mainly come in the form of scatterers, which can include the substrate [19], charged impurities in the vicinity of the channel [20], and defects in the lattice [21], to

name a few. Specifically regarding the tailoring of graphene sheets into local interconnects, scattering from line-edge-roughness (LER) is by far the most dominate source of degraded performance. Such LER scattering is a result of physical edge roughness in the interconnect and degrades graphene to the point that it can no longer outperform Cu. LER also impacts graphene’s ability to capture applications in transistors, memory, an sensor devices. An illustration of such LER is shown in **Figure 2**. Overcoming LER requires the lithographic patterning of atomically smooth edges. As of now, we do not foresee any reliable techniques of patterning necessarily smooth graphene edges in a CMOS-compatible manner.

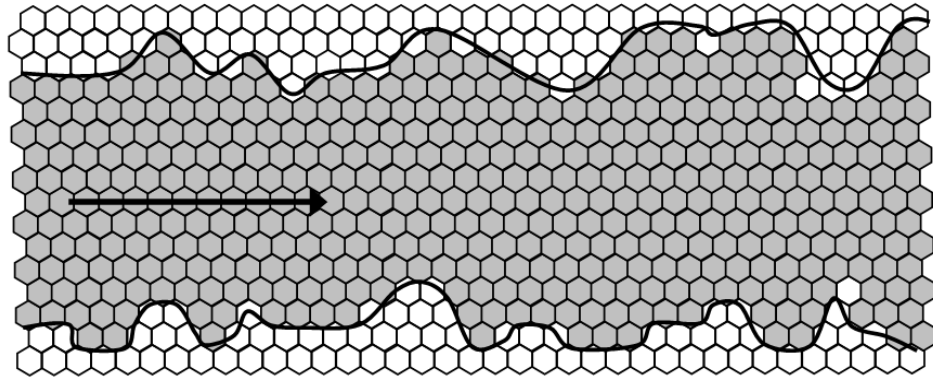


**Figure 2.** Illustration of the contrast between an atomically smooth interconnect edge and LER. LER is indicated by the dark outline and limits the mobility of graphene nanoribbon interconnects. The flow of carriers is indicated with an arrow.

In this thesis, we present fundamental contributions to the chemical doping of graphene sheets with a particular focus on techniques of combating LER in nanoscale graphene interconnects; i.e., bringing graphene closer to its theoretical values. These techniques provide a realizable avenue for displacing Cu at the local interconnect level (along with geometrical/capacitance benefits), furthering IC scaling, and cross-pollinating graphene into other solid state devices based on electrical conduction. As 2D graphene represents a true departure from all other 3D materials, unique even to quasi-2D inversion

layers in Si Metal-Oxide-Semiconductor Field Effect Transistors (MOSFET) and 2D electron gasses (2DEG) in compound semiconductors, a reinventing of traditional bulk chemical doping techniques is necessary. We provide here a benchmarking and solutions for chemically doping graphene into high-conductance nanoscale devices.

### **1.3 Literature Review on Graphene**

The graphene sheet is described as a monolayer of  $sp^2$  carbon arranged in a honeycomb lattice – graphene is a single layer of graphite. The theoretical work on graphene extends back to the 1940's where it was first identified as a rich system for probing novel electrical properties [22]. For over half a century it was thought that the isolation of graphene, as well as other strictly 2D crystals, was thermodynamically impossible as such materials have a tendency to spontaneously “melt” at any finite temperature. This melting was thought to stem from the fact that thermal displacement could exceed the inter-atomic spacing of the lattice itself [23]. Specifically regarding carbon allotropes, it was generally accepted that carbon would form more stable curved structures such as soot and fullerenes. This being said, when the graphene sheet was first isolated in 2004 it generated international excitement as the 2D material was a true departure from any previous 3D bulk material [16]. Graphene would go on to win the Nobel Prize in Physics just six years later in 2010.

Since its isolation, graphene has single handedly provided one of the richest solid state mediums since Si, nurturing ventures into mechanical reinforcements [24], thermal interfaces [25], scaffolds for tissues and bone growth [26], and almost every fundamental electronic device [3, 8, 27, 28]. The immediate application in electronic devices is a result of the phenomenal electrical properties of the material and unique 2D geometry.

These electrical properties will be discussed here in two sections based on the ability to realize them in fabricated devices: (1) theoretical properties and (2) experimental properties. Concerning the theoretical properties of graphene, a detailed discussion is beyond the scope of this thesis as they vanish due to the non-idealities present in actual fabricated devices. However, they are worth mentioning as they provide tremendous motivation to further mature the handling and processing of graphene sheets.

Regarding the theoretical properties of graphene, the linear energy-momentum ( $E-k$ ) dispersion at the edge of the six corners of the Brillouin zone gives rise to carriers that behave as zero rest-mass relativistic Dirac Fermions. These particles propagate at an “effective speed of light” described by the Fermi velocity;  $1 \times 10^6$  m/s, [29]. As such, carriers in graphene can operate under ballistic transport over micron distances, at room temperature, with angle-dependent Klein tunneling at p-n junctions [30]. This angle dependent tunneling can support a variety of novel electronic devices. These include electron lenses, such as the Veselago Lens [31], remarkable electrical transistors and valves [32], and scatter-free waveguided interconnects [33]. The latter was probed experimentally by us and is discussed in further detail in Chapter 3. The band structure of graphene is described as a gapless semimetal where the density of states (DOS) vanishes at the intersection of the conduction and valence band. This is shown in **Figure 3**. As such, the carrier density of graphene can be freely tuned for both p-type and n-type carriers, with potential to make the material electrically insulating when the Fermi level is pinned at the zero DOS position, referred to here as the Dirac point. In addition to this, an artificial band gap (or insulating state) can be engineered in the material through a number of techniques including physical patterning of the graphene [34-37], half

metallicity [38], reversible  $sp^2$ - $sp^3$  conversion [39], or via breaking of the symmetry using perpendicular electrical fields in bilayer graphene [40, 41]. As a crowning touch, graphene also exhibits the largest mechanical strength [24] and thermal conductivity [25] of any known material, opening new avenues for electronic devices designed for harsh environments.

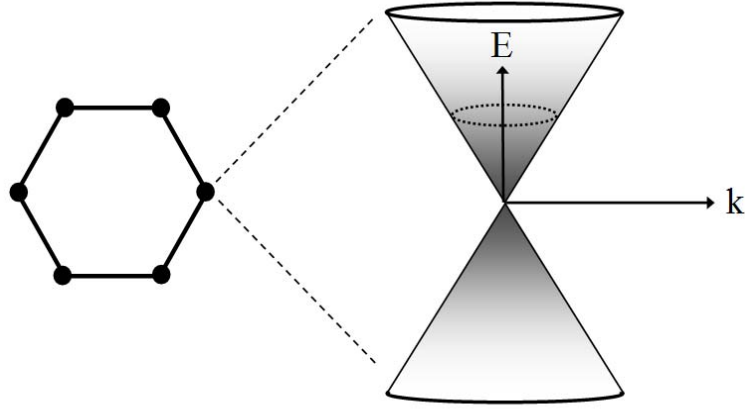


**Figure 3.** Linear E-k dispersion in graphene at the six corners of the Brillouin Zone. This dispersion gives rise to many of the desirable electrical properties of graphene.

Regarding the experimental properties of graphene, a number of impressive demonstrations have paved the way for graphene's application to local interconnects. These experimentally demonstrated properties include room temperature carrier mobilities of  $\sim 200,000 \text{ cm}^2/\text{Vs}$  (over  $1,000\times$  larger than Si) [42], mean-free paths of  $\sim 1\mu\text{m}$  (over  $1,000\times$  larger than Si or Cu) [42], breakdown current densities of up to  $\sim 10^8 \text{ A/cm}$  (more than  $1,000\times$  larger than Cu) [4], and minimal fabrication costs (significantly cheaper than metals or III-V materials) [43]. What separates these experimental properties from the theoretical properties are the non-idealities that set in for fabricated devices, washing out the more exotic properties of graphene. These non-idealities typically come in the form of scatterers, which limit the mobility and disrupt the ballistic

path of carriers. In graphene interconnects with linewidth *larger* than 50 nm, these scatterers come from a variety of intrinsic and extrinsic sources [19]. These can take the form of process residue or oxide charge trapped below the graphene [44], phonons from the substrate [19], charged impurities in the vicinity of the channel due to adsorbates [20], and defects in the lattice due to the growth process or electron irradiation from patterning and imaging [45].

The Dirac point, where the DOS vanishes at the intersection of the bands, is of particular interest in fabricated graphene devices. Experimentally, the insulating state where the Fermi level is pinned at the Dirac point cannot be reached. This is the result of two primary non-idealities. First, any finite temperature will promote electrons to the conductance band since graphene is a gapless semimetal. Second, electron and hole “puddles” exist in the material, which readily conduct via inter-band tunneling [46, 47]. The implications of this are that when the Fermi level is pinned in the vicinity of the Dirac point, a minimum conductivity point can be observed – it has a significantly higher resistance yet is far from electrically insulating. In gated graphene devices, the gate bias at which the minimum conductivity point is observed ( $V_{\min}$ ) is a powerful tool for determining the carrier density. Specifically, the position of  $V_{\min}$  is an indicator of the displacement of the Fermi level from the Dirac point, and is related to the carrier density through the expression

$$C_{ox} \cdot V_{\min} = n \cdot e \quad (1)$$

where  $C_{ox}$  is  $11.6 \text{ nF cm}^{-2}$  for the 300 nm  $\text{SiO}_2$  dielectric used in this thesis. When the gate bias is varied, the Fermi level is swept through the DOS and a V-shaped curve (clearly indicating  $V_{\min}$ ) results. Throughout this thesis, the displacement of  $V_{\min}$  from

zero gate bias is then used to determine the carrier density in the material. A representative V-shaped curve resulting from gated electrical testing of a graphene device is shown in **Figure 4**. Conductance of the devices in this thesis is expressed in regards to quantum conductance,  $e^2/h$ , where  $e$  is the elementary charge and  $h$  is the Planck constant.

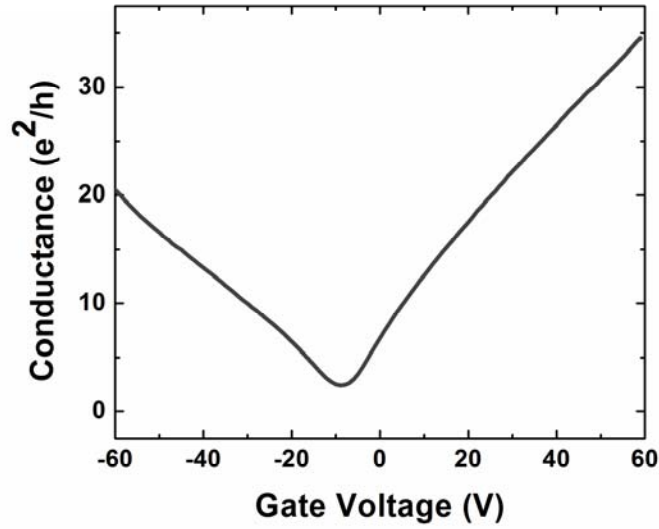


**Figure 4.** Gated electrical testing of a graphene device. The devices in this thesis are exfoliated onto 300 nm of  $\text{SiO}_2$ , which functions as a gate dielectric. As the gate voltage is modulated, the Fermi level is swept through the DOS in the graphene and a minimum conductivity point is clearly visible at  $V_{\text{min}}$ .

A distinct advantage of graphene sheets for CMOS, especially in contrast to CNT, is the available techniques by which the material can be synthesized. Since the first isolation of graphene debris using a mechanical exfoliation technique [16], a number of cost-effective and CMOS-compatible techniques have emerged for the wafer-scale synthesis of graphene. The most promising of these techniques take the form of graphene synthesis on metallic films. More specifically, the synthesis of graphene directly on Cu surfaces has shown tremendous promise for commercialization of the material. These

synthesis techniques are driven by the poor solubility of C within Cu. As such, single-crystal graphene sheets can be synthesized on Cu templates using standard chemical-vapor deposition (CVD) processes [48-50], solid carbon feedstock [51], and trace carbon within the metal itself [52]. Given the tight thermal budget of CMOS process, synthesis on Cu can even support near-room temperature growth [53]. Once grown, these graphene sheets can be coated with a supporting polymer, freed from the Cu using a chemical etch, and transferred to an arbitrary substrate for the formation of interconnect tiers [49, 50]. If the Cu template is thinned below 50 nm, graphene can actually be synthesized directly on a dielectric without the need for the aforementioned transfer steps [54]. The production of up to 30 in  $\times$  30 in graphene films using a roll-to-roll technique has been demonstrated for the commercial production of electrical fabrics [55].

There exist a number of other techniques, of varying maturity, for producing wafer-scale graphene films that are worth mentioning. The most promising of these techniques is the production of graphene-like films on SiC – referred to as epitaxial graphene [56, 57]. Here, thermal sublimation of Si from the SiC surface results in rotationally stacked graphene layers that behave as isolated graphene sheets [58]. Epitaxial graphene has shown tremendous control over material quality, beyond CVD graphene, and potential for a number of electron devices. We have experimentally probed graphene interconnects on SiC [10], but will withhold discussion here given the hurdles it faces for insertion into CMOS. The first of these hurdles is the raw cost associated with SiC substrates, which must be lowered before epitaxial graphene becomes commercially viable. The second is that no effective techniques exist for removing the graphene from the substrate as it is chemically bound to the SiC. As such,



epitaxial graphene cannot be introduced only as a local interconnect fabric and/or in a hybrid system, but must replace FEOL and BEOL devices. Lastly, epitaxial graphene possess a strong intrinsic n-type doping due to interactions with the nucleation layer of the underlying SiC, making complimentary devices difficult to form. There also exist other techniques for synthesizing graphene and graphene films, which include the reduction of graphene oxide and diffusion through nickel [59, 60].

Aside from CMOS-compatible synthesis, the high-frequency performance of graphene is critical for its application to local interconnects. Experimental demonstrations of graphene devices operating in the 10's to 100's of GHz range have been previously shown elsewhere [27, 61-64]. The high-frequency operation of moderate quality graphene interconnects has been experimentally demonstrated in a CMOS environment [65], with further modeling efforts justifying their performance at the local level [66-69]. Graphene sheets/ribbons depart from other CNT or Cu interconnects at high-frequency due to the onset of the anomalous skin effect as the mean-free path becomes comparable to the skin depth [70]. It is important to note that when comparing graphene interconnects to Cu, the (RC) latency is a function both of the resistivity and the line-to-line capacitance ( $C_{\text{line}}$ ). While this thesis focuses on improving the resistivity of graphene, improved performance/latency to 1:1 AR Cu is also expected to stem from the reduced value of  $C_{\text{line}}$  given graphene's atomically thin geometry [71]. One metric that is particularly suited to the high-frequency operation of graphene devices is the Johnson Figure of Merit (JFoM). The JFoM is defined as the product of the cut-off frequency ( $f_T$ ) and the breakdown voltage ( $V_{\text{BD}}$ ) in the material:

$$JFoM = f_T \cdot V_{\text{BD}} \quad (2)$$

From our own work, we have shown that physical damage to the graphene interconnect (i.e., breakdown) will occur at voltages on the order of 3 V for GNRs with a sub-50 nm linewidth and 750 nm length [4]. This value has been confirmed via burnout studies on CNT as well [72, 73]. This being said, we will take  $V_{BD}$  to be  $\sim 3V$ . The intrinsic value of  $f_T$  has been expected to be as high as 323 GHz for graphene devices [62], which places the JFoM at just below  $10^4$  GHzV. However, the range for extrinsic (fabricated) transistors and interconnects is about 1.3 GHz to 100 GHz [27, 61, 63, 65], which places the JFoM in a range of 4 GHzV to 300 GHzV.

Switching focus back to electrical resistivity, in graphene interconnects with a linewidth *smaller* than 50 nm, the most significant non-ideality is the carrier scattering from LER, which is dominant over nearly all other sources of scattering. This LER scattering is a result of edge roughness along lithographically patterned or cleaved edges and aggressively reduces carrier mobility as the interconnect linewidth is scaled below 50 nm [34, 74]. Specifically, LER-limited mobility takes the form

$$\mu = A \cdot W^B \quad (3)$$

Where  $\mu$  is the mobility,  $W$  is the width,  $B$  is  $\sim 4$ , and  $A$  is a fitting parameter. As mentioned, suppressing LER scattering would require the fabrication of atomically smooth edge where the average roughness is much lower than the Fermi wavelength of carriers in the graphene channel [17]. Such “specular” edges would generally require an edge roughness below 0.5 nm. In the pursuit of such edges, there have been a handful of experimental demonstrations of quasi-smooth edges in graphene, however, none of the techniques used to produce these edges appear to be reliable for wafer-scale processing and/or compatible with CMOS infrastructure. The most promising of these techniques

involves the “unzipping” of CNT [75, 76]. Here, a defect is induced in the CNT sidewall, followed by a chemical and/or physical agitation that splits a seam in the CNT, ultimately unrolling the CNT into a graphene interconnect. A second technique cleaves graphene flakes in a solution of Nitric Acid, after which the GNR fragments are randomly poured/dispersed upon a substrate [77]. Both of these techniques face tremendous CMOS roadblocks in regards to reliable placement and orientation, repetition over an entire wafer, and cost. This being said, there is no foreseeable CMOS-compatible route for patterning smooth edges, and nanoscale graphene devices seeking high electrical conductivity must combat LER scattering through increases in the carrier density, i.e., doping.

Tuning of the carrier density in graphene is possible through both electrostatic and chemical doping techniques. A great deal of the immediate attention graphene received for electronic devices is owed to the exfoliation technique by which it was first isolated [16]. Here, graphene is exfoliated onto a  $\text{SiO}_2$  dielectric, which serves two essential functions; (1) it facilitates the optical contrast of monolayer graphene for identification [78] and (2) it functions as a back-gate to modulate the carrier density [16]. As such, modulation of the carrier density in graphene first took the form of electrostatic techniques. Since this back-gated technique, a variety of novel top-gated techniques have been developed to increase the carrier density in graphene. These include deposition of ultrathin dielectrics [79], drop casting of liquid dielectrics [80], and nano-gapped side-gates [81]. These techniques are not viable for interconnects given that they require added fabrication complexity, static power dissipation, and are limited by dielectric breakdown. However, they have been beneficial in that they have experimentally

demonstrated that the carrier density in graphene can be increased by orders of magnitude beyond its intrinsic value [80].

Where as electrostatic doping techniques can be somewhat translated over from 3D bulk semiconductors, chemical doping of graphene has remained relatively immature given its entirely unique 2D lattice. The traditional route of embedding dopant impurities within the center of the lattice has been demonstrated, however, this results in crippling reductions in mobility for graphene (four orders of magnitude reduction), washing out most of what makes graphene attractive over Cu [82, 83]. As such, to date, the majority of chemical doping techniques for graphene have focused on charge transfer due to physisorption on the basal plane. Simply put, coating the graphene surface. Such basal physisorption techniques have the advantage of being non-invasive into the lattice, preserving mobility and increasing conductivity. Specifically, this includes coatings with polymers [84], metals [85], salts [86], and physisorption of molecules [87]. Such physisorption techniques constitute the bulk of graphene chemical doping and are greatly limited in their ability to provide carrier densities beyond the range of  $10^{12} \text{ cm}^{-2}$  (making them hopeless for combating LER), as well as face challenges in regards to the high resolution complimentary doping needed to form almost all electronic devices.

## **CHAPTER 2**

### **BENCHMARKING OF INTRINSIC GNRs**

#### **2.1 Motivation for the Chapter**

Graphene, as an electronic material, has been receiving much attention as a possible replacement for Si CMOS technology. In addition to its use as a switching device, graphene can also be used as an interconnect material, and a truly monolithic system can be constructed using graphene for both transistors and interconnects [57]. Compared to Si and even III–V semiconductors, graphene has superior mobility. Ballistic transport in graphene makes it attractive not only for use as transistors but also for interconnects.

Graphene was first isolated in 2004, and since then, many properties have been confirmed experimentally, including high mobility, ballistic transport, linear E–k dispersion, and a width-dependent transport gap. Transistors fabricated from graphene nanowires have shown impressive on–off ratios [34, 88]. For interconnect applications, graphene has shown interesting properties in terms of its temperature coefficient and use as a thermal interface material [89, 90]. Theoretical projections for GNRs for use as interconnects have been made in [17], and GNRs are predicted to outperform Cu for interconnect applications. It has been theorized that single-layer GNRs can result in a lower resistance per unit length than 1:1 aspect ratio (AR) Cu, for linewidth (W) that is less than 8 nm [17]. There has been little experimental work on the electrical characterization of graphene for use as an interconnect material. While there are some experimental data for wide graphene ribbons [44], there has not been a thorough investigation of resistivity for narrow-width GNRs ( $W < 100$  nm). In this Chapter, we

will focus on characterizing graphene resistivity for narrow-width GNRs and will compare the resistivity of GNRs to that of Cu.

## 2.1 Experimental Procedure

The experimental procedure for forming graphene devices (up through the contact metallization) is described in detail here, and referenced in the subsequent Chapters. Exfoliated graphene is used as the starting material. Graphene layers are flaked from large graphite pieces (Kish graphite, Toshiba Ceramic Company) using a Scotch tape and adhered onto an oxidized Si substrate with an oxide thickness of 300 nm. The Si substrate is degenerately doped for use as a back-gate. Monolayer graphene is first identified amongst the graphitic debris field using optical contrast. An optical image of a monolayer graphene flake is shown in **Figure 5**.

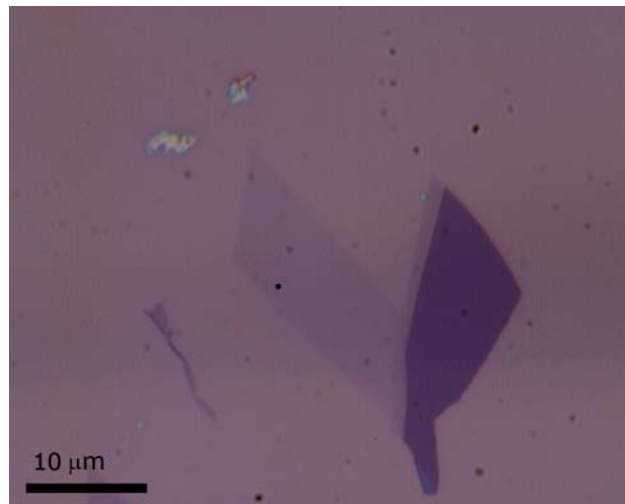


**Figure 5.** Optical image of a monolayer of exfoliated graphene amongst a graphitic debris field on 300 nm of SiO<sub>2</sub>. The lighter region indicates monolayer graphene with darker few-layer graphene to the right.

Once identified, these monolayer flakes are then verified using Raman Spectroscopy and Atomic Force Microscopy (AFM). The Raman spectrum of a monolayer graphene flake is shown in **Figure 6**.

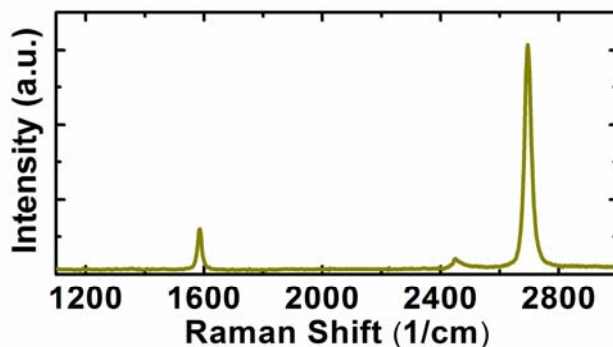


**Figure 6.** Raman spectrum of monolayer exfoliated graphene exhibiting no D-peak.

Next, a four-point contact metallization is patterned using electron beam lithography (EBL) in the positive tone resist, ZEP520A (Zeon Chemicals). The alignment of the EBL to the graphene flake occurs by documenting the position of the flake to pre-patterned alignment marks on the substrate. The four-point contact metallization pads post-develop are shown in **Figure 7**.

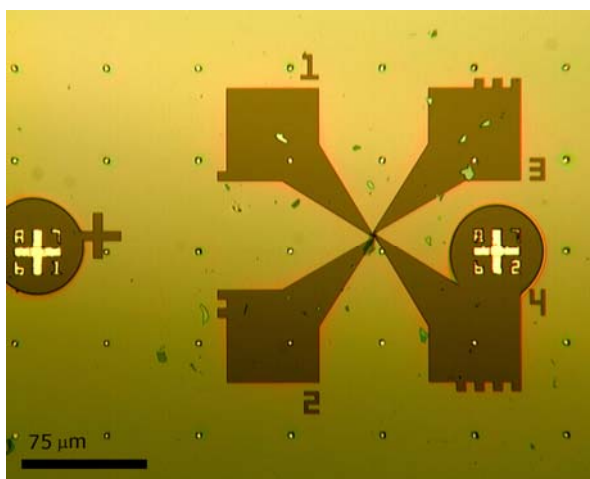


**Figure 7.** Optical image of the four-point contact metallization, post-develop, that is patterned using EBL.

Next, a Ti/Au (20 nm/80 nm) metal stack is then evaporated using an Electron Beam (E-Beam) Evaporator. The contact pads are then formed using a standard liftoff procedure in warm 1165 solvent. An SEM image of the four-point contact metallization on the graphene flake is shown in **Figure 8**.

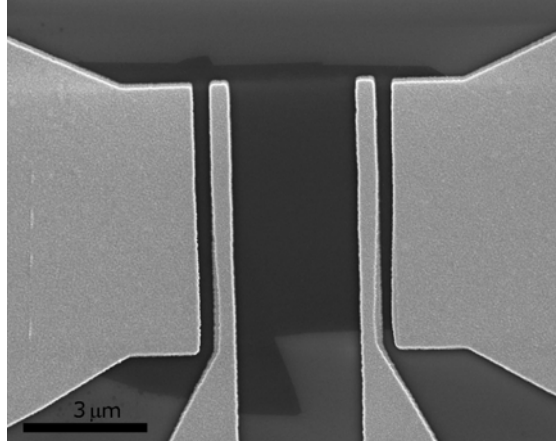


**Figure 8.** SEM image of the four-point contact metallization fingers atop a flake of exfoliated graphene.

This step is followed by characterization of the 2D graphene for contact resistance, minimum conductivity point, and the intrinsic carrier density. A second layer of EBL is used to define a set of ten GNRs in parallel with linewidth ranging from 18 nm to 52 nm, and a length ranging from 0.2 μm to 1 μm. These interconnects are patterned using the negative tone resist, HSQ. The HSQ etch mask is then transferred into the graphene using a brief exposure to an oxygen plasma. The resulting device with a set of ten GNRs is shown in **Figure 9**.

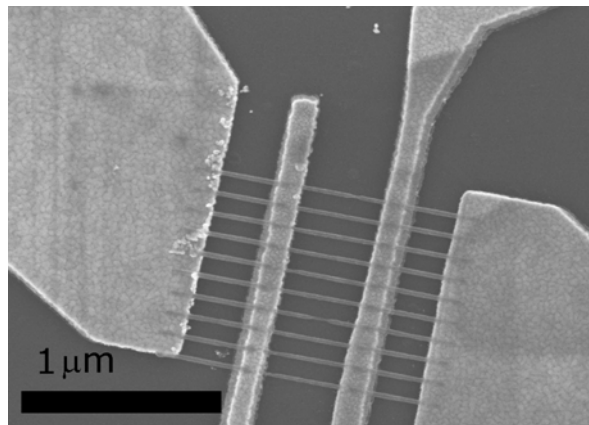


**Figure 9.** Set of ten GNRs in parallel fabricated between the four-point contact metallization. The interconnects are still coated by the HSQ etch mask.



All of the electrical measurements in this thesis are meticulously extracated using a four-point technique, hence the four-point metallization pattern in **Figure 9**. In such measurements, a standard lock-in amplifier is used to channel an excitation current (5 – 100 nA), in series with a large (10 M $\Omega$ ) resistance, through the outer fingers of the metallization. The voltage is read across the inner fingers and used to extract the resistivity/conductivity of the graphene channel. This technique is illustrated in **Figure 10** below and is essential to removing contact resistance from our measurements of the graphene. An HP 4156 semiconductor parameter analyzer was used to perform low-bias measurements along with the sweeps of the back-gate voltage. Tests for ohmic contacts were performed at voltages down to a few microvolts and there was no indication of a Schottky barrier.

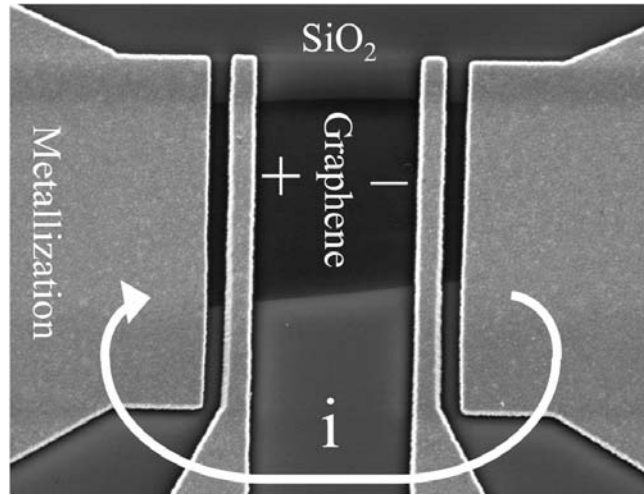


**Figure 10.** Setup for the four-point electrical testing that is performed on all graphene devices in this thesis. An excitation current (nA) is injected through the outer fingers and the voltage bias of the graphene channel is read across the inner fingers. This technique removes contact resistance from our measurements.

### 2.3 Extraction of Resistivity for GNR Sets

Contact resistance was extracted for each device at various stages of processing. The contact resistance was found to be 30  $\mu\Omega \cdot \text{cm}^2$  for most devices and did not change

after the second EBL step or after the plasma etch. Back-gated measurements of the conductance modulation reveal a small negative shift in the position of the minimum conductivity point after the HSQ spin and EBL. A large positive shift of  $V_{\min}$  is observed after the plasma etch. Unlike true metals, a semimetal such as graphene shows significant variation in conductivity with application of a back-gate bias (since this causes a shift in the Fermi level). Thus, it is important to measure resistance at the same carrier density across different GNRs to ensure a fair comparison. The carrier density is pinned by making the value of  $V_g - V_{\min}$ , where  $V_g$  is the voltage applied to the back-gate, the same across the GNR when extracting resistivity. The back-gate capacitance is  $11.5 \text{ nF/cm}^2$ , and for an electron density of  $5 \times 10^{12} \text{ cm}^{-2}$ , this translates to a  $V_g - V_{\min}$  of 70 V (for 300 nm of oxide). All resistance and resistivity measurements are thus measured at  $V_g - V_{\min} = -70 \text{ V}$  (hole carriers) so that the corresponding carrier density makes the GNR operate in the metallic regime. This translates to a Fermi energy of 63 meV for 2D graphene [91].

A total of 18 devices, each with ten parallel GNRs, were measured; these devices were selected from a larger set of samples based on their resistivity. For ease of comparison to Cu, 3D resistivity ( $\rho_{3D}$ ) is calculated for these devices; it is more common to calculate the 2D resistivity for a 2D material like graphene. **Figure 11** shows the resistivity of various devices as a function of the GNR width. Most of the data are clustered between 15 and 25  $\mu\Omega \cdot \text{cm}$ . Also shown for comparison is the Cu resistivity as projected by the International Technology Roadmap for Semiconductors (ITRS) [1]. Note that little experimental data exists for narrow Cu lines, and ITRS projections are based on extending current model parameters to narrow linewidth. Line-edge roughness

(LER) and liner scaling becomes increasingly challenging for widths below 30 nm and will lead to additional increases in effective Cu resistivity; thus, ITRS projections for Cu resistivity are optimistic but are used nonetheless since they can be thought of as the best case scenario for a Cu line. This collection of data represents, at the time, one of the largest and more promising demonstrations of GNR resistivity.

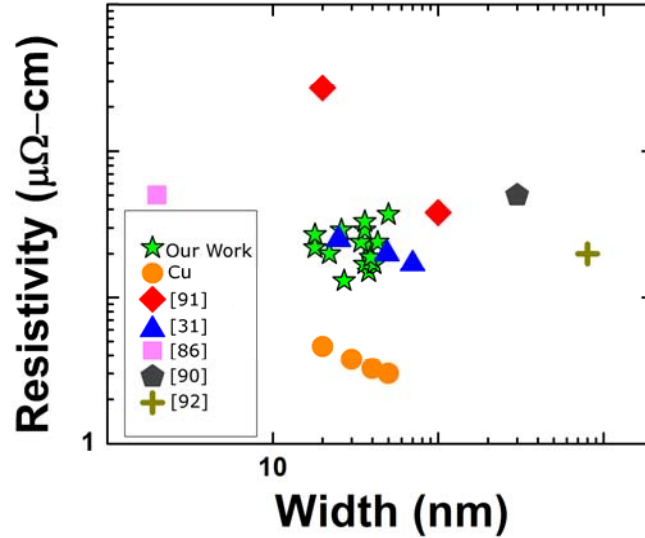


**Figure 11.** Resistivity of our GNR sets in comparison to previous works. We demonstrate one of the largest experimental collections and some of the lowest resistivities yet shown.

#### 2.4 Demonstration of Comparable Resistivity to Cu

There have been a few published results on the 2D resistivity for wide and narrow GNRs; it is informative to compare these values in **Figure 11** against other current demonstrations [34, 88, 92-94]. All measurements in this work were done at 300 K; some of the data points from previously published data were extracted from low-temperature measurements but nevertheless provide a useful comparison. The resistivity from [34] is between 16 and 30  $\mu\Omega \cdot \text{cm}$ , although the measurements were made at 200 K. For widths below 100 nm, resistivity from other previously published data is more spread out. Resistivities of GNRs from this study are some of the lowest values reported for narrow

GNRs. However, the GNRs are still two to three times less conductive than Cu wires.

The 18 devices shown in **Figure 11** have a set of ten GNRs in parallel. Critical-dimension uniformity, LER, and the starting graphene material would cause individual GNRs to have different properties compared to one another. The ribbon-to-ribbon non-uniformity is masked somewhat since ten GNRs are measured in parallel. To extract properties of single GNRs (rather than a parallel set), a large number of GNRs would have to be fabricated, to obtain a statistically significant set of resistivity data. Because of the finite size of graphene flakes (usually less than  $20\text{ }\mu\text{m}^2$ ), it is not possible to fabricate a large number of GNRs (that can be probed one at a time) on the same flake. By employing techniques applied to CNT [73], it is possible to use the device shown in **Figure 9** to extract the performance of individual GNRs.

An HP4156 semiconductor analyzer is used to apply a voltage ramp between two electrodes with ten GNRs in parallel. Due to increasing current density in the GNR, there is a voltage at which a GNR breaks down, resulting in a visible drop in current. The device testing is stopped at this point, and the voltage ramp is repeated from 0 V. Successive GNR breakdowns occur at around the same voltage as for the first breakdown event. By recording the difference in conductance between two successive breakdown events, the individual GNR conductance can be extracted. It is also found that if the voltage-ramp steps are small enough (2 mV), it is possible to avoid multiple GNR breakdowns in a single event. The contact resistance does not change after each event, and this indicates the robust nature of the contact metallization. Back-gated conductance modulation is extracted for each GNR, and the modulation does not significantly change from one GNR to another—this means that the GNRs are of similar metallicity. All

GNRs studied in this chapter showed an impressive breakdown current density of  $5\text{--}20 \times 10^8 \text{ A/cm}^2$ , which points to the superior electromigration performance of GNRs, and is published in a sister work [4]. This being said, a more detailed discussion of breakdown current density and its correlation with resistivity for various GNR dimensions will be withheld.

It is found that there is a significant difference in resistance from one GNR to another, even on the same flake. **Figure 12** shows the range of GNR resistivity extracted for four different devices, each with a different linewidth. For each width, the best, worst, and mean values of resistivity are shown. The best GNR has a resistivity that is comparable to that of Cu. For monolayer 2D graphene on  $\text{SiO}_2$ , phonon scattering limits room-temperature resistivity to about  $1.2 \mu\Omega\cdot\text{cm}$  (at  $n = 5 \times 10^{12} \text{ cm}^{-2}$ ). Thus, the best GNR is three times less conductive than this limit ( $1.2 \mu\Omega\cdot\text{cm}$ ).

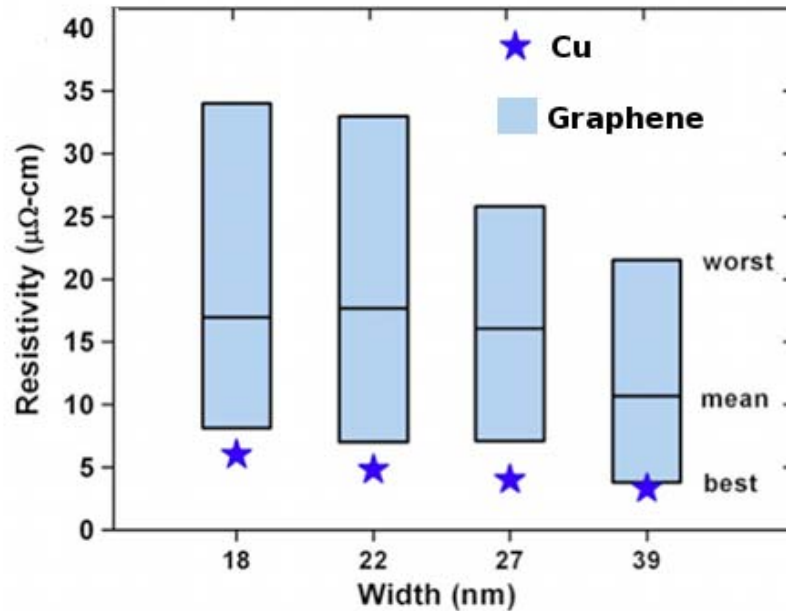


**Figure 12.** Demonstration of comparable resistivity between sub-50 nm GNRs and 1:1 aspect ratio Cu interconnects. The lowest and highest resistivity from each GNR set is extracted using a burnout technique.

Graphene on SiO<sub>2</sub> has various scattering mechanisms limiting its conductivity: (1) intrinsic scattering, which limits mobility to 200,000 cm<sup>2</sup>/Vs and is seen in suspended graphene [14]; (2) extrinsic scattering due to SiO<sub>2</sub> phonons, which imposes a carrier mobility limit of 40,000 cm<sup>2</sup>/Vs at  $n = 1 \times 10^{12} \text{ cm}^{-2}$  and  $T = 300 \text{ K}$  [19]; (3) impurity scattering; and (4) LER scattering. It is possible to estimate the contribution of impurity scattering in GNRs using the scattering theory presented in [44]. The impurity density is estimated to be  $n_i = 2\text{--}19 \times 10^{11} \text{ cm}^{-2}$  for the set of devices shown in **Figure 9**. This translates to an impurity-limited mobility of 2,500 – 19,000 cm<sup>2</sup>/Vs. It is possible to estimate the LER-limited mobility by extracting the difference in mobility before and after plasma etch (which converts 2D graphene flakes into GNRs) using Matthiessen's rule. For the 22 nm wide GNRs shown in **Figure 9**, the LER-limited mobility is in the range of 6,000–9,000 cm<sup>2</sup>/Vs, and the effective GNR mobility is in the range of 4,000–8,000 cm<sup>2</sup>/Vs; thus, GNR mobility at a 22 nm linewidth could either be limited by impurity scattering or LER scattering.

In the previous discussion of GNR resistivity, it has been implicitly assumed that multilayered graphene will be readily available to fabricate GNRs, i.e., if only single or few-layer graphene is available, then a more apt comparison parameter would be resistance per unit length. Recent experiments with graphene grown on SiC substrates have shown that truly non-interacting multilayer graphene films of tens of layers can be formed [58]—rotational stacking preserves the ballistic nature of carriers and would be valuable for interconnect applications.

In conclusion, graphene interconnects of sub-50 nm linewidth have been fabricated and compared to Cu interconnects in terms of their 3D resistivity. The average GNR

resistivity was higher than the projected Cu resistivity for linewidth ranging from 18 nm to 52 nm. Resistivities of individual GNRs have been extracted from sets of parallel GNRs, and it was found that the best GNR (for a given width) had a resistivity that was comparable to a Cu wire of the same width. An analysis of scattering mechanisms revealed that narrower GNRs were limited either by LER or impurity scattering. This Chapter gives the first experimental evidence of the potential of narrow GNRs for use as on-chip interconnects.

## CHAPTER 3

### BASAL PLANE DOPING

#### 3.1 Motivation for the Chapter

In Chapter 2 we experimentally demonstrated that intrinsic GNRs could be comparable to 1:1 AR Cu interconnects at sub-50 nm linewidth. The devices of Chapter 2 are considered intrinsic in that they exhibit moderate carrier densities in the range of  $5 \times 10^{12} \text{ cm}^{-2}$  and have not received additional processing beyond the fabrication of the interconnect. Despite being comparable to Cu, these intrinsic GNRs are far below their theoretical limit of  $\sim 1.2 \text{ } \mu\Omega\text{-cm}$  on  $\text{SiO}_2$ . The electrical resistivity ( $\rho$ ) of interconnects takes the form of any traditional conductor,

$$\rho = \frac{1}{q\mu n} \quad (4)$$

where  $q$  is the charge of an electron ( $1.602 \times 10^{-19}$ ),  $n$  is the carrier density, and  $\mu$  is the carrier mobility in the interconnect. Thus, two routes exist for pushing the resistivity down towards its theoretical limit, improve  $n$  or improve  $\mu$ . As mentioned in Chapter 1, the mobility of sub-50 nm GNRs is dominated by LER scattering, which results in increasingly aggressive reductions in  $\mu$  as the linewidth is scaled. This can theoretically be overcome via the fabrication of devices with atomically smooth edges. However, no techniques currently exist, or are foreseeable in the near future, for fabricating smooth edges in a reliable, cost effective, and CMOS-compatible manner.

As such, improving the electrical conductivity ( $\sigma$ ) of sub-50 nm GNRs is most viable through increases in the carrier density. Regarding doping of interconnects; chemical techniques are attractive over electrostatic techniques, as they do not require a



voltage bias or additional processing to form the gate. As increased conductivity for local interconnects is the focus of this thesis, we begin our approach to chemical doping with a non-invasive basal plane (i.e., physisorption) technique in hopes of preserving the crystallinity of the graphene sheet. Given the atomically thin nature of the graphene lattice, it is susceptible to changes in  $n$  through physisorption interactions with the basal plane and does not necessarily require the embedding of defects as with traditional bulk semiconductors. As such, we can potentially tune the value of  $n$  via the basal plane while maintaining high values of  $\mu$ , resulting in increased conductivity.

A variety of techniques have been previously employed to provide both p-type and n-type chemical doping to the basal plane of graphene. These include coating graphene with polymers [84], diazonium salts [86], metals [85], and physisorption of molecules [87]. However, these techniques are considered far too immature for CMOS given that (1) these techniques can only apply one type of doping (p-type or n-type) and are not complimentary, (2) these techniques are not tunable and can only induce a single specific carrier density, and (3) these techniques can only apply a blanket doping and require masking and added process steps to pattern doped regions. In this Chapter, we present a basal plane technique that is capable of tunable complimentary (p-type or not n-type) doping, is capable of ultrahigh resolution in a single process step, and can preserve  $\mu$  for pure conductance increases. This technique is used to demonstrate the first chemically doped p-n junction in graphene.

### **3.2 Experimental Procedure**

Graphene devices with four-point contact metallization were fabricated using exfoliated flakes via the process discussed in Chapter 2. Few (1-3) layer graphene was

used to demonstrate the robustness of the chemical doping technique. The technique presented here involves the spin-on glass, HSQ, and is referred to hereon as the “HSQ doping technique.” HSQ was previously referenced in Chapter 2 as the ultrahigh resolution e-beam resist used to pattern our GNRs. All electrical testing was performed using the four-point technique, to remove contact resistance, using a lock-in amplifier.

### 3.3 Demonstration of Tunable/Complimentary Basal Doping via E-Beam

Here, we demonstrate tunable p-type and n-type chemical doping in graphene through interactions of HSQ with the basal plane. Initially, the effect of e-beam-induced cross-linking in HSQ on carrier transport in few layer graphene was studied. Two samples were fabricated, each containing multiple devices. The devices were tested for their carrier density with a back-gate (through the position of  $V_{min}$ ) and were found to have little initial doping with respect to the HSQ induced shift, **Figure 13a**. After thorough sample cleaning, it was confirmed that the initial doping present in these devices is a result of exposure to the ambient environment and not of residual resist. The samples were then coated with a 30 nm thick film of HSQ and baked for 3 min. at 180 °C. One sample was developed in tetramethylammonium hydroxide (TMAH), washing away the HSQ. Gated electrical testing post-development of this sample revealed a strong n-type doping as indicated by the shift of  $V_{min}$  to a larger negative gate voltage, **Figure 13b**. The second sample was patterned with EBL—the pattern consisted of large regions (20  $\mu\text{m}$  diameter) covering each flake with a dose of 3200  $\mu\text{C}/\text{cm}^2$ , **Figure 14**. Gated electrical testing of these devices revealed a large positive shift of the  $V_{min}$ , thus indicating a strong p-type doping—**Figure 13c**. For p-type HSQ doping, electron-hole symmetry is observed near the minimum conductivity point.

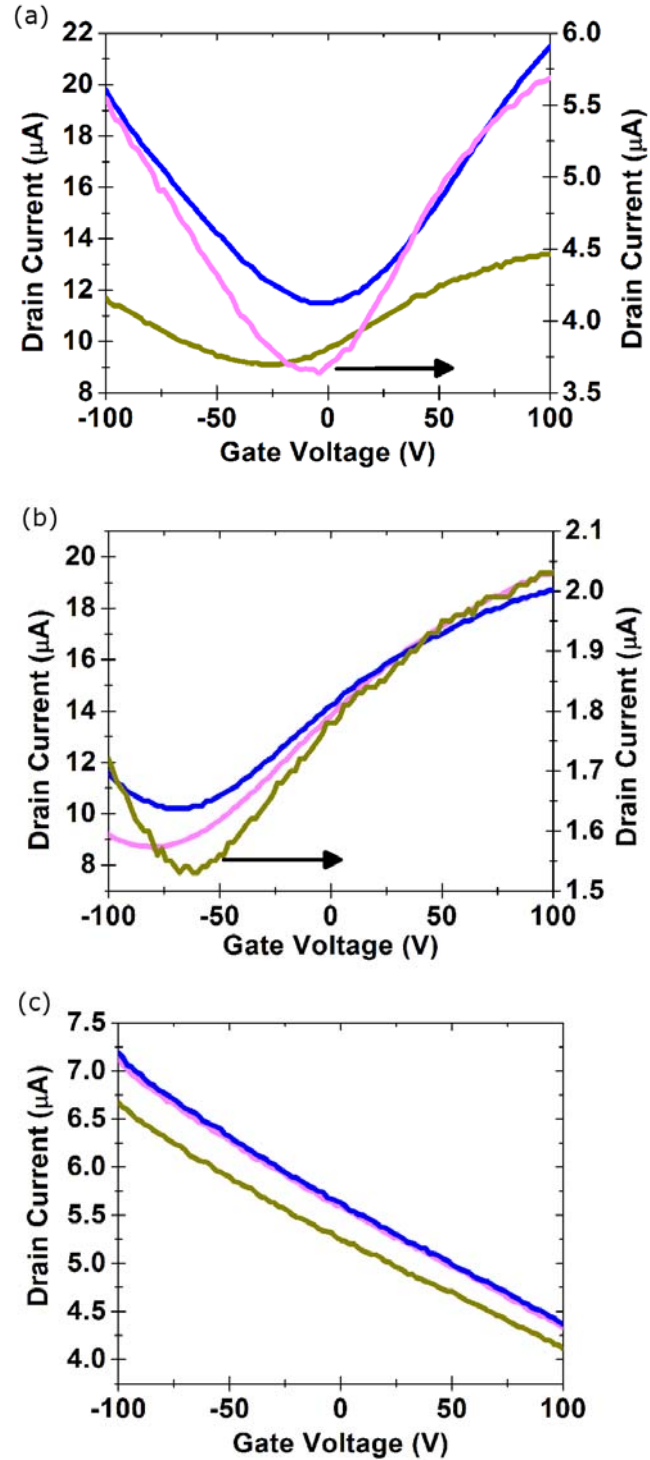


**Figure 13.** Demonstration of p-type and n-type doping via coating the graphene basal plane with a film of HSQ. (a) Three pristine devices show low intrinsic doping prior to coating. (b) Devices are coated with HSQ, baked, and developed. A strong n-type doping is observed. (c) Devices are coated with HSQ that is heavily cross-linked via e-beam irradiation. A strong p-type doping is observed.

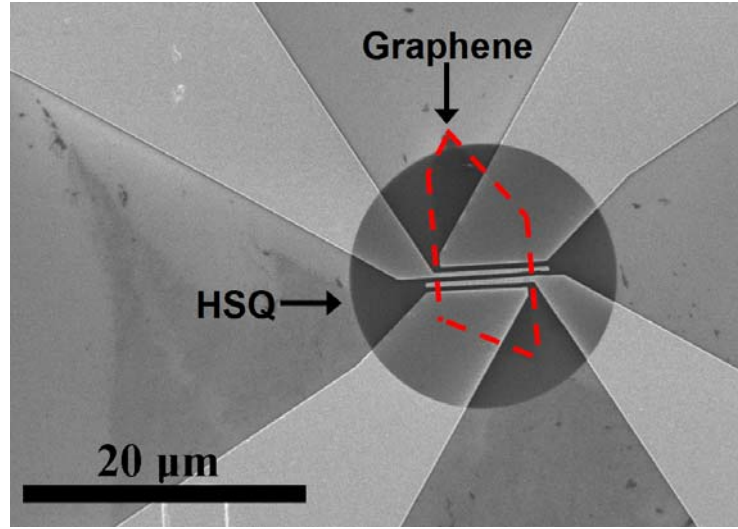


**Figure 14.** SEM image showing a graphene device coated with a 20  $\mu\text{m}$  diameter film of HSQ. The film is patterned using EBL.

A number of devices of the form of **Figure 14** were fabricated, each with a different dose for the HSQ. The incident dose ranged from 250 - 5,000  $\mu\text{C}/\text{cm}^2$ . A plot of the shifts of  $V_{\text{min}}$  (i.e., the difference in  $V_{\text{min}}$  between the metallization and HSQ patterning steps) for varying doses is shown in **Figure 15**. Since HSQ-induced doping can be quantified by the resulting shift in  $V_{\text{min}}$ , the induced doping can be effectively measured regardless of the initial doping levels present in the devices. Error bars indicate shifts of  $V_{\text{min}}$  outside of the measurable range ( $\pm 100$  V). For zero dose (i.e., HSQ is spun-on and developed without any e-beam irradiation), a large negative shift in  $V_{\text{min}}$  is seen and is consistent with results discussed previously. For a dose between 250 – 1,000  $\mu\text{C}/\text{cm}^2$ , the  $V_{\text{min}}$  shift ( $\Delta V_{\text{min}}$ ) increases from more than  $\pm 100$  to 0 V. For doses between 1,000 – 5,000  $\mu\text{C}/\text{cm}^2$ ,  $\Delta V_{\text{min}}$  increases from 0 V to more than 100 V and a saturation is seen in the amount of shift induced. This saturation is likely due to saturation of cross-linking for doses higher than 2,000  $\mu\text{C} / \text{cm}^2$ .

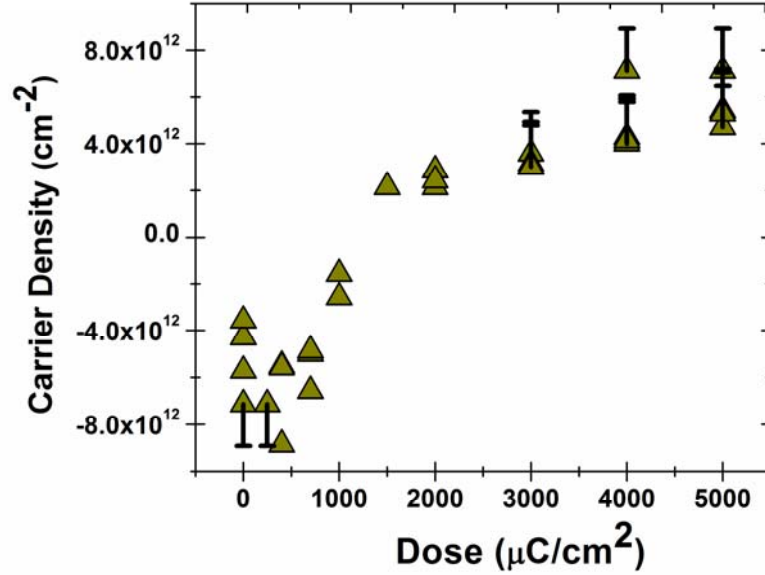


**Figure 15.** Demonstration of tunable complimentary doping of graphene via HSQ films on the basal plane. The cross-linking in the HSQ is controlled through the incident irradiation delivered by the EBL. At low cross-linking (low dose), a strong n-type doping is observed. As the cross-linking is increased (higher dose) a smooth transition to strong p-type doping is observed. Error bars indicate doping levels beyond the gate bias of  $\pm 100$  V.

### 3.3 Demonstration of Tunable/Complimentary Basal Doping via Plasma

The application of HSQ for chemical doping provides novel avenues for tuning the carrier density in graphene. That is, there exist other techniques for providing energy to cross-link the HSQ film. These include thermal annealing at temperatures of around 500 °C, which is known to induce a structural change [95], and exposure to a plasma of energetic ions can also be used with the benefit of a lower temperature for processes with a tight thermal budget. To investigate plasma-induced cross-linking, three graphene devices with metal contacts were fabricated and coated with 30 nm of HSQ. The devices were exposed with a low dose of 600  $\mu\text{C}/\text{cm}^2$ , with the same pattern as in **Figure 14**, to get a layer of HSQ patterned on the device while inducing little shift in the minimum conductivity point. This was followed by a timed exposure to a low-power Argon plasma

with an Argon flow rate of 25 SCCM (SCCM denotes cubic centimeter per minute at standard temperature and pressure). Short, one second, flash exposures to the plasma were used followed by electrical testing in between each step. The relation between exposure time to the plasma and the position of  $V_{min}$  demonstrates tunable complimentary conductance improvements for both p-type and n-type carriers in graphene. The carrier mobility was monitored (through the slope of the I-V relation) and was found to remain constant regardless of plasma exposure time. These conductance improvements are shown in **Figure 16**.

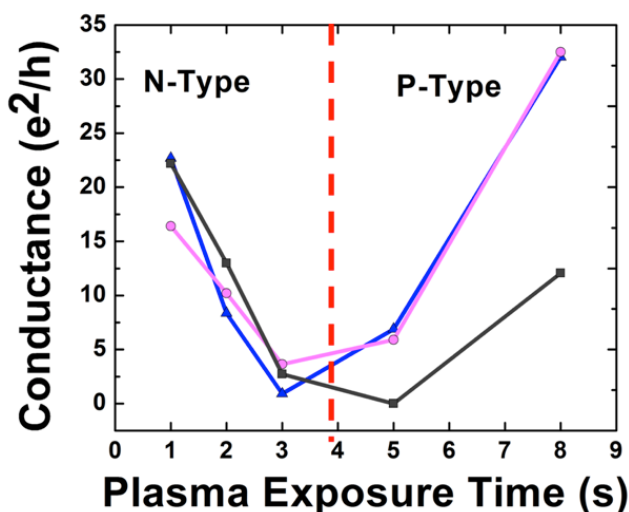


**Figure 16.** Demonstration of tunable complimentary improvements in conductance via plasma-induced cross-linking of HSQ films on graphene. Controlling the exposure time to the plasma, the carrier density is tuned from strong n-type to strong p-type, while preserving the mobility in the graphene.

### 3.4 Demonstration of the First Chemically Doped P-N Junction

The dual nature of HSQ – resulting in both n-type and p-type doping of graphene – is attributed to the mismatch of bond strengths between Si–H and Si–O bonds in the HSQ film, as well as the out-gassing of hydrogen at higher degrees of cross-linking. It has been predicted that basal-plane physisorption of hydrogen leads to n-type doping of graphene [95, 96]. It is also well documented that physisorption of species from the ambient

environment, specifically water vapor and oxygen, lead to p-type doping [16, 97, 98]. In HSQ, Si–H bonds are more easily broken than Si–O bonds; Si–H bonds have a bond strength of 4.08 eV while Si–O bonds have a bond strength of 8.95 eV [95]. At low degrees of cross-linking, Si–H bonds are readily broken providing hydrogen to bond with the graphene basal-plane. Due to the offset in electronegativity, hydrogen acts as an n-type dopant for graphene. Higher degrees of cross-linking in the HSQ film lead to p-type doping. There are two primary mechanisms that facilitate the switch from electron to hole carriers in the material. The first is that Si–O bonds begin to break at more mature stages of cross-linking due to their larger bond strength. The breaking of Si–O bonds provides oxygen for physisorption at the graphene surface. The second contributor to the observed p-type doping is the removal of hydrogen from the HSQ film. Advanced stages of cross-linking lead to HSQ decomposing into  $\text{SiH}_4$  and  $\text{H}_2$  components [95]. These components escape from the HSQ film, as evident through decreased Si–H:Si–O bond ratios as well as the porous nature of the film. The structural changes of cross-linked HSQ are illustrated in **Figure 17**.

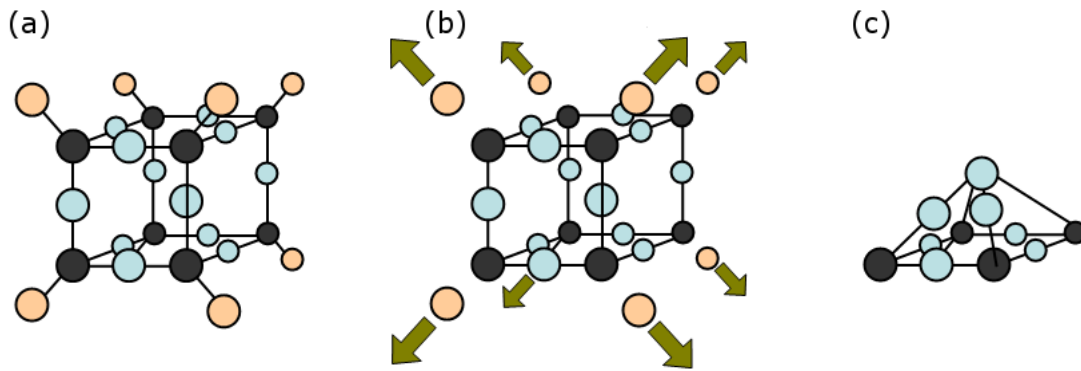


**Figure 17.** Structural and chemical changes to the HSQ film during cross-linking. (a) The cage-like network of HSQ with H (tan), O (blue), and Si (black) atoms. (b) Outgassing of the H with moderate cross-linking. (c) Complete removal of H and collapsing to a dense network-like structure after advanced cross-linking.

Doping through plasma exposure can be used to provide rapid doping over the surface of large area graphene with minimal reduction in mobility. This would be beneficial to applications that need conductivity higher than that offered by intrinsic graphene – for example, on-chip interconnects. Spin-coating graphene ribbons with a layer of HSQ and subjecting them to plasma exposure would result in high-conductivity graphene ribbons as well as a low-k coating that is required as an interlayer dielectric. In addition, the dual nature of HSQ doping can be used to create p-n junctions in a single process step. Fabrication of the first chemically doped p-n junction in graphene is demonstrated using the HSQ doping technique – **Figure 18**.

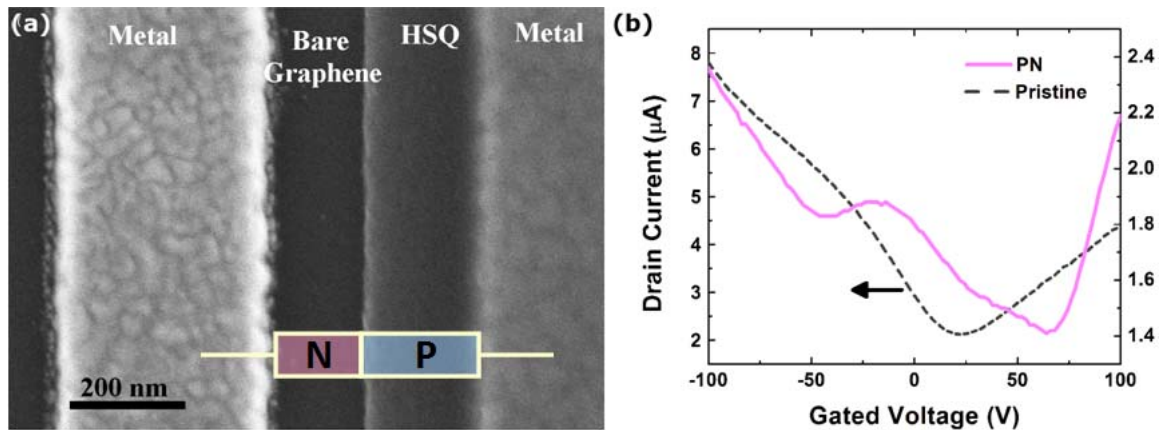


**Figure 18.** Demonstration of the first chemically doped p-n junction in graphene. (a) An SEM of the p-n junction. Two metallization fingers span a region of bare (p-type) graphene and HSQ-coated (n-type) graphene. (c) Gated electrical testing of the device reveals two distinct minimum conductivity points to the left and right of zero gate bias, confirming the formation of a true p-n junction.

An HSQ stripe was exposed over half of a graphene channel while leaving the other half unexposed, defining the p-region and n-region, respectively. Gated electrical testing reveals two distinct minimum conductivity points, indicating complementary regions of doping. It has been shown that local minimums in gated-current testing are indicative of p-n junction formation in graphene devices. Presented here is the first evidence of a



chemically doped graphene p-n junction with Dirac points clearly indicating the superposition of p and n regions and with separations in excess of 100 V. Using the relation between Fermi level and carrier density, the p-n junction demonstrated in this work is expected to exhibit an energy separation between the two neutrality points in excess of 340 meV, the highest yet reported for a chemically doped junction. Deviations from the expected location of the minimum conductivity points have been previously observed and are attributed to induced states that allow carrier penetration into the adjacent region [86]. Extension of locally doped carriers into the adjacent complementary regions by up to 450 nm have been observed [99]. The levels of doping presented in this work are shown to be significantly high enough to maintain locally defined p-type and n-type regions, despite slight degradation due to carrier mixing between the two complementary doped regions. As with any graphene device, prolonged exposure to the ambient environment induced a background p-type doping to the fabricated p-n junction [16]. Passivation is required to pin the energy levels in both the p- and n- regions.

### **3.4 Investigation of P-N Junction Interconnect Waveguides**

In addition to the fundamental significance of complimentary doping for graphene devices, in general, the demonstration of a p-n junction has direct application for novel interconnect architectures. Mainly, these come in the form of electron waveguides. Such waveguided interconnects can be applied as supercollimation in a series of p-n junctions [33], electron optical fibers [100], and electron lenses that can focus the flow of charge [31]. These architectures are based on the ability to deflect and channel carriers in graphene at the interfaces of p-n junctions, without a loss in momentum; i.e., ballistic

interconnects [101]. The main advantage that can come from a waveguided interconnect is the removal of LER scattering. Such electron waveguides do not require physical etching of the edges, and as such, can maintain ultrahigh mobility and/or ballistic transport in the graphene. In addition to this, electron waveguides can provide benefits to the thermal management of ICs. Graphene sheets exhibit the largest in-plane thermal conductivity of any known material [25]. By maintaining a continuous lattice (where interconnect paths are patterned via doping and not etching), the graphene sheet can serve as a heat spreader, minimizing local hot spots and providing a means of pulling heat from the chip. This being said, an experimental investigation of such waveguided interconnects warranted investigation.

To experimentally investigate p-n junction interconnects waveguides, we employed the HSQ doping technique to fabricate electrically decoupled interconnect paths in graphene sheets. Mainly, this took the form of two interconnect paths in parallel, separated by a variety of p-n junctions – **Figure 19**. The p-n junctions can be seen by the HSQ stripes that decouple the interconnect paths between the sets of contacts. This decoupling is thought to stem from the scattering and reflection of carriers at the p-n interface [30].

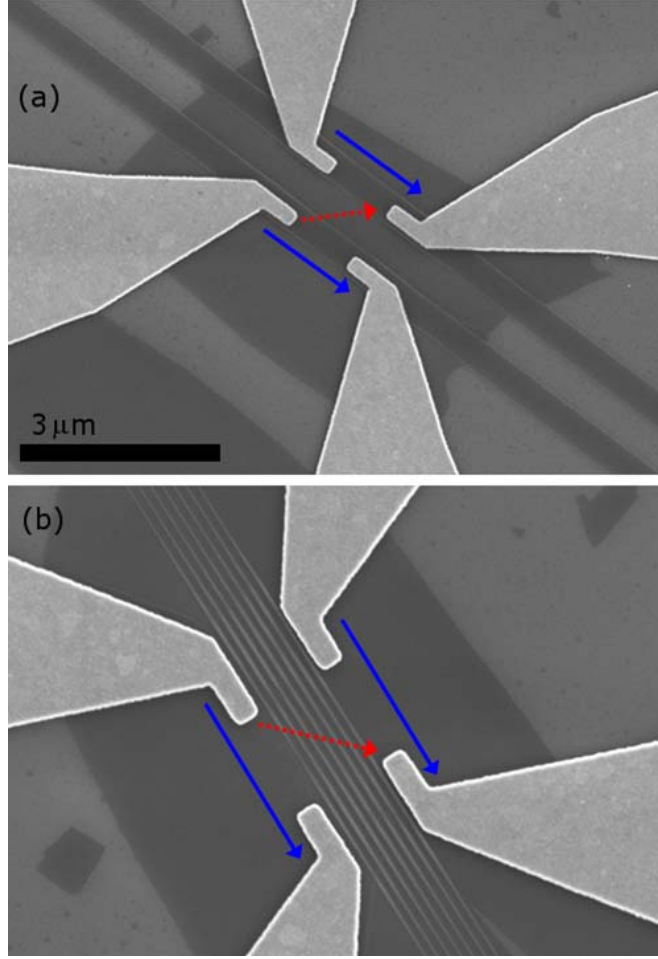


**Figure 19.** Experimental investigation of waveguided interconnects based on p-n junctions in graphene. The interconnect paths (blue arrow) are electrically decoupled (red arrow) through the formation of p-n junctions. The p-n junctions are indicated by the lighter stripes of HSQ. Two architectures are presented with a (a) A single p-n junction and (b) with multiple p-n junctions.

The electrical conductivity through the interconnects (blue arrow) and through the decoupled path (red arrow) was extracted. **Figure 20** shows the corresponding gated electrical testing for the two paths. It can be seen that the electron mobility is maintained within the interconnect and degraded through the decoupled path. The decoupled path also exhibits signs of p-n junction formation via the emergence of local minimum conductivity points. Despite promising results, this architecture requires significant

maturing of the processing technology – improved material quality and sharper p-n junctions – before it can be considered a viable technique for CMOS processing.

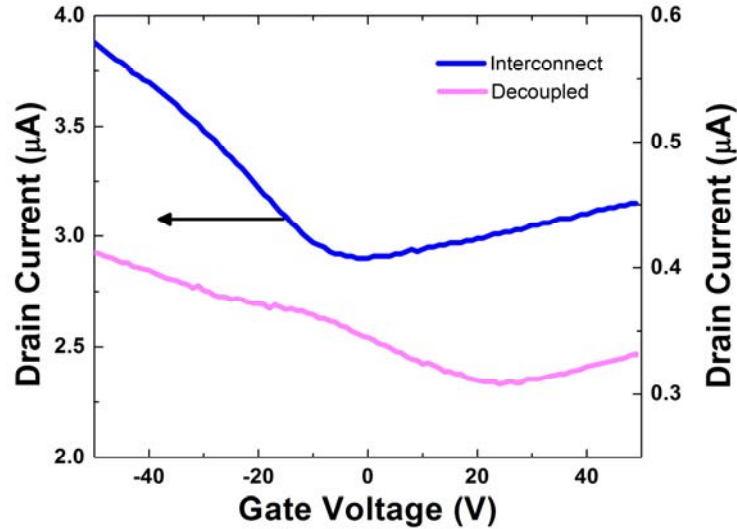


**Figure 20.** Gated electrical testing of the preliminary waveguided interconnects based on p-n junctions. The interconnect path (blue curve) shows a higher drain current with a single minimum conductivity point. The decoupled path (red curve) shows an order of magnitude reduction in the drain current, and signs of p-n junction formation via the two local minimum conductivity points.

In conclusion, it has been shown that HSQ films on graphene are capable of complementary doping. Since HSQ can be patterned with high resolution, the technique proposed here offers high-resolution fabrication of n-doped and p-doped regions. The n-type and p-type doping mechanism of HSQ is attributed to basal plane bonding of hydrogen and oxygen, respectively. The duality of this process results from the mismatch in bond strengths between Si–H and Si–O bonds in the material as well as the out-gassing of hydrogen from the film at higher levels of cross-linking. It has been shown that cross-linking of the HSQ film can be induced either by e-beam irradiation or low-power plasma exposure, allowing for complementary doping in a single processing step. The first graphene p-n junction was fabricated using HSQ doping and was found to have large energy level separations, indicating strong p- and n-type doping. This Chapter provides

evidence for a technique that is capable of single-step, high resolution, complementary doping of graphene.

## **CHAPTER 4**

### **COMPARISON OF BASAL AND DEFECT DOPING**

#### **4.1 Motivation for the Chapter**

Despite the conductance improvements demonstrated in Chapter 3, a fundamental investigation of the most efficient means of doping graphene into high conductance nanoscale devices (interconnects) is absent. Moreover, it appears in Chapter 3, as well as other works [96], that chemical doping via the basal plane is limited to carrier densities on the order of  $5 \times 10^{12} \text{ cm}^{-2}$ . This being said, we employ the HSQ doping technique of Chapter 3 to provide a direct comparison between two fundamental chemical doping techniques: (1) basal plane physisorption and (2) vacancy defect passivation. In conducting this comparison, we extract the chemical doping efficiencies for both techniques in a metric of carriers donated per available C-atom in the graphene lattice. Ultimately, these observations lead to the identification of edge-defect passivation as an efficient and scalable means of chemically doping nanoscale graphene devices.

Graphene sheets, a 2D allotrope of carbon, have recently drawn enormous attention as a potential candidate for nanoscale electrical conduction applications. High intrinsic mobility [42, 102, 103], combined with the ability to modulate the Fermi level [16], allows the conductivity of graphene to be tuned by orders of magnitude. Chemical routes toward doping graphene are highly attractive over electrostatic techniques, which require static power dissipation and are limited by dielectric breakdown and stability issues [104, 105]. Being a 2D system, graphene requires a departure from 3D bulk semiconductor doping techniques and a rethinking of the most efficient and practical route toward doping the material at nanoscale dimensions. Owing to the graphene sheet being

atomically thin, doping techniques that are less intrusive and preserve a pristine lattice are desirable over the direct incorporation of dopant species into the basal plane, which can severely limit mobility [83]. In this Chapter, we show that the passivation of C-atoms residing adjacent to vacancy defects is over three orders of magnitude more efficient a doping mechanism than physisorption on basal plane C-atoms, the metric for comparison being conducting carriers donated per available C-atom in the graphene lattice. When leveraging naturally occurring edge defects as dopant sites, i.e. broken  $\sigma$ -bonds along edge C-atoms, a scaling trend of increased doping with reduced dimensions is observed and will exhibit pronounced control over the carrier density as large-area graphene sheets are scaled into nanometer features.

Most of the doping techniques shown to date on graphene operate on the mechanism of surface charge transfer; physisorption or intimate contact on a continuous and nearly vacancy-free basal plane. It has been shown that graphene doping can be induced by interactions with a number of materials such as physisorption of gasses [28], liquids [106], polymers [84], metals [85], and organic molecules [87]. Also, we have demonstrated in Chapter 3 that thin films of HSQ can be used to either n- or p-dope graphene by controlling the amount of incident energy [5]; the film undergoes a transition from H- rich to O-rich as it cross-links, corresponding to n- and p-doping, respectively.

Intrinsic graphene is thought to have a carrier density of  $10^{11} \text{ cm}^{-2}$  [16, 107]; comparing this to the atomic density of monolayer graphene ( $4 \times 10^{15} \text{ cm}^{-2}$ ), only 1 in 40,000 atoms contributes to conduction at room temperature. However, carrier densities on the order of  $10^{14} \text{ cm}^{-2}$  can be induced by electrostatic doping [80]. Though doping by electrostatic gating is impractical for most applications, it provides evidence that the

carrier density in graphene sheets can be increased to more than 1,000 times the intrinsic density. Surface charge transfer induces only a weak carrier density in graphene, on the order of  $10^{12} \text{ cm}^{-2}$ , and is predicted to exhibit an effective charge donated per C-atom on the order of  $1 \times 10^{-3} - 1 \times 10^{-2}$  carriers [85, 96, 108]. Techniques of inducing ultrahigh carrier densities in nanoscale graphene sheets, without significant reductions in mobility or requiring static power dissipation are highly sought. The passivation of naturally occurring defects along the edge of cleaved graphene sheets can provide an efficient and potentially effortless chemical doping route for widely tuning the conductance of nanoscale graphene devices. Many predictions have been made on the doping possibilities by graphene edge decoration with various species [109-112]. In addition, the elevated reactivity of the edge has also been studied in relation to the basal plane [113, 114], making edge defects a natural candidate for passivation. Along these lines, ammonia doping of fabricated graphene nanoribbons was thought to have a strong edge doping component [115]. Raman studies of diazonium salt functionalization of edges reveal that a defect-related peak (D-peak) at  $1,350 \text{ cm}^{-1}$  is visible at the edges [116], and is attributed to covalent bonding of edge atoms with the doping species. In this work, we provide a direct comparison of the doping efficiency of edge defect sites versus physisorption on basal plane C-atoms on graphene sheets, highlighting intrinsic scaling laws unique to edge defect doping that are predicted to dominate in the nanoscale regime.

## 4.2 Experimental Procedure

The mechanical exfoliation of the graphene sheets used in this work is carried out under ambient atmospheric conditions, on thermally grown  $\text{SiO}_2$  (300 nm) atop a heavily doped Si substrate, similar to Chapters 2 and 3. Monolayer graphene sheets are again first



identified by optical contrast then verified using Raman and AFM. A four-point contact metallization pattern is defined using EBL, followed by an e-beam evaporation of a Ti/Au metal stack (20 nm/80 nm) and a standard metal liftoff procedure. A short, controlled exposure to a 5 keV e-beam occurs for all graphene sheets during quick SEM imaging to obtain accurate geometries for subsequent edge patterning. Graphene devices are then pumped for 24 h at a vacuum of  $1.5 \times 10^{-6}$  Torr before four-point electrical testing is performed under vacuum at room temperature to extract the intrinsic material properties. A pulsed-gate bias technique is used to minimize oxide and impurity hysteresis [117], which is verified by performing double sweeps of the gate bias.

A thin film of HSQ atop the graphene sheet is employed to provide both n-doping and p-doping to either the edge or basal plane [5]. By controlling the degree of cross-linking in the HSQ, n-doped and p-doped regions can be selectively patterned [95, 118, 119]. All graphene sheets go through a spin-on application of HSQ (30 nm), a bake (180 °C) and an application of appropriate dose to the edge and basal plane. The EBL dose is delivered using a JEOL JBX-9300FS 100 keV e-beam operating at a 2 nA beam current with a 4 nm spot diameter;  $1.5 \times 10^4$  A/cm<sup>2</sup> current density. Lastly, the graphene sheets go through a develop in TMAH to remove uncross-linked HSQ. To define an n-doped basal region, a low dose of 200  $\mu\text{C}/\text{cm}^2$  is delivered to the film/graphene stack to avoid e-beam induced damage of graphene while at the same time providing a shift of the Fermi level ( $\sim 200$  meV) into the conduction band. To define a p-doped region, a dose of 2000  $\mu\text{C}/\text{cm}^2$  is used since it sufficiently outgases H from the film, making it O-rich.

All graphene sheets that are compared in this work are subject to identical process conditions to reduce process-induced variability between samples, and have nearly

identical widths. After the sheets are tested for their initial (pristine) response and spin-coated with the HSQ thin film, they are processed into two distinct devices: (1) n-doped edge and n-doped basal plane and (2) p-doped edge and n-doped basal plane. These are labeled as NNG and PNG sheets, respectively. For NNG sheets, n-doping is applied to the edge and basal plane by exposing the entire sheet to the uniform low e-beam dose. For PNG, p-doping is selectively applied to the graphene edge by exposing a narrow O-rich HSQ layer along the edge of the sheet to the high e-beam dose while the low dose is still given to the basal plane to induce similar n-doping. A minimal ( $\sim 200$  nm) high dose HSQ overlap onto the basal plane of the PNG sheet is achieved, thereby allowing for an independent study of the edge doping and basal plane doping components. An illustration of an NNG and PNG sheet is shown in **Figure 21**.

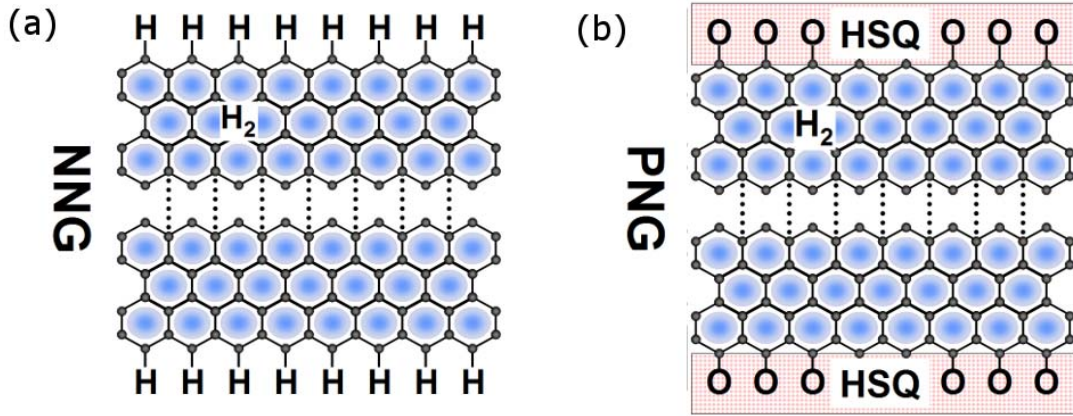


**Figure 21.** Illustration of NNG and PNG sheets. (a) An NNG sheet has an n-type basal plane from physisorption of molecular hydrogen ( $H_2$ ) and an n-type edge from  $sp^2$  passivation with H. (b) A PNG sheet has an n-type basal plane from physisorption of  $H_2$  and a p-type edge from passivation with O. The O along the edge is provided by a cross-linked film of HSQ along the edge region.

Low-power Raman spectroscopy is performed on both the basal plane and edge of the graphene, **Figure 22**. A D-peak in the Raman spectrum is observed exclusively along the edge of the sheet, verifying a finite passivated edge defect population as well as the pristine quality of the basal plane.

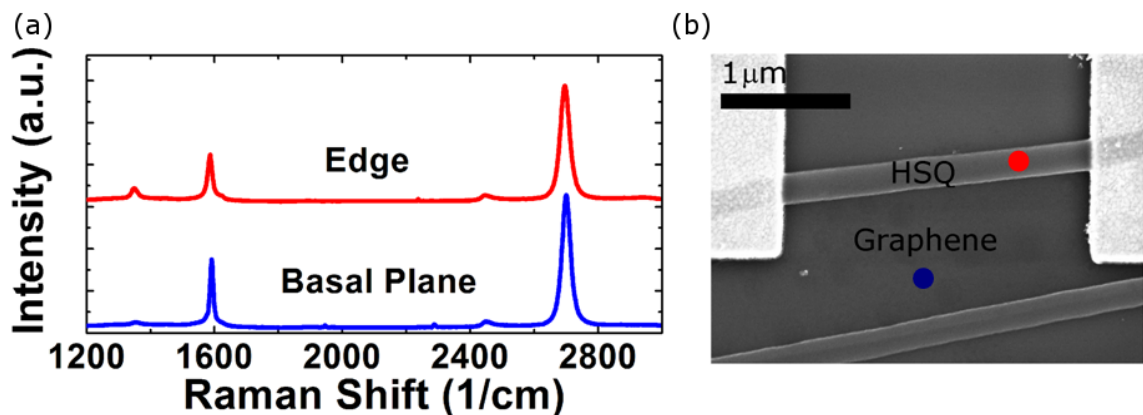


**Figure 22.** Raman spectrum on the basal plane and edge of graphene sheets. (a) The Raman spectrum verifies monolayer graphene with a defect free basal plane. The edge region displays a D-peak at  $1,350\text{ cm}^{-1}$  indicating defect passivation. (b) Mapping of the positions where the Raman spectrum are taken. A thin film of HSQ is seen along the edge of the PNG sheet.

### 4.3 Basal and Defect Doping Techniques

Electrical testing on an NNG sheet reveals a significant negative shift in the minimum conductivity point compared to the pristine response, **Figure 23a**. This is caused by the charge-transfer from H to the graphene and is consistent with the n-doping previously reported [5, 96]. The novelty of this work lies in understanding the behavior of PNG sheets, where the competition between p-doped edges and an n-doped basal plane allows for a direct observation of the role of the edge doping component, **Figure 23b**. It can be seen that the PNG sheet displays a reduced shift of  $V_{\min}$  of 8 V. An NNG sheet has an n-doped edge resulting from  $\text{sp}^2$  H-passivation of dangling bonds on edge defects, as well as an n-doped basal plane due to physisorption of molecular  $\text{H}_2$ , **Figure 21a**. A PNG sheet has a p-doped edge resulting from O-passivation, and a similar n-doped basal plane resulting from  $\text{H}_2$  physisorption, **Figure 21b**.

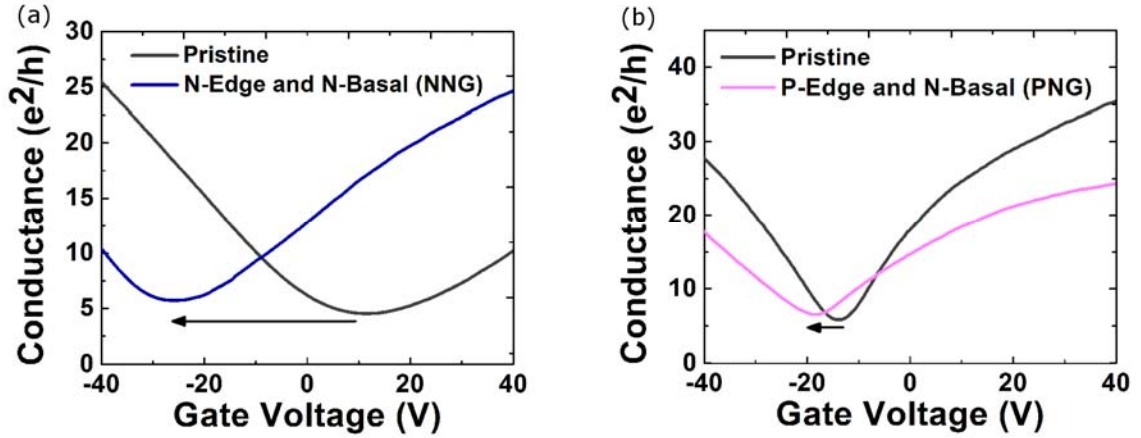


**Figure 23.** Gated electrical testing of an NNG and PNG sheet. (a) The NNG sheet exhibits a strong n-type doping resulting in a shift of  $V_{min}$  by -35V from its pristine value. (b) The PNG sheet exhibits a suppressed n-type doping resulting in a shift of  $V_{min}$  by only -8V from its pristine value. The suppressed doping for the PNG sheet is attributed to the p-type doping from the edge.

An SEM image of a PNG sheet with contact metallization is shown in **Figure 24**. A narrow O-rich region of heavily cross-linked HSQ is visible along the sheet edge, inducing O-passivated edge defects. NNG sheets are found to exhibit shifts of  $V_{min}$  ranging from -40 to -28 V and PNG sheets exhibit shifts from -15 to -3 V. The variation in the pristine doping level of the NNG and PNG sheet is attributed to dopants trapped between the graphene and substrate. Despite thorough cleaning and sufficient dwell time under high vacuum, these doping levels will vary slightly between substrates; yet remain constant throughout processing.

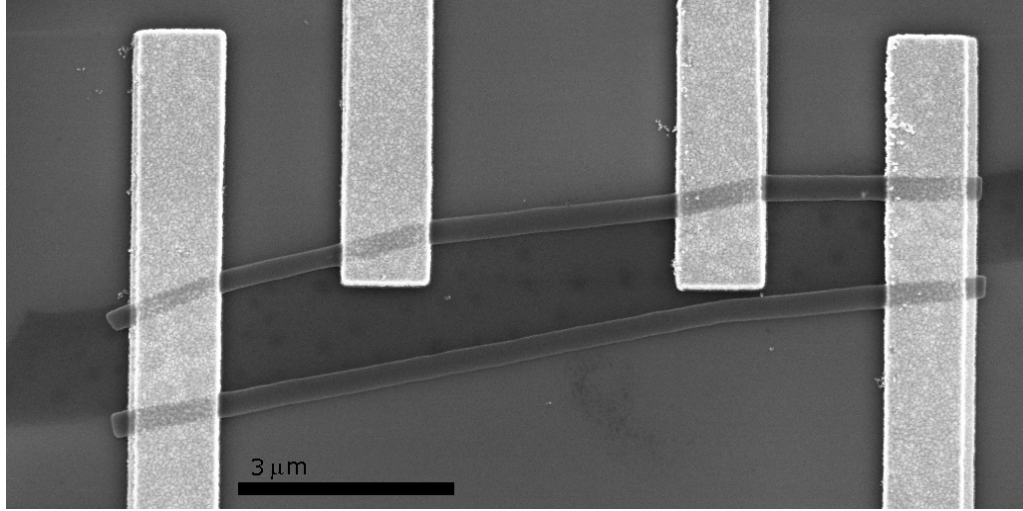


**Figure 24.** SEM image of a PNG sheet. An HSQ strip with 200 nm overlap is clearly visible along the sheet edge. The HSQ is used to transition the edge doping to p-type doping.

A direct observation of edge doping is obtained by demonstrating NNG and PNG behavior on the same graphene sheet, **Figure 25**. An NNG sheet is compared to its pristine response and found to exhibit a -25 V shift of  $V_{min}$ . The edge is then transitioned from n-doping to p-doping via an EBL exposure; similar to all PNG sheets. It is found that by changing the polarity of only the edge doping component, a shift of  $V_{min}$  of 13V (230 meV) is induced. SEM imaging of the NNG and PNG graphene sheet are shown in **Figure 25b** and **25c**, respectively.

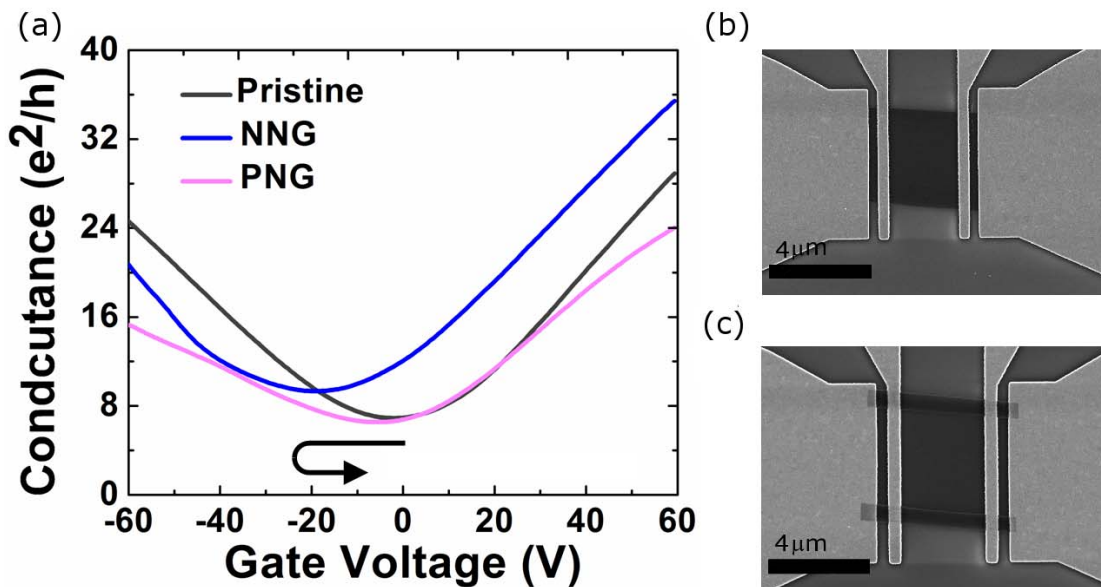


**Figure 25.** Demonstration of NNG and PPG functionality on the same graphene sheet. (a) Gated electrical testing reveals low intrinsic doping in the pristine sheet. Upon converting the sheet to NNG, a negative shift of  $V_{min}$  by -25 V is observed, indicating n-type doping. Upon converting the NNG sheet to a PNG sheet, a positive shift of  $V_{min}$  by 13 V is observed, indicating p-type doping from the edge. (b) SEM image of the NNG sheet. (c) SEM image of the same sheet after being transitioned to PNG.

In extracting the doping efficiencies, a detailed understanding of the HSQ doping mechanism is required. The process of spin-coating the HSQ resin precursor ( $H_8Si_8O_{12}$ ) atop the graphene releases approximately 65% of its H-content in the form of volatile molecular  $H_2$  [120]. Since this will diffuse out all surfaces of the film, it is assumed that a flux of  $H_2$  on par with ~30% of the resin's content will reach the graphene surface. For a film thickness of 30 nm, and an HSQ molecular mass of 424 g/mol, the flux of  $H_2$  to the basal plane of the graphene sheet should be on the order of  $1 \times 10^{16} \text{ cm}^{-2}$ , which is comparable to the atomic density of the graphene lattice. The binding energy of molecular  $H_2$  to the pristine graphene surface should be on the order of 70 meV [121]. Although there is a slight preference (~10 meV) for the molecule to situate in the center of the graphene hexagon, the 200 °C bake of the film to remove solvent provides

sufficient energy for overcoming the 14 meV diffusion barrier of  $H_2$  on the graphene sheet, making a uniform physisorption atop basal plane C-atoms likely [121]. Chemical doping via physisorption is the primary mechanism of charge transfer on the basal plane, as indicated by the lack of a significant defect population, verified by spectroscopy in **Figure 22**. The 5 keV e-beam exposure that occurs during SEM imaging is over an order of magnitude below the incident energy required for the sputtering of C-atoms [122], and will not generate vacancy defects on the basal plane. Similarly, the 100 kV e-beam of the EBL used to deliver the  $200 \mu C/cm^2$  dose to the basal plane is below the  $\sim 130$  keV threshold for knock-on displacement of  $sp^2$  bonded carbon [123], thus maintaining a pristine, physisorption doped, basal plane. Moreover, the dwell time of the e-beam over basal C- atoms is on the order of 10's of nanoseconds for a  $200 \mu C/cm^2$  dose, which is far below the sputtering rate for even 200 keV electrons, which is on par with 1 nm/s [124].

The edge of the graphene sheet is passivated through distinctly different mechanisms for the NNG and PNG sheets, which exhibit n-doped and p-doped edges, respectively. For the NNG sheet, a partially decorated H-passivated edge that is n-doped is assumed to result from the exfoliation process [111]. STM measurements of  $sp^2$  hybridized graphite edges in air at room temperature have revealed edges passivated by H [125]. Additionally, the spontaneous disassociation of gaseous molecular  $H_2$  and water vapor to form H-passivated edge defects has been shown to occur exothermically through a number of possible scenarios [126, 127]. Graphene sheet edges cleaved under ambient conditions with typical partial pressures of molecular  $H_2$  preferably form  $sp^2$  bonding [128]. The  $sp^2$  H-passivated NNG edge that exists will donate unpaired electrons for conduction [109, 129]. The PNG O-passivated, p-doped, edge is generated through the

process of replacing H with O at passivated edge C-atom sites. This transition occurs through the mechanism of knock-on displacement of light H-atoms passivating the ribbon edge, which takes place at electron energies below the threshold for C-atom displacement [130]; i.e. H can be displaced while maintaining the graphene lattice. A similar mechanism of irradiation-induced selective expulsion of H from C-films was previously demonstrated using ion irradiation [131]. The 2,000  $\mu\text{C}/\text{cm}^2$  dose that is applied to the edge of the PNG sheet effectively outgases H from the HSQ film, which facilitates the transition from a H-rich to O-rich environment around the freshly de-passivated edge C-atoms [95]. The passivation of dangling  $\sigma$ -bonds along the edge of the graphene sheet with O has been studied previously and should contribute p-carriers to the conducting graphene p-system [132].

Regarding the extent of doping at the graphene edge, only a fraction of total available edge C-atoms will contribute to chemical doping; i.e. a mixed edge exists [36]. The instant the graphene edge is cleaved during the exfoliation process, which is identical for all NNG and PNG sheets, it is assumed that a fixed, and finite, population of edge C-atoms passivated with foreign species from the ambient environment or remain chemically reactive, whereas the remainder will become chemically inert through the process of C–C edge reconstruction. There are two primary mechanisms that govern the extent of edge passivation. The first is the fraction of the graphene edge that orients with a zigzag chirality, since this is the only edge state that is predicted to facilitate chemical passivation due to the large density of states near the Fermi level, which is absent for other orientations [133-135]. The second is the availability of potential passivating species, whose absence would result in an entirely reconstructed edge, as observed by



STM imaging under vacuum [136]. Based on an abundance of ultrahigh resolution STM and tunneling electron microscopy (TEM) imaging of graphene and sp<sup>2</sup> hybridized graphitic edges cleaved in an identical manner to those produced in this work, approximately 30% of the graphene edge will oriented as zigzag [129, 137-141]. Graphene edges with a zigzag orientation have been shown to be highly chemically reactive and energetically unstable when un-passivated, making them subject to spontaneous and relatively effortless passivation with dopant species [113, 116]. Therefore, all edge C-atoms residing on zigzag portions of the sheet edge are expected to contribute to chemical doping.

The fraction of edge C-atoms participating in chemical doping is defined by the exfoliation process, which is identical for NNG and PNG sheets, and expected to remain fixed throughout the subsequent fabrication steps. The electron energies used to irradiate the graphene edge are below the values required for sputtering of C-atoms along the graphene edge or milling a new edge orientation into the sheet [122, 123]. We have verified this by exposing the HSQ-coated basal plane of a graphene sheet to the same e-beam dose used at the edge, and observed the maintenance of a pristine, defect barren, basal plane via Raman spectroscopy. The production of the PNG sheet involves the replacing of previously H-passivated edge sites with O, producing a p-type edge; thus the extent of edge doping is similar for both NNG and PNG sheets. With both sp<sup>2</sup> H and O passivation predicted to contribute 1 carrier per passivated C-atom [109, 132], similar doping levels should exist for the NNG and PNG sheet edge.

#### **4.4 Observation of Scaling Trend for Edge Defect Passivation**

The intrinsic n-type edge of the graphene sheet and scaling trend for edge doping are experimentally observed on pristine devices. Here, a scaling law of increased doping with a reduction in dimension should exist. Multiple pristine graphene sheets of varying dimension are fabricated on two separate substrates (defined as a batch). The carrier density is carefully extracted and plotted as a function of the sheet's width, **Figure 26**. All substrates are thoroughly cleaned before the application of the exfoliated graphene sheets. Once applied, the sheets are cleaned using a copious solvent rinse, and then placed under a vacuum of  $1.5 \times 10^{-6}$  T for 24 h before performing 4-point electrical testing at room temperature. Due to limitations in the exfoliation process, obtaining more than four high-quality graphene samples within a batch is difficult to achieve. A scaling law characteristic of edge doping, p-doping to increasingly stronger n-doping as the n-type edge gains dominance, is observed for all graphene sheets within a batch. The apparent background p-doping on the basal plane is attributed to adsorbates from the ambient environment [16], possibly pinned between the substrate and graphene sheet, whose doping contribution changes between batches, but is found to remain relatively constant within a batch; exhibiting similar values for flakes of similar dimensions but at different locations on the substrate.

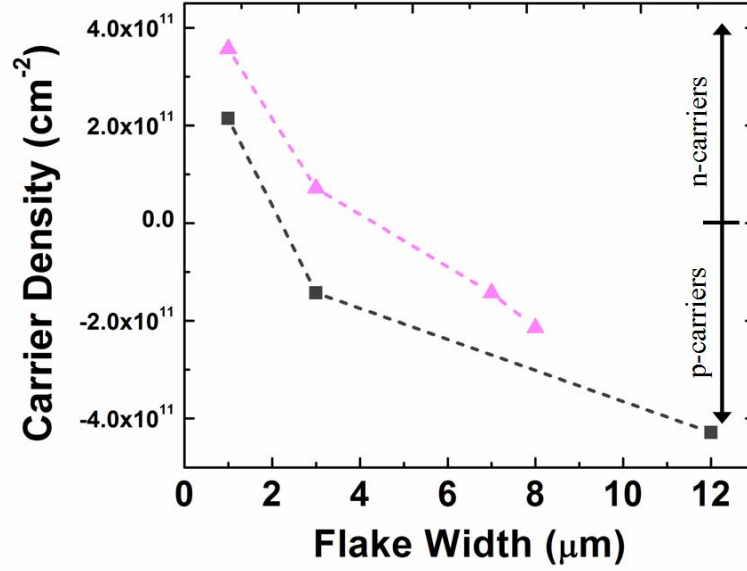


**Figure 26.** Initial observation of the scaling trend associated with edge doping. The ask-cleaved graphene flakes have an intrinsic n-type edge doping (due to H-passivation from the ambient environment) and a p-type basal plane (from physisorption and process residue). As the width of the graphene flake is decreased, a transition from p-type devices to increasingly stronger n-type devices is observed as the edge begins to dominate the carrier density.

#### 4.5 Extraction of Doping Efficiencies per Basal and Edge C-Atom

A model is developed to extract the charge donation efficiency for edge and basal C-atoms, based on the observed shift of  $V_{min}$  from multiple fabricated NNG and PNG sheets, **Figure 23**. All sheets were chosen to have a nearly identical width of 2.2 μm, defined by the exfoliation process. The length of the graphene sheet is defined by the contact metallization spacing, which is set at 3 μm to avoid doping from the adhesion layer metal into a signification portion of the graphene channel [142, 143]. Initially an entirely zigzag chirality is assumed for the orientation of the sheet edge. The total number of edge and basal plane C-atoms for the graphene sheet are extracted based on the chaining of an edge and basal unit cell, which dictates eight C-atoms per 0.983 nm of edge length and 16 C-atoms per 0.4217 nm<sup>2</sup> of basal plane, respectively. These values are

derived using a 2.46 Å lattice constant for the hexagonal C-sheet [22].

The extent of doping along the graphene edge is added to the complexity of the model by scaling back the number of edge atoms that are predicted to contribute to chemical doping; i.e. passivate. First, the effect of edge roughness is accounted for by scaling up the number of available edge C- atoms by a factor of 1.5 to account for added surface area along the contours of the cleaved edge. Second, the number of contributing edge C-atoms is scaled down by a factor of 0.3 to account only for portions of the graphene edge that orient with a zigzag chirality, which is the only orientation expected to facilitate passivation [133-135]. Both of these values are extracted based on a large sampling of high resolution STM and TEM imaging of graphene and graphitic edges produced in a similar manner to all graphene sheets used in this work [125, 129, 137-141].

The purpose of developing this model is to extract the doping efficiency for edge ( $\chi_E$ ) and basal ( $\chi_B$ ) C-atoms, in a metric of carriers donated per C-atom, based on experimentally observed shifts in the bulk carrier density between NNG and PNG sheets. By observing the role the edge plays in suppressing the n-type doping for a PNG, resulting from the competing polarity of the p-type edge and n-type basal plane, such an extraction can be made. The total carrier density in the graphene sheet ( $n_{sheet}$ ) can be expressed as the joint contribution of the basal and edge component:

$$n_{sheet} = n_E + n_B \quad (5)$$

where,

$$n_E = atoms_E \times \chi_E \quad (6)$$

$$n_B = atoms_B \times \chi_B \quad (7)$$

Here,  $\text{atoms}_E$  and  $\text{atoms}_B$  represent the total contributing edge and basal plane C-atoms, respectively. For NNG sheets, the edge and basal component sum, while for PNG sheets these components subtract. The carrier density is again tied to the position of  $V_{\min}$  through the relation provided in Equation (1) where  $C_{\text{ox}}$  in the devices produced in this work is  $11.6 \text{ nF cm}^{-2}$  for 300 nm of  $\text{SiO}_2$ . For PNG devices, an approximate 200 nm overlap of the cross-linked HSQ onto the basal plane of the sheet, verified by ultrahigh resolution SEM, is taken into account by reducing the n-type basal region, and adding a finite p-doped basal region [5]. A range of likely basal plane efficiencies, based on previously reported predictions for physisorption, from  $1 \times 10^{-5} - 1 \times 10^{-3}$  carriers per C-atom is initially assigned to  $\chi_B$  [85, 96, 108]. For each specific estimate for  $\chi_B$ , the corresponding value of  $\chi_E$  that produces the observed bulk carrier density in the graphene sheet can be determined. The result is a solution set of unique pairs of  $\chi_E$  and  $\chi_B$ , spanning all values of  $\chi_B$  that fall within the predicted basal plane physisorption range. These solution sets are produced for both NNG and PNG sheets. For NNG sheets, a range of  $V_{\min}$  shifts from -40 V to -28 V was observed, with the mean falling at -34 V. For PNG sheets, a range from -15 V to -3 V is used, with the mean falling at -9 V. The true values of  $\chi_E$  and  $\chi_B$  lie at the intersection of the NNG and PNG curves, i.e. the  $\chi$  pairs that satisfy the observed behavior of both type sheets, **Figure 27**.

The spread of projected values for  $\chi_E$  and  $\chi_B$  is indicated by the intersection of the solutions for the PNG and NNG sheets, indicated in bold outline in **Figure 27**. The true  $\chi$  values are taken at the intersection for the mean curves for both sheets, indicated with a dot. The results in **Figure 27** reveal that the passivation of C-atoms residing adjacent to vacancy defects contribute close to .85 carriers per C-atom, while physisorption atop

basal plane C-atoms contributes close to  $5.5 \times 10^{-4}$  carriers per C-atom. This makes the passivation of edge defects over three orders of magnitude more efficient than basal plane physisorption, as a route towards chemical doping. The value obtained for  $\chi_E$  lies close to the expected value, which should reside around one carrier per atom for sp<sup>2</sup> H-passivation and O-passivation [109, 132]. A strict upper limit on the potential for edge passivation is indicated in red, with two carriers per atom being possible through the pyrrolic N-passivation of graphene defects [144]. Donation efficiencies beyond this value are unlikely. Similarly, edge charge donations below 0 carriers per atom represent v pairs that are not possible for PNG sheets. The extremes of the model do slightly predict values residing in these forbidden ranges, this error is related to variability in the experimental fabrication arising from minor deviations in width of the graphene sheets and basal plane overlap of the cross-linked HSQ on PNG sheets. An estimation of  $\chi$  is also extracted from the wider graphene sheet in **Figure 25** and found to lie within the outlined spread in **Figure 27**; with  $\chi_E$  predicted to be 1.1 carriers per C-atom. This wider sheet behaves as expected, with the edge having less influence on the overall carrier density; a lower n-doping for the NNG sheet and a weaker shift from the p-doped edge of the PNG.

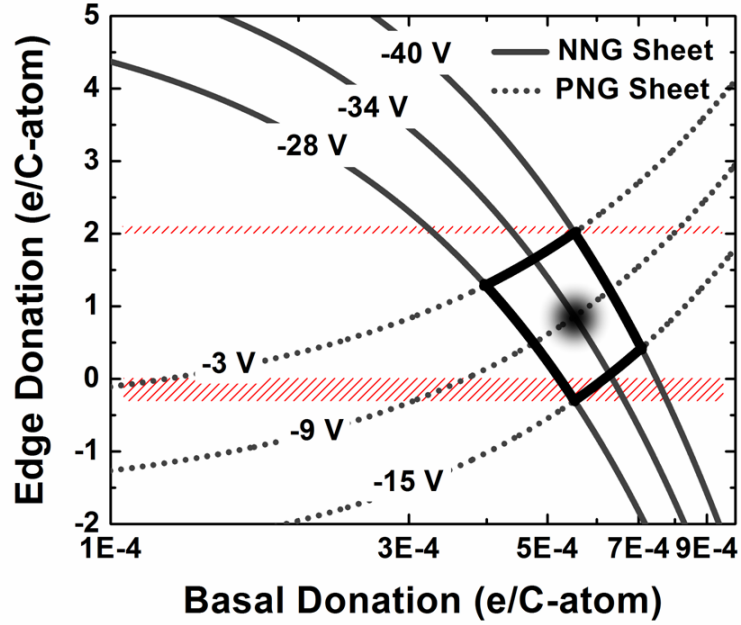


**Figure 27.** Extraction of the carriers donated per C-atom in the graphene lattice for vacancy defect passivation and physisorption. Based on the experimentally observed shift of  $V_{min}$  for multiple NNG and PNG sheets, curves representing all pairs of  $\chi_E$  and  $\chi_B$  that could produce the observed doping level in the sheet are plotted. NNG sheets are plotted for the experimentally observed shifts from -40 to -28 V, with the mean falling at -34 V. PNG sheets are plotted for experimentally observed shifts from -15 to -3 V, with the mean falling at -9 V. The intersection of the NNG and PNG curves, outlined in bold, represents the possible values for  $\chi$ . The true values for  $\chi_E$  and  $\chi_B$  are taken as the intersection of the mean curves, marked with a dot. It is found that charge donation for physisorption atop a basal atom is on the order of  $5.5 \times 10^{-4}$  carriers per C-atom and 0.85 carriers per C-atom for edge atoms. This indicates that edge atoms, or C-atoms residing adjacent to vacancy defects, are over three orders of magnitude more efficient than basal plane atoms as a route towards chemical doping.

The values of  $\chi_E$  and  $\chi_B$  can be similarly extracted from the scaling law identified on pristine graphene sheets of varying widths, **Figure 26**. Based on the observed shift of carrier density as the graphene sheet dimensions are reduced, and assuming that similar basal plane doping exists for all devices within a batch, the contribution of edge and basal atoms is calculated using an iterative technique. It is found that for both batches, the value of  $\chi_E$  converges to a range of 0.5–1 carrier per edge C-atom, while  $\chi_B$  converges to a range of  $0.5 \times 10^{-4}$  to  $2 \times 10^{-4}$  carriers per basal C-atom. These  $\chi$  values are slightly less

than those estimated from the NNG and PNG sheets. The difference is a result of changing the basal plane dopant species between the pristine graphene and HSQ-doped (NNG/PNG) sheets. The basal plane of the pristine graphene sheets is expected to be doped by O and atmospheric adsorbents [16]. The efficiency of basal plane doping is dependent on how close the dopant molecule is to the surface of graphene [121]. The physisorption of H for the NNG and PNG sheets is expected to have a more intimate contact with the basal plane of the graphene sheet than atmospheric adsorbates [108], **Figure 26**, resulting in more efficient doping. An underestimation of the basal plane doping efficiency for pristine sheets results in a similar under estimation of the edge doping component. Despite these variations in the estimates for  $\chi_E$  and  $\chi_B$ , the passivation of edge defects is still predicted to be over three orders of magnitude more efficient. This scaling trend, observed in **Figure 26**, is unique to edge doping and is highly desirable as a combatant to the onset of LER-limited mobility at narrow dimensions [145]. Based on the analysis presented in this work, a single passivated edge C-atom could provide the equivalent carrier injection to that of physisorption atop a 7 nm  $\times$  7 nm basal plane region. Additionally, this work highlights the necessity of carefully controlling the edge chemistry in nanoscale graphene devices. The heightened reactivity of the graphene edge in comparison to the basal plane makes it an attractive candidate for effortless chemical doping [113, 116], both deliberately and unintentionally. As large area sheets are patterned into nanometer features, variability in the edge passivation can begin to significantly impact the bulk carrier density, resulting in conductance modifications. Plasma etching techniques can provide interesting avenues for controlling and exploiting the edge chemistry of etched graphene devices.



In conclusion, we have directly probed two fundamental routes for chemically doping graphene sheets and shown that passivation of dangling  $\sigma$ -bonds from vacancy defect sites is inherently over 1,000-fold more efficient than physisorption on a defect-free graphene lattice, in terms of carriers donated per contributing C-atom. We have carefully extracted the chemical doping efficiencies of edge and basal atoms, in a metric of carriers donated per C-atom and present values of 0.85 and  $5.5 \times 10^{-4}$ , respectively. Using electron beam lithography for edge passivation, the interplay between doping via edge C-atoms and the basal plane physisorption was directly observed on the same graphene sheet. The leveraging of naturally occurring defect sites along the edge of a cleaved or etched graphene sheet exhibits an inherent scaling law of increased doping with reduced dimensions; carrier density growing by an order of magnitude with every 10 times reduction in width. This trend, observed here experimentally on pristine graphene, will induce large carrier densities at nanoscale widths, making it dominant over other chemical doping techniques. This Chapter demonstrates the capability of naturally occurring defect sites along the edge of graphene sheets to provide a route towards ultra-high carrier densities in nanoscale graphene systems requiring high conductance.

## **CHAPTER 5**

### **DEMONSTRATION OF EDGE-DEFECT DOPING**

#### **5.1 Motivation for the Chapter**

This Chapter is motivated by key findings in Chapter 5 and experimentally probes the passivation of edge defects in graphene interconnects. Specifically, this chapter is motivated by (1) the overwhelming efficiency of defect passivation over basal physisorption, (2) the apparent limit to carrier densities possible through interactions with the basal plane, and (3) the apparent scaling trend associated with edge doping (increased carrier density with reduced dimensions). Here, we focus on confirming the scalability of edge doped interconnects, identifying (CMOS-compatible) techniques of applying edge doping, and modeling the resistivity of sub-50 nm edge doped graphene interconnects.

During “in situ” doping, we aim to introduce dopant species during either the growth or transfer step for eased and more efficient edge passivation with dopant species. In regards to growth, these dopants could be introduced into a variety of growth techniques, including sublimation of Si from SiC [57], CVD [48], or even in the transfer/patterning of such CVD graphene films [49].

A number of doping techniques for graphene have been previously explored, the majority of which have focused on surface charge transfer to the graphene sheet. These doping techniques have been shown to have a relatively weak charge contribution, on the order of  $10^{-4}$  carriers per basal atom [96], typically limiting the induced carrier concentrations to around  $5 \times 10^{12} \text{ cm}^{-2}$ . Doping from physisorption of gaseous oxygen and water vapor [16], ammonia [108], and carbon monoxide have been previously explored [28]. Doping from charge transfer of films of various metals [142, 146], polymer

electrolytes [104], diazonium salts [84], aromatic molecules [147], and polyethyleneimine have been explored [86]. It has been previously suggested that nitrogen edge functionalization [115], by means of electrically annealing graphene nanoribbons in an ammonia environment is capable of inducing moderate n-type carrier concentrations. Similar techniques of n-type doping through nitrogen defect passivation on the basal plane of graphene sheets have been probed by reduction in graphene oxide in an ammonia environment [148], introduction of ammonia to the CVD growth process [83], arc discharge in an H<sub>2</sub> and ammonia environment and exposure to a low-power ammonia plasma [82, 149]. Most previous techniques rely on post-growth doping, which is inherently weaker and less efficient than the in situ doping technique demonstrated in this work. In addition, in some of these techniques, increased carrier concentration comes at the cost of an increased basal plane defect density, characterized by the emergence of a prominent D-peak during Raman imaging and poor mobilities of 200 – 400 cm<sup>2</sup>/Vs [83, 150].

## **5.2 Experimental Procedure**

Graphene devices in this work are exfoliated from Kish graphite onto 300 nm of thermally grown SiO<sub>2</sub> on highly doped silicon (to serve as a back-gate). Cleaning of the substrate is preformed prior to exfoliation—the substrate is baked for 1 h at 400 °C in a nitrogen ambient (N-ambient). An N-ambient is produced using a Terra Universal Dual Purge system. Relative humidity is monitored in situ and kept below 5% using a 4700 SCCM high-flow purge of N<sub>2</sub>. An internal positive pressure of ~180 mT is maintained. Exfoliation of the graphene sheets is carried out in the same N-ambient, without removal of the substrate, using a procedure similar to exfoliation in air presented previously in

Chapter 2. The substrate is then removed from the N-ambient and monolayer and few-layer graphene devices are identified optically and verified using Raman spectroscopy. All processing steps post-exfoliation are kept below 200 °C to ensure that the N-passivated bonds remain intact. Nitrogen passivation has been previously probed using x-ray photoelectron spectroscopy and shown to have binding energies on the order of 400 eV [144], making it robust throughout the processing temperatures used in this work. Contact metallization is patterned using electron beam lithography and a metal evaporation of Ti/Au (20 nm/80 nm) followed by a liftoff procedure. The devices are then pumped for 24 h at a pressure of  $1.5 \times 10^{-5}$  Torr before performing four-point electrical testing under vacuum. A pulsed gating technique is used to minimize hysteresis from previous gate sweeps and identify true values for the minimum conductivity point [117]. A double-sweep of the gate voltage is performed on all devices to verify the suppression of the hysteresis and  $V_{min}$  stability with multiple sweeps. SEM images are taken post-electrical testing to determine the graphene interconnect linewidth.

### 5.3 Scaling Edge Doped Interconnects

Electrical testing of two representative devices is shown in **Figure 28a**. These devices are on the same substrate and both devices are n-doped but the carrier concentration at zero gate bias is different between the two. The corresponding SEM images of the graphene flakes are shown in **Figure 28b**. The devices are found to exhibit mobilities in excess of  $5,000 \text{ cm}^2/\text{Vs}$ .

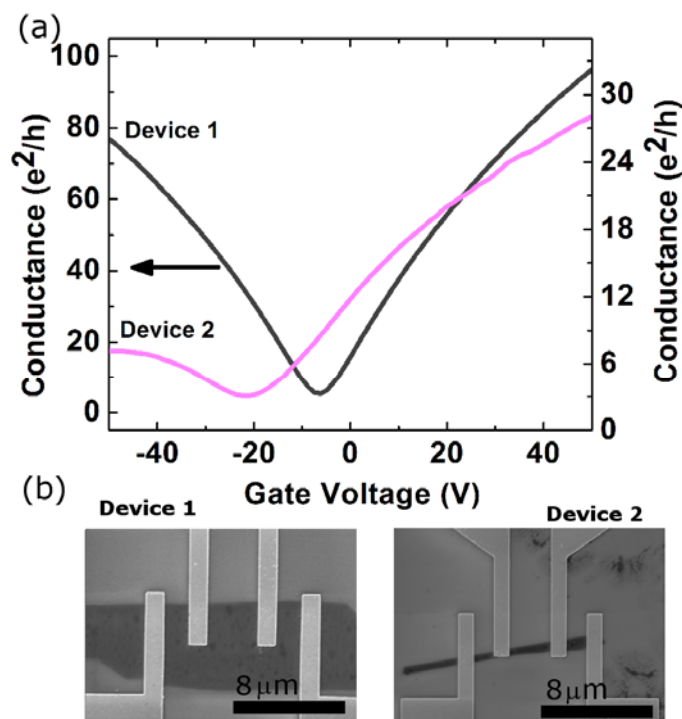


**Figure 28.** Gated electrical testing of two graphene sheets exfoliated in a nitrogen-rich environment. Having the dopant specie present as the interconnect is freshly cleaved results in efficient passivation of the edge. (a) Testing of the two devices reveals two different levels of n-type doping. (b) SEM imaging reveals that the narrower of the two sheets exhibits a larger n-type doping.

Raman spectroscopy is performed on the graphene basal plane in **Figure 29**. The lack of a D-peak for the devices studied in this work indicates that a pristine basal plane, with minimal defect density, is maintained when using this technique.

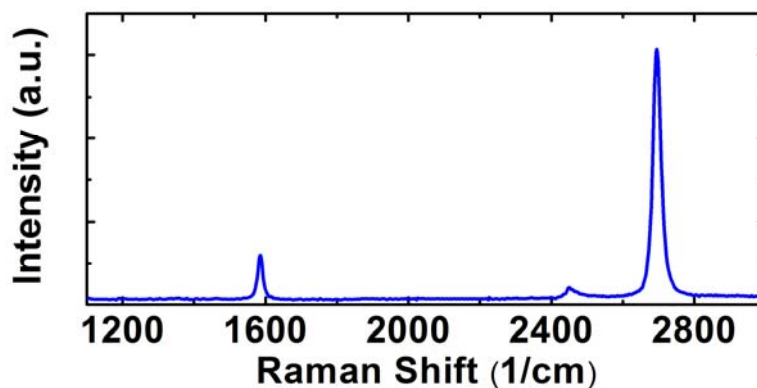


**Figure 29.** Raman spectroscopy of a graphene sheet exfoliated in a  $N_2$  glovebox reveals a pristine basal plane. No D-peak is observed, indicating a basal plane free of defects.

Multiple in situ doped graphene devices across four separate process batches are fabricated and tested for their electrical response. Electrical measurements of all devices reveal n-doped graphene, from the negative values of  $V_{min}$ , **Figure 30a**. The carrier density as a function of flake width is plotted, **Figure 30b**. A trend of increased n-type doping with reduced flake dimensions is observed for all devices within a batch, indicated by dashed lines. Since the number of edge dopant species remains fixed with width scaling, an increasing n-type carrier concentration is observed.

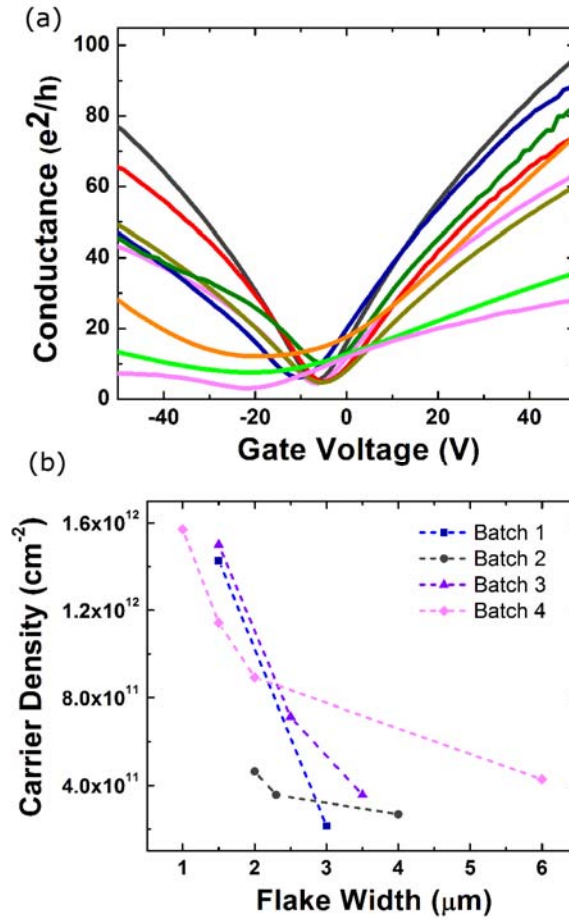


**Figure 30.** Experimental verification of the scaling trend associated with edge doped interconnects. (a) Gated electrical testing of multiple interconnects with varying linewidth. (b) A plot of the carrier density of these devices versus the interconnect width reveals increasing n-type doping with scaled dimensions. Positive values of the carrier density represent n-type carriers.

The n-type doping of the graphene ribbons (GR) is attributed to nitrogen passivation of dangling  $\sigma$ -bonds along the ribbon edge - these dangling bonds are thought to occur at the time of cleaving during the exfoliation process. It can be seen that there is a small  $V_{min}$  offset between substrates. This variation is attributed to basal plane doping from process-related residues, which despite thorough cleaning, induce a small background doping level. Though this doping offset varies between process batches, it is reasonable to assume that it remains fixed within a single batch since the substrate and all devices fabricated atop it are exposed to identical process conditions. Additionally, devices of similar widths but within the same substrate exhibit comparable doping, indicating little spatial variation in doping within a given substrate.

#### **5.4 Identification of Techniques for In Situ Edge Doping**

Graphene defect sites can undergo various C–C reconstructions in an attempt to form a stable lattice. In terms of defect passivation with foreign elements, zigzag edges are of greater significance than armchair edges due to their large density of states near the Fermi level [36, 151-154]. This has been verified experimentally through scanning tunneling microscopy imaging along the edge of graphene sheets [137]. Zigzag edges with dangling  $\sigma$ -bonds are not stable and have a natural tendency to undergo reconstruction in the form of two adjacent hexagons transitioning into one heptagon and one pentagon [127, 155-157]. For this reason, when attempting to passivate defects of fresh graphene vacancies, the choice of element for passivation must provide an energetically favorable alternative to C–C reconstruction. Nitrogen passivation of dangling bonds has been shown to be capable of providing a stable alternative [158-160]. In addition to this, it has been shown that incorporation of nitrogen into the graphene

lattice is most energetically favorable along the ribbon edge [158, 160], providing in situ nitrogen doping with an inherent spatial selectivity of decorating only the edge of the GR. Doping using this technique occurs through the generation of pyridinic-N and pyrrolic-N lattices [144], who donate 1 and 2 conducting electrons to the  $\sigma$ -system, respectively.

In situ doping of graphene is especially attractive as a counterpart to the growth or transfer of graphene from various substrates (post-growth) such as SiC, Cu, Ni. Defects are currently an unavoidable reality to the fabrication of graphene devices. Defects have been shown to be generated during the growth of epitaxial graphene [161], CVD growth and transfer [83], the reduction in graphene oxide [59], the tailoring of graphene via etching [35], and exposure of graphene to electron beam irradiation [162]. It has been shown that stable [45], un-passivated, basal-plane defects in the form of Stone–Wales configurations and interstitial-vacancy recombination can readily exist in graphene sheets [163, 164]. These defects induce short-range scatterers to the material, whose role is to limit mobility at high carrier concentrations [29]. It has been observed that in the event of defect generation in vacuum, C–C reconstruction will occur rapidly, with a stable un-passivated defect site forming in a matter of seconds [136]. The in situ doping technique presented in this work demonstrates that by performing the graphene growth process in an environment rich with the passivating specie, passivation at the time of defect generation can lead to an efficient conversion of un-passivated defects to dopant sites, with unique opportunities for spatial selectivity. By employing in situ doping of edge defect sites alone, n-type carrier concentrations on the order of  $1.5 \times 10^{12} \text{ cm}^{-2}$  can be observed while maintaining high mobility. Edge doping is speculated to provide a robust, long-term doping mechanism for graphene, given the energetically stable structure of an



N-passivated edge. Post-passivation, the edge is predicted to become chemically inert, and provide a constant doping, excluding the breaking of N–C bonds or generation of fresh defects.

### 5.5 Extrapolation and Modeling of Edge Doping Trend

A model is developed to benchmark the performance of edge doped GNR interconnects. Regarding GNRs at the local interconnect level, reduced latency over Cu is expected to stem from the confluence of geometrical and electrical advantages of graphene. The 2D geometry, alone, of the graphene sheet will result in significant reductions in the line-to-line capacitance ( $C_{\text{line}}$ ) over Cu. GNRs with moderate LER scattering are expected to outperform Cu in regards to the RC delay at 9 nm linewidths due purely to these reductions in  $C_{\text{line}}$  [71]. The focus of this thesis is to provide a CMOS-compatible means of combating LER in order to increase the linewidth at which GNRs can outperform Cu interconnects in regards to this RC delay. It should be noted that peripheral benefits relating to electromigration failure are expected as well, but discussed elsewhere [4].

The starting point for this model is to extrapolate the carrier density of an edge doped GNR down to sub-50 nm linewidth. Specifically, the experimental scaling trends shown in **Figure 26** and **Figure 30** will be extended using a simple model. A GNR interconnect is constructed based on a lattice constant of 2.46 Å [22], which yields eight available edge C-atoms in the graphene lattice for every .93 nm of GNR length. Each passivated edge C-atom is predicted to contribute .85 carriers to the conducting  $\pi$ -system based on the value of  $\chi_E$  obtained in **Figure 27**. For this model, we will assume that all C-atoms along the GNR edge are passivated with N. Our GNR is subject to realistic

levels of LER comparable to that observed experimentally in our process [3, 74]. While reducing mobility as described in Equation (1) of Chapter 1, this LER will also increase the number of edge atoms and as such we scale up the available edge C-atoms by a factor of 1.2. As expected, an order of magnitude increase in the GNR carrier density is observed for every  $10\times$  reduction in interconnect linewidth. This is shown below in **Figure 31**.

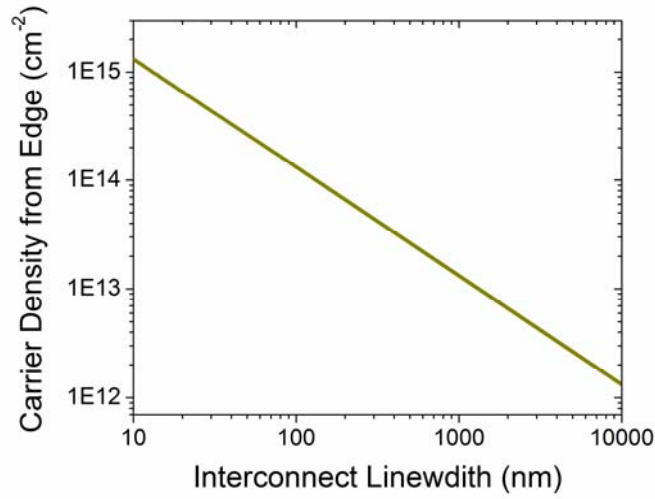


**Figure 31.** Modeling of the scaling trend for the carrier density in efficiently edge doped GNRs.

Based on this extrapolation, it can be seen that the contribution to carrier density from edge passivation, alone, becomes comparable to basal plane physisorption at 1  $\mu\text{m}$  linewidth; basal techniques are limited to values below  $1 \times 10^{13} \text{ cm}^{-2}$ . Below 1  $\mu\text{m}$ , the edge continues to gain dominance and ultimately approaches carrier densities beyond  $1 \times 10^{15} \text{ cm}^{-2}$  at a 10 nm linewidth. Aside from the benefits of increased carrier density, fluctuations in the edge passivation of fabricated devices can lead to significant device-to-device variability for GNRs. For example, when using a plasma to etch nanoscale

GNRs, the composition of the plasma may need stricter process control to avoid variations in the edge passivation, carrier density, and resistivity while being patterned.

We extend our model to provide a preliminary assessment of GNR resistivity in comparison to 1:1 AR Cu interconnects. While a complete system-level modeling is beyond the scope of this thesis and provided elsewhere [17, 68, 69], a preliminary assessment can provide a foundation for future research. We begin by taking a graphene sheet with a length (L) set at 500 nm and variable linewidth (W). We support the GNR with an underlying SiO<sub>2</sub> dielectric. The phonon-limited mobility of graphene on oxide will limit the values of  $\mu$  to 40,000 cm<sup>2</sup>/Vs [19]. The Fermi level in the graphene sheet will be initially pinned at 520 meV, representing a basal physisorption-inducting intrinsic carrier density of  $n = 5 \times 10^{12}$  cm<sup>-2</sup>. This value is on par with the limits to basal plane doping as well as a value of  $\chi_B = 5.5 \times 10^{-4}$  carriers per C-atom in the lattice [6]. Two interconnect models are generated. An intrinsic GNR will have no chemical passivation of the edge contributing to doping (i.e., an entirely C-C reconstructed edge). An edge doped GNR will have entirely N-passivated edge atoms and whose carrier density follows the trend of **Figure 31**. Both GNRs will be subject to experimentally observed LER-limited mobility that is published in our sister work [74]. This LER-limited mobility will take the form of Equation (3) in Chapter 1 and is applied using Matthiessen's rule. The resistivity of these GNRs are compared with optimistic projections for the resistivity 1:1 AR Cu in **Figure 32** below [1, 17].

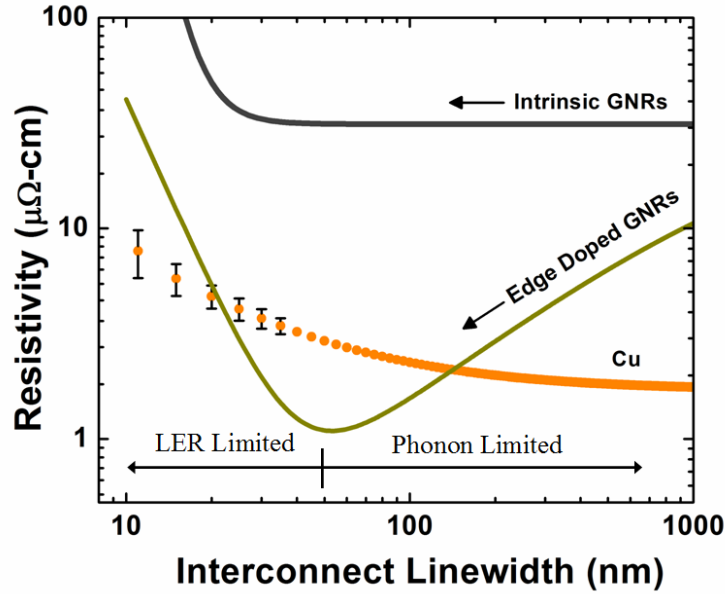


**Figure 32.** Resistivity scaling of intrinsic and edge doped GNRs based on simplified graphene models. The onset of LER-limited mobility is applied at linewidth below 50 nm. Edge doped GNRs show orders of magnitude lower resistivity than intrinsic GNRs, while outperforming Cu for a narrow window of linewidth.

It can be seen that intrinsic GNRs and/or GNRs doped through basal plane physisorption techniques, which are subject to current levels of LER, exhibit resistivities nearly an order of magnitude above 1:1 AR Cu interconnects. However, with the application of edge doping, GNRs are expected to provide lower resistivity down to 20 nm linewidths. It should be noted that these GNRs are subject to drastic LER-limited mobility comparable to current processing maturity. As the LER is smoothed out, the GNR resistivity will continue to improve and extend graphene's performance to larger linewidths.

In conclusion, it is shown that in situ doping techniques are highly attractive for the efficient incorporation of dopant species into the graphene lattice. By carrying out the exfoliation of graphene in a N-ambient, the dopant specie can play an active role in minimizing C–C reconstruction by passivating defect sites, thereby producing n-type

GNRs. The presence of the passivating specie at the moment of defect generation is thought to be essential to the minimization of un-passivated defect sites, whose only role is to limit graphene's mobility. In situ doping techniques are highly attractive as counterparts to the growth and transfer processes, where natural kinetics can be exploited to provide unique avenues for the direct embedding of dopant atoms, an opportunity lacking in post-growth doping techniques. Modeling efforts of edge doped GNRs suggest that the carrier density will increase by an order of magnitude for every  $10\times$  reduction in linewidth. Below  $1\text{ }\mu\text{m}$  linewidth, edge doping is expected to dominate over surface physisorption techniques and provide a path towards lower resistivity interconnects when compared to Cu.

## CHAPTER 6

### PERIPHERAL APPLICATION IN NON-VOLATILE MEMORY

#### 6.1 Motivation for the Chapter

In the process of exploring techniques for removing charged impurity scatterers in graphene using dielectric screening [165, 166], we unearthed a novel technique of enhancing the hysteresis in graphene devices. The unique 2D nature of graphene presents a wealth of opportunity to disrupt the state of the art for a number of devices beyond interconnects, including non-volatile (Flash) memory. Here, we present a novel device design capable of room temperature hysteresis beyond what was previously capable in carbon electronics.

Atomically thin carbon devices are highly attractive for sensor applications, owing to their heightened dependence of bulk conductance to adsorbates and charges in the vicinity of the channel [28]. Historically, the ability of such devices to *sense* relied on a modification of the carrier density by the external species, which trickles into a measurable deviation in conductance [167]. Memory applications are perfect niches for such carbon devices, where a drive for operation based on single-electron sensitivity exists [168, 169]. Thus far, the most promising memory devices in CNTs and GNRs have taken the form of floating-gate architectures, where hysteresis from the screening of locally pinned charge results in a shift in carrier density and, ultimately, a displacement of the threshold voltage [169]. However, such devices require a bandgap and are limited to low-temperature operation [167], with gapped GNRs being additionally plagued by vast reductions in mobility [34]. New routes for producing hysteresis and enhancing the sensitivity of quasi-2D systems are expected to have a far-reaching impact for carbon

devices [170].

In this Chapter, we present a fundamentally new approach to producing hysteresis in graphene devices. Field-driven injection of charge into the underlying SiO<sub>2</sub> substrate is used to modify the layout of charged-impurity scatterers seen by the graphene channel. By coating the device with the dielectric material dimethylformamide (DMF), “low-conductance” and “high-conductance” states are observed by disrupting and reinstating the dielectric screening process. Here, external species modify the conductance through their role as scatterers rather than dopants. This paradigm shift in the sensing mechanism is expected to excite new avenues for ultrahigh sensitivity in carbon devices. Atomically thin carbon devices offer the possibility of designing nanoscale ballistic systems that become diffusive by the addition of a single scattering charge.

## **6.2 Experimental Procedure**

Devices are fabricated using mechanically exfoliated graphene applied to a Si substrate with 300 nm of thermally grown oxide [16]. The application of graphene occurs while the substrate is at an elevated temperature ( $> 200$  °C) to fully desorb bound water molecules [171], allowing for an intimate contact. The graphene flakes on scotch tape are loaded into a standard glovebox that maintains a dry N<sub>2</sub> environment. The substrate is prepared using a solvent rinse and a 10 s exposure to a low-power oxygen plasma to remove organic residues. The substrate is loaded within the same glovebox and placed on a hot plate at 300 °C to bake for 24 h. The graphene is applied via gentle pressure to the scotch tape in contact with the hot substrate surface. The substrate is then removed from the hot plate/glovebox for further processing. Monolayer graphene is identified by optical contrast and verified using AFM and Raman spectroscopy [172]. Contact metallization is

patterned using electron-beam lithography, followed by evaporation of a Ti/Au (20 nm/80 nm) stack. A total of 15 devices were fabricated. The channel length is defined by the inner contacts and is pinned at 3  $\mu\text{m}$  to avoid doping effects from the metallization. The channel width is defined by the exfoliation. The device is pumped for 24 h at a vacuum of  $1.5 \times 10^{-6}$  Torr to remove atmospheric adsorbates. When drop casting is performed, the vacuum is broken and a loop of the back-gate bias is continually pulsed using hold and off times of 1 and 15 ms, respectively. Four-point electrical testing at a 50-mV drain–source bias is used to remove contact resistance ( $r_c$ ) from our measurements. However,  $r_c$  was extracted by comparing the four-point to two-point measurements and found to be  $\sim 30 \Omega$ , which is over an order of magnitude below our channel resistance. Four-point testing and a pulsed back gate are used for all measurements in this letter.

### 6.3 Demonstration of Room-Temperature Hysteresis

Electrical testing of a single device is shown in **Figure 33**. The pristine device is exposed to the ambient environment and exhibits no observable hysteresis **Figure 33a**. After 30 s of ambient exposure, a 10- $\mu\text{L}$  film of DMF is drop cast using a microsyringe. A 3-min break-in time is attributed to mechanical settling of the probe tips, which could be disturbed during the drop casting, as well as the formation of a significant trap population below the channel. A stable room-temperature conductance gap of nearly one order of magnitude ( $2\text{--}20 e^2/h$ ) is demonstrated, **Figure 33b**. The low-conductance state on the forward sweep is on par with the pristine unscreened conductance state observed in **Figure 33a**. The high-conductance screened state agrees with the previous values for DMF coating of graphene [165], confirming that the hysteresis results from a turning-on



and a turning-off of the dielectric screening process. The values presented in [171] were internally verified on a batch of devices in our setup. After 8 min, the hysteresis becomes unstable due to evaporation of the DMF.

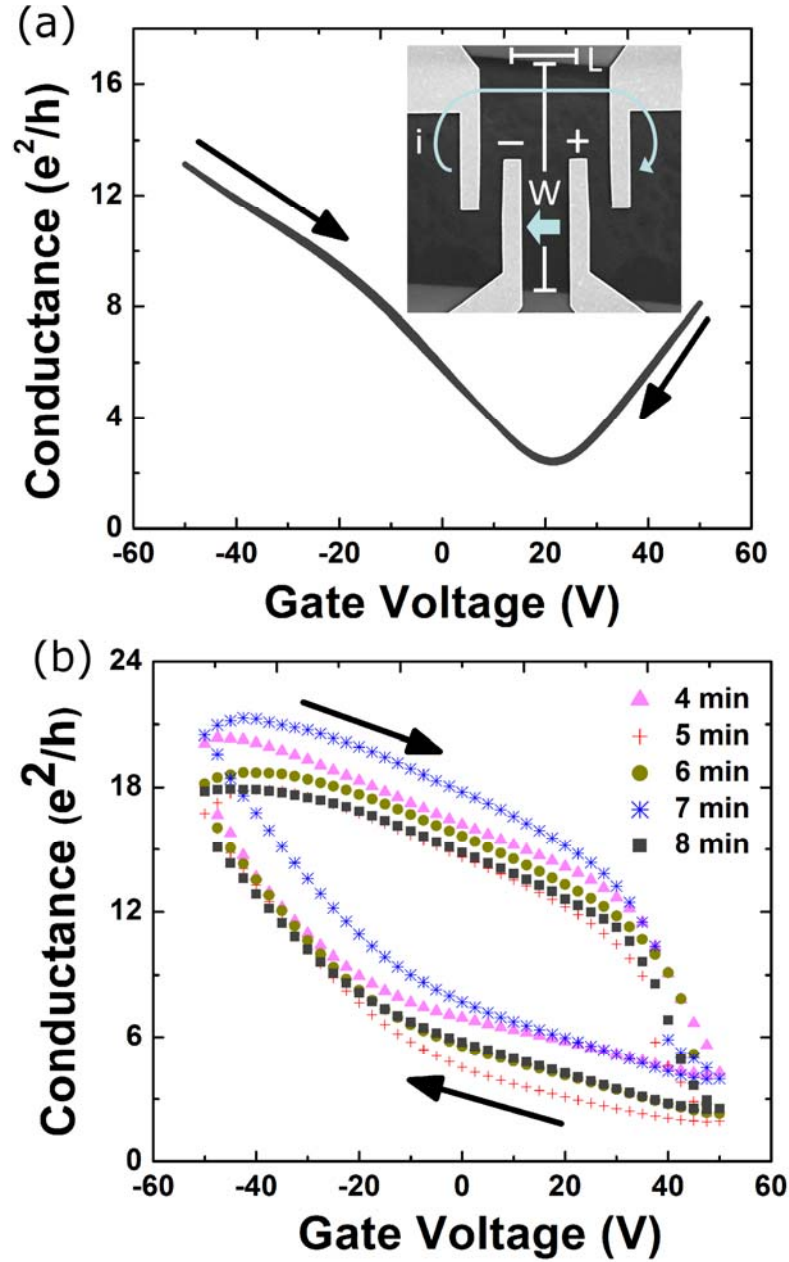


**Figure 33.** Demonstration of a non-volatile graphene memory device. (a) Gated electrical testing of a pristine graphene sheet atop a  $\text{SiO}_2$  dielectric reveals no hysteresis. Pulsed-gate testing is used to remove charge trapping in adsorbates. (b) An overlying screening dielectric is applied and a room-temperature hysteresis of nearly one order of magnitude is observed.

## 6.4 Explanation of the Hysteresis Mechanism

Mobility in graphene devices is severely limited by charged impurities in the vicinity of the channel [20], resulting in significant reductions in conductance. Coating graphene with a dielectric has been shown to be capable of screening charged impurities. Over one order of magnitude improvement in conductance with proper selection of the dielectric and a heavily scattered channel is possible [106, 173]. There are two fundamental mechanisms that drive hysteresis in carbon devices supported by SiO<sub>2</sub>. The first is charge trapping of adsorbed water vapor and hydroxyl groups on or in proximity to the carbon channel [174]. The second mechanism involves field-driven emission of charge from the carbon channel into the underlying substrate [169, 175]. The millisecond back-gate pulse times used in this work occur on a time scale more rapid than the charge-trapping time associated with atmospheric adsorbates, which are on the order of 0.1–10 s [117], making charge injection from the graphene the primary driver of hysteresis. Modeling of the injection of electrons from CNTs into the underlying oxide has been previously carried out [175, 176]. The injection and release of electrons locally embedded in the SiO<sub>2</sub> are functions of the electric field ( $E_{\text{int}}$ ) at the channel/oxide interface. The magnitude of  $E_{\text{int}}$  is a function of the external potential, which is dominated by the carrier density ( $n$ ) in the graphene device. The back-gate voltage is tied to  $n$  through the expression provided in Equation (1). Here,  $C_{\text{ox}}$  for 300 nm is 11.6 nF/cm<sup>2</sup>, and  $V_g - V_{\text{min}}$  is the displacement of the minimum conductivity point (i.e., where the Fermi level is pinned in the vicinity of the Dirac point) from zero gate bias. Carrier densities beyond  $2 \times 10^{12} \text{ cm}^{-2}$  should exist in the graphene sheet at the extremes of the gate voltage loop. Based on our AFM measurements, the graphene sheet is taken as a 3.5 Å-thick uniform plane of charge

[172]. An intimate contact with the substrate, which is oxide coated with a single layer of silanol groups, is assumed given the elevated temperature of the substrate during exfoliation [171, 177], producing an interfacial spacing of approximately 1 Å ( $d_{\text{int}}$ ). The magnitude of the electric field resulting from the charge in the graphene channel can be expressed using the Poisson equation:

$$E_{\text{int}} = \frac{qn}{\epsilon} d_{\text{int}} \quad (8)$$

This results in electric fields at the interface on the order of 0.2 V/nm, which is comparable to the breakdown field for SiO<sub>2</sub> [169, 178], facilitating the local embedding and release of electrons directly from the channel.

Injected electrons into the oxide reside close the carbon/SiO<sub>2</sub> interface at depths on the order of 3 nm [117, 175, 176]. The Thomas–Fermi screening length ( $\lambda$ ) for graphene is defined as  $\lambda = 1/(4k_F\alpha)$ , where  $k_F = (\pi n)^{1/2}$  and  $\alpha = 2e^2/\hbar v_f (K_1 + K_2)$  [106]. For this specific system,  $K_1$  is the dielectric constant of SiO<sub>2</sub>, and  $K_2$  is the dielectric constant of DMF, which are ~3.9 and ~36, respectively. Assuming a carrier concentration of  $n = 1 \times 10^{12} \text{ cm}^{-2}$ , the screening length for injected charge is over 25 nm. Since the charge from the graphene is injected at narrow depths, even multilayer graphene systems are not sufficient to effectively screen trapped oxide charge, resulting in a residual electric field penetrating into the DMF film. An explanation of the hysteresis mechanism is shown in **Figure 34**. At large positive values of the gate bias, electrons are emitted from the graphene and embedded into the underlying oxide, producing a new scattering layout of negatively charged impurities. The result of these scatterers is a low-conductance (unscreened) state observed on the leftward sweep of the gate bias. These scatterers are

eventually released at large negative values of the gate voltage, ushering a return to the high- conductance (screened) state seen on the rightward sweep of the gate bias.

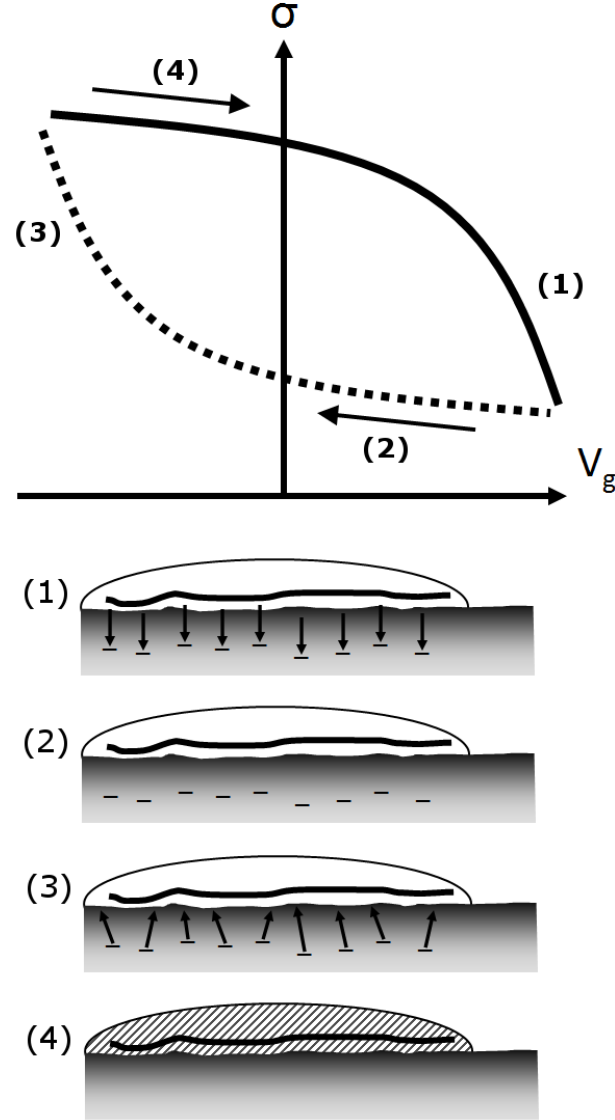


**Figure 34.** Explanation of the mechanism of hysteresis. (1) At large positive values of the gate voltage, electrons are emitted from the graphene channel and embed at shallow depths in the underlying gate dielectric. (2) These embedded electrons disrupt the dielectric screening process, and function as charged impurities working to lower the conductivity. (3) At large negative values of the gate voltage, the electrons are released from the oxide. (4) Once the electrons are released, a return to the high conductance state is observed.

From a scalability standpoint, the operating voltage required for charge injection, i.e., switching, can be vastly reduced by thinning the gate dielectric beyond 300 nm. In terms of the conductance gap, atomically thin carbon devices (CNTs and GNRs) offer an entirely unique platform for ballistic transport across micrometer lengths. The ultimate limit for devices leveraging single-electron sensitivity is first envisioned here, where the transition between ballistic and diffusive transport can occur in graphene channels from the self-emission of a lone charged scatterer.

In conclusion, a graphene device exhibiting a room-temperature conductance hysteresis of nearly one order of magnitude has been demonstrated. It is shown that, by coating graphene with a dielectric, a transition from a screened “high-conductance” state to an unscreened “low-conductance” state can be produced. The disruption and reinstating of the steady-state screening process is found to be driven by charge injection from the graphene channel. This Chapter has presented the first demonstration of a potential floating-gate device where external charge is utilized as a scattering mechanism to modify conductance, which is a new approach to enhancing the sensitivity of atomically thin carbon devices.

## CHAPTER 7

### CONCLUDING REMARKS AND FUTURE RESEARCH

In this thesis we provide contributions to the chemical doping of graphene sheets, with a particular focus on introducing graphene as a replacement to Cu at the local interconnect tier of CMOS ICs. Graphene possess entirely unique electrical properties and as such, provides the opportunity to advance a diverse portfolio of technologies. Regarding local interconnects, reduced latency can stem from the confluence of reduced capacitance from the 2D geometry of the graphene as well as reduced electrical resistivity – the latter is the focus of this thesis as low line-to-line capacitance is intrinsic to the atomically thin graphene sheet. As graphene represents the first truly 2D conductor, traditional chemical doping techniques of bulk 3D conductors – embedded dopant impurities – should be abandoned for new techniques that effectively dope graphene into high conductance nanoscale devices. In this thesis, we introduce novel doping techniques that involved surface physisorption and the tailoring of edge chemistry. These techniques are expected to provide new avenues for introducing graphene interconnects/devices into CMOS environments, as well as capturing new applications for graphene as an electrical conduit. Our approach to chemical doping is summarized below.

In Chapter 2, we begin by benchmarking the electrical resistivity and breakdown current density of intrinsic (as-fabricated) GNRs [3, 4]. We fabricate GNRs at a linewidth ranging from 18 nm to 52 nm as both Cu and graphene are subject to edge scattering at these dimensions. We provide one of the most complete experimental collections of narrow graphene interconnects and the first demonstration that GNR resistivity can be comparable to 1:1 AR Cu at a similar linewidth. This Chapter provides

motivation for the subsequent chemical doping work as our GNRs are still far from meeting their theoretical resistivity of  $1.2 \mu\Omega\text{-cm}$ .

In Chapter 3, we begin our approach to chemical doping by through a surface physisorption technique [5]. That is, we bring dopant species into contact with the basal plane of the graphene sheet and control the carrier density through the charge transfer that occurs. Basal plane techniques are a natural starting point as they have the advantage of being non-invasive, maintaining the graphene crystallinity, and preserving carrier mobility. We develop our basal plane technique by coating graphene with thin films of HSQ. We then tailor the chemical composition of the HSQ, via cross-linking, to provide both n-type and p-type doping to graphene in a tunable manner. We use HSQ to demonstrate the first basal technique that is both tunable (in regards to the induced carrier density) and capable of providing n-type and p-type complimentary doping. This being said, we demonstrate an order of magnitude increase in electrical conductivity for both p-type and n-type carriers. Next, we use the HSQ doping technique to demonstrate the first chemically doped p-n junction in graphene. This demonstration opens the door for tremendous future research focused on p-n junctions. Specifically, this includes Klein Tunneling devices, electron optics/lenses, and waveguided interconnects. We provide a preliminary basis for such waveguided interconnects in Chapter 3.

In Chapter 4, we use the HSQ doping technique of Chapter 3 to provide a direct comparison between two fundamental methods of chemically doping graphene: (1) basal physisorption and (2) vacancy defect passivation [6]. This Chapter is motivated by the apparent limits of basal techniques to carrier densities on the order of  $5 \times 10^{12} \text{ cm}^{-2}$ , which are observed in Chapter 3 and confirmed by other groups. By controlling the chemical

passivation of naturally occurring edge defects, we are able to extract the doping efficiency for physisorption and defect passivation in a metric of carriers donated per available C-atom in the graphene lattice. We show that the chemical passivation of a vacancy defect is over  $1,000\times$  more efficient than physisorption. Specifically, we present values of 0.85 and  $5.5\times 10^{-4}$  carriers donated per C-atom for passivation and physisorption, respectively. Moreover, we provide the first observation of a scaling trend possible when passivating naturally occurring defects along the edge of etched interconnects, which we refer to as “edge doping.” This edge doping results in increased carrier densities with reduced linewidth and is extremely advantageous for CMOS scaling.

In Chapter 5, we provide the first experimental demonstration of a graphene interconnect that was edge doped using an in situ technique [7]. Also, we verify the scaling trend of increased carrier density with reduced dimensions that is inherent to edge doping. We provide the first evidence that efficient edge passivation must combat the C-C reconstructions that normally occur and render the edge chemically inert. We demonstrate that such reconstructions can be overcome by (1) having the passivating specie present at the instant the edge is cleaved and by (2) using specie that provide an energetically favorable alternative to C-C reconstruction. We capture both of these requirements via exfoliating graphene in a N-rich environment ( $N_2$  purged glovebox), demonstrating in situ edge doped interconnects whose carrier density increases with scaling. Lastly, we extrapolate these edge doping trends and show that ultrahigh carrier densities can be induced in nanoscale graphene devices. We compare such devices to 1:1 aspect ratio Cu at sub-50 nm linewidth, and benchmark the dimensions at which edge chemistry dominates the carrier density over interactions with the basal plane. Lastly, we



provide the foundation for future research by which edge doping can be applied through CMOS-compatible plasma exposures. That is, edge doping can be applied using a plasma etch containing the dopant specie. Future research should target the experimental fabrication of sub-50 nm edge doped graphene interconnects using such plasma-induced passivation of the edge, possibly via dense N-plasmas.

In Chapter 6, we provide contributions to non-volatile graphene memory through the tuning of hysteresis in gated devices [8]. Specifically, while exploring techniques of improving interconnect conductivity via dielectric screening, we unearthed a novel technique of enhancing the hysteresis in graphene devices. We use this hysteresis technique to demonstrate a room-temperature hysteresis gap of nearly one order of magnitude, with potential for further scaling and application in ultrahigh resolution chemical sensors. Lastly, we provide additional peripheral contributions to the realm of graphene devices [9-11].

A summary of our approach to the chemical doping of GNRs interconnects is provided below in **Table 1**.

**Table 1.** Summary of our approach to the chemical doping GNR interconnects.

Chapter 2	<p style="text-align: center;"><b>Benchmarking of Intrinsic GNRs</b></p> <p>We begin with benchmarking the electrical resistivity and breakdown current density of as-fabricated (intrinsic) GNRs. GNRs are fabricated at a linewidth between 18 nm to 52 nm as this range includes the onset of edge scattering for both Cu and graphene. The contributions of this Chapter include a demonstration of comparable resistivity between GNRs and 1:1 AR Cu as well as GNR breakdown current densities over 1,000× greater than Cu.</p>
Chapter 3	<p style="text-align: center;"><b>Basal Plane Doping</b></p> <p>Next, we look to improve upon the intrinsic GNRs of Chapter 2 by applying chemical doping techniques to reach the theoretical resistivity of 1.2 <math>\mu\Omega\text{-cm}</math>. We begin our approach to chemical doping through a non-invasive physisorption technique on the graphene basal plane. The basal plane is a natural starting point as the crystallinity of graphene and the carrier mobility can be maintained. The contributions of this Chapter include the first tunable complimentary doping technique for graphene and a demonstration of the first chemically doped p-n junction in graphene.</p>
Chapter 4	<p style="text-align: center;"><b>Comparison of Basal and Defect Doping</b></p> <p>Next, we provide a direct comparison between two fundamental methods of doping graphene: (1) basal plane physisorption and (2) vacancy defect passivation. This Chapter is motivated by the apparent limitation of basal techniques to a carrier density of <math>\sim 5 \times 10^{12} \text{ cm}^{-2}</math>. The contributions of this Chapter include an extraction of the chemical doping efficiencies of physisorption and defect passivation (in a metric of carriers per available C-atom), a demonstration that defect passivation is 1,000× more efficient than physisorption, and the identification of the potential for edge defect passivation.</p>
Chapter 5	<p style="text-align: center;"><b>Demonstration of Edge Defect Doping</b></p> <p>Next, we experimentally fabricate graphene interconnects that are doped through edge defect passivation. We identify that such edge doping requires that the dopant specie be present at the moment the edge is formed and be energetically favorable to C-C edge reconstructions, which render the edge chemically inert. The contributions of this Chapter include benchmarking of the dimensions where edge doping dominates over basal plane doping, verification of a scaling trend associated with edge doping, and a preliminary modeling effort of edge doped GNR interconnects.</p>
Chapter 6	<p style="text-align: center;"><b>Peripheral Application in Non-Volatile Memory</b></p> <p>Lastly, we provide peripheral contributions to non-volatile graphene memory devices. While investigating means of improving GNR mobility via dielectric screening, we develop a technique for enhancing hysteresis in graphene devices. This technique is used to demonstrate a preliminary non-volatile graphene device that operates via transition of dielectric screening on and off in the graphene channel.</p>

## REFERENCES

- [1] S. I. Association, "International Technology Roadmap for Semiconductors," 2011.
- [2] D. Edelstein, J. Heidenreich, R. Goldblatt, W. Cote, C. Uzoh, N. Lustig, P. Roper, T. McDevitt, W. Motsiff, A. Simon, J. Dukovic, R. Wachnik, H. Rathore, R. Schulz, L. Su, S. Luce, J. Slattery, and IEEE, "Full copper wiring in a sub-0.25  $\mu\text{m}$  CMOS ULSI technology," *International Electron Devices Meeting - 1997, Technical Digest*, pp. 773-776, 1997.
- [3] R. Murali, K. Brenner, Y. X. Yang, T. Beck, and J. D. Meindl, "Resistivity of graphene nanoribbon interconnects," *IEEE Electron Device Letters*, vol. 30, pp. 611-613, Jun 2009.
- [4] R. Murali, Y. X. Yang, K. Brenner, T. Beck, and J. D. Meindl, "Breakdown current density of graphene nanoribbons," *Applied Physics Letters*, vol. 94, Jun 2009.
- [5] K. Brenner and R. Murali, "Single step, complementary doping of graphene," *Applied Physics Letters*, vol. 96, Feb 2010.
- [6] K. Brenner, Y. X. Yang, and R. Murali, "Edge doping of graphene sheets," *Carbon*, vol. 50, pp. 637-645, Feb 2012.
- [7] K. Brenner and R. Murali, "In situ doping of graphene by exfoliation in a nitrogen ambient," *Applied Physics Letters*, vol. 98, Mar 2011.
- [8] K. Brenner, T. J. Beck, and J. D. Meindl, "Enhancing hysteresis in graphene devices using dielectric screening," *IEEE Electron Device Letters*, vol. 33, pp. 1195-1197, Aug 2012.

- [9] Y. X. Yang, K. Brenner, and R. Murali, "The influence of atmosphere on electrical transport in graphene," *Carbon*, vol. 50, pp. 1727-1733, Apr 2012.
- [10] S. E. Bryan, K. Brenner, Y. X. Yang, R. Murali, and J. D. Meindl, "P-Type electrical transport of chemically doped epitaxial graphene nanoribbons," *IEEE Electron Device Letters*, vol. 33, pp. 866-868, Jun 2012.
- [11] Y. X. Yang, K. Brenner, and R. Murali, "System-level analysis of graphene klein tunneling device," *11th IEEE Conference on Nanotechnology*, pp. 1575-1579, 2011.
- [12] Y. Takigawa, N. Tarumi, M. Shiohara, E. Soda, N. Oda, and S. Ogawa, "Novel air-gap formation technology using Ru barrier metal for Cu interconnects with high reliability and low capacitance," *Japanese Journal of Applied Physics*, vol. 50, Jan 2011.
- [13] X. Gu, T. Nemoto, Y. Tomita, A. Teramoto, R. Kuroda, S. I. Kuroki, K. Kawase, S. Sugawa, and T. Ohmi, "Cu single damascene integration of an organic nonporous ultralow-k fluorocarbon dielectric deposited by microwave-excited plasma-enhanced CVD," *IEEE Transactions on Electron Devices*, vol. 59, pp. 1445-1453, May 2012.
- [14] M. A. Khaderbad, R. Pandharipande, V. Singh, S. Madhu, M. Ravikanth, and V. R. Rao, "Porphyrin self-assembled monolayer as a copper diffusion barrier for advanced CMOS technologies," *IEEE Transactions on Electron Devices*, vol. 59, pp. 1963-1969, Jul 2012.

- [15] C. C. Yang, B. Li, H. Shobha, S. Nguyen, A. Grill, W. Ye, J. AuBuchon, M. Shek, and D. Edelstein, "In situ Co/SiC(N,H) capping layers for Cu/low-k interconnects," *IEEE Electron Device Letters*, vol. 33, pp. 588-590, Apr 2012.
- [16] K. S. Novoselov, A. K. Geim, S. V. Morozov, D. Jiang, Y. Zhang, S. V. Dubonos, I. V. Grigorieva, and A. A. Firsov, "Electric field effect in atomically thin carbon films," *Science*, vol. 306, pp. 666-669, Oct 2004.
- [17] A. Naeemi and J. D. Meindl, "Conductance modeling for graphene nanoribbon (GNR) interconnects," *IEEE Electron Device Letters*, vol. 28, pp. 428-431, May 2007.
- [18] A. K. Geim and K. S. Novoselov, "The rise of graphene," *Nature Materials*, vol. 6, pp. 183-191, Mar 2007.
- [19] J. H. Chen, C. Jang, S. D. Xiao, M. Ishigami, and M. S. Fuhrer, "Intrinsic and extrinsic performance limits of graphene devices on SiO<sub>2</sub>," *Nature Nanotechnology*, vol. 3, pp. 206-209, Apr 2008.
- [20] J. H. Chen, C. Jang, S. Adam, M. S. Fuhrer, E. D. Williams, and M. Ishigami, "Charged-impurity scattering in graphene," *Nature Physics*, vol. 4, pp. 377-381, May 2008.
- [21] J. H. Chen, W. G. Cullen, C. Jang, M. S. Fuhrer, and E. D. Williams, "Defect scattering in graphene," *Physical Review Letters*, vol. 102, Jun 2009.
- [22] P. R. Wallace, "The band theory of graphite," *Physical Review*, vol. 71, pp. 622-634, 1947.
- [23] R. E. Peierls, "Quelques proprietes typiques des corps solides," *Ann. I. H. Poincare*, vol. 5, pp. 177-222, 1935.

- [24] C. Lee, X. D. Wei, J. W. Kysar, and J. Hone, "Measurement of the elastic properties and intrinsic strength of monolayer graphene," *Science*, vol. 321, pp. 385-388, Jul 2008.
- [25] A. A. Balandin, S. Ghosh, W. Z. Bao, I. Calizo, D. Teweldebrhan, F. Miao, and C. N. Lau, "Superior thermal conductivity of single-layer graphene," *Nano Letters*, vol. 8, pp. 902-907, Mar 2008.
- [26] T. R. Nayak, H. Andersen, V. S. Makam, C. Khaw, S. Bae, X. F. Xu, P. L. R. Ee, J. H. Ahn, B. H. Hong, G. Pastorin, and B. Ozyilmaz, "Graphene for controlled and accelerated osteogenic differentiation of human mesenchymal stem cells," *Acs Nano*, vol. 5, pp. 4670-4678, Jun 2011.
- [27] Y. M. Lin, C. Dimitrakopoulos, K. A. Jenkins, D. B. Farmer, H. Y. Chiu, A. Grill, and P. Avouris, "100-GHz transistors from wafer-scale epitaxial graphene," *Science*, vol. 327, pp. 662-662, Feb 2010.
- [28] F. Schedin, A. K. Geim, S. V. Morozov, E. W. Hill, P. Blake, M. I. Katsnelson, and K. S. Novoselov, "Detection of individual gas molecules adsorbed on graphene," *Nature Materials*, vol. 6, pp. 652-655, Sep 2007.
- [29] K. S. Novoselov, A. K. Geim, S. V. Morozov, D. Jiang, M. I. Katsnelson, I. V. Grigorieva, S. V. Dubonos, and A. A. Firsov, "Two-dimensional gas of massless Dirac fermions in graphene," *Nature*, vol. 438, pp. 197-200, Nov 2005.
- [30] M. I. Katsnelson, K. S. Novoselov, and A. K. Geim, "Chiral tunnelling and the Klein paradox in graphene," *Nature Physics*, vol. 2, pp. 620-625, Sep 2006.

- [31] V. V. Cheianov, V. Fal'ko, and B. L. Altshuler, "The focusing of electron flow and a Veselago lens in graphene p-n junctions," *Science*, vol. 315, pp. 1252-1255, Mar 2007.
- [32] P. Avouris, Z. H. Chen, and V. Perebeinos, "Carbon-based electronics," *Nature Nanotechnology*, vol. 2, pp. 605-615, Oct 2007.
- [33] C. H. Park, Y. W. Son, L. Yang, M. L. Cohen, and S. G. Louie, "Electron beam supercollimation in graphene superlattices," *Nano Letters*, vol. 8, pp. 2920-2924, Sep 2008.
- [34] M. Y. Han, B. Ozyilmaz, Y. B. Zhang, and P. Kim, "Energy band-gap engineering of graphene nanoribbons," *Physical Review Letters*, vol. 98, p. 206805, May 2007.
- [35] J. W. Bai, X. Zhong, S. Jiang, Y. Huang, and X. F. Duan, "Graphene nanomesh," *Nature Nanotechnology*, vol. 5, pp. 190-194, Mar 2010.
- [36] K. Nakada, M. Fujita, G. Dresselhaus, and M. S. Dresselhaus, "Edge state in graphene ribbons: Nanometer size effect and edge shape dependence," *Physical Review B*, vol. 54, pp. 17954-17961, Dec 1996.
- [37] R. Balog, B. Jorgensen, L. Nilsson, M. Andersen, E. Rienks, M. Bianchi, M. Fanetti, E. Laegsgaard, A. Baraldi, S. Lizzit, Z. Sljivancanin, F. Besenbacher, B. Hammer, T. G. Pedersen, P. Hofmann, and L. Hornekaer, "Bandgap opening in graphene induced by patterned hydrogen adsorption," *Nature Materials*, vol. 9, pp. 315-319, Apr 2010.
- [38] Y. W. Son, M. L. Cohen, and S. G. Louie, "Half-metallic graphene nanoribbons," *Nature*, vol. 444, pp. 347-349, Nov 2006.

- [39] D. C. Elias, R. R. Nair, T. M. G. Mohiuddin, S. V. Morozov, P. Blake, M. P. Halsall, A. C. Ferrari, D. W. Boukhvalov, M. I. Katsnelson, A. K. Geim, and K. S. Novoselov, "Control of graphene's properties by reversible hydrogenation: evidence for graphane," *Science*, vol. 323, pp. 610-613, Jan 2009.
- [40] T. Ohta, A. Bostwick, T. Seyller, K. Horn, and E. Rotenberg, "Controlling the electronic structure of bilayer graphene," *Science*, vol. 313, pp. 951-954, Aug 2006.
- [41] Y. B. Zhang, T. T. Tang, C. Girit, Z. Hao, M. C. Martin, A. Zettl, M. F. Crommie, Y. R. Shen, and F. Wang, "Direct observation of a widely tunable bandgap in bilayer graphene," *Nature*, vol. 459, pp. 820-823, Jun 2009.
- [42] K. I. Bolotin, K. J. Sikes, Z. Jiang, M. Klima, G. Fudenberg, J. Hone, P. Kim, and H. L. Stormer, "Ultrahigh electron mobility in suspended graphene," *Solid State Communications*, vol. 146, pp. 351-355, Jun 2008.
- [43] G. D. Ruan, Z. Z. Sun, Z. W. Peng, and J. M. Tour, "Growth of graphene from food, insects, and waste," *Acs Nano*, vol. 5, pp. 7601-7607, Sep 2011.
- [44] Y. W. Tan, Y. Zhang, K. Bolotin, Y. Zhao, S. Adam, E. H. Hwang, S. Das Sarma, H. L. Stormer, and P. Kim, "Measurement of scattering rate and minimum conductivity in graphene," *Physical Review Letters*, vol. 99, Dec 2007.
- [45] A. Hashimoto, K. Suenaga, A. Gloter, K. Urita, and S. Iijima, "Direct evidence for atomic defects in graphene layers," *Nature*, vol. 430, pp. 870-873, Aug 2004.
- [46] J. Martin, N. Akerman, G. Ulbricht, T. Lohmann, J. H. Smet, K. Von Klitzing, and A. Yacoby, "Observation of electron-hole puddles in graphene using a



- scanning single-electron transistor," *Nature Physics*, vol. 4, pp. 144-148, Feb 2008.
- [47] Y. B. Zhang, V. W. Brar, C. Girit, A. Zettl, and M. F. Crommie, "Origin of spatial charge inhomogeneity in graphene," *Nature Physics*, vol. 5, pp. 722-726, Oct 2009.
- [48] X. S. Li, W. W. Cai, J. H. An, S. Kim, J. Nah, D. X. Yang, R. Piner, A. Velamakanni, I. Jung, E. Tutuc, S. K. Banerjee, L. Colombo, and R. S. Ruoff, "Large-area synthesis of high-quality and uniform graphene films on copper foils," *Science*, vol. 324, pp. 1312-1314, Jun 2009.
- [49] A. Reina, X. T. Jia, J. Ho, D. Nezich, H. B. Son, V. Bulovic, M. S. Dresselhaus, and J. Kong, "Large area, few-layer graphene films on arbitrary substrates by chemical vapor deposition," *Nano Letters*, vol. 9, pp. 30-35, Jan 2009.
- [50] K. S. Kim, Y. Zhao, H. Jang, S. Y. Lee, J. M. Kim, J. H. Ahn, P. Kim, J. Y. Choi, and B. H. Hong, "Large-scale pattern growth of graphene films for stretchable transparent electrodes," *Nature*, vol. 457, pp. 706-710, Feb 2009.
- [51] Z. Z. Sun, Z. Yan, J. Yao, E. Beitler, Y. Zhu, and J. M. Tour, "Growth of graphene from solid carbon sources," *Nature*, vol. 468, pp. 549-552, Nov 2010.
- [52] S. Amini, J. Garay, G. X. Liu, A. A. Balandin, and R. Abbaschian, "Growth of large-area graphene films from metal-carbon melts," *Journal of Applied Physics*, vol. 108, Nov 2010.
- [53] J. Kwak, J. H. Chu, J. K. Choi, S. D. Park, H. Go, S. Y. Kim, K. Park, S. D. Kim, Y. W. Kim, E. Yoon, S. Kodambaka, and S. Y. Kwon, "Near room-temperature

- synthesis of transfer-free graphene films," *Nature Communications*, vol. 3, Jan 2012.
- [54] A. Ismach, C. Druzgalski, S. Penwell, A. Schwartzberg, M. Zheng, A. Javey, J. Bokor, and Y. G. Zhang, "Direct chemical vapor deposition of graphene on dielectric surfaces," *Nano Letters*, vol. 10, pp. 1542-1548, May 2010.
- [55] S. Bae, H. Kim, Y. Lee, X. F. Xu, J. S. Park, Y. Zheng, J. Balakrishnan, T. Lei, H. R. Kim, Y. I. Song, Y. J. Kim, K. S. Kim, B. Ozyilmaz, J. H. Ahn, B. H. Hong, and S. Iijima, "Roll-to-roll production of 30-inch graphene films for transparent electrodes," *Nature Nanotechnology*, vol. 5, pp. 574-578, Aug 2010.
- [56] C. Berger, Z. M. Song, T. B. Li, X. B. Li, A. Y. Ogbazghi, R. Feng, Z. T. Dai, A. N. Marchenkov, E. H. Conrad, P. N. First, and W. A. de Heer, "Ultrathin epitaxial graphite: 2D electron gas properties and a route toward graphene-based nanoelectronics," *Journal of Physical Chemistry B*, vol. 108, pp. 19912-19916, Dec 2004.
- [57] C. Berger, Z. M. Song, X. B. Li, X. S. Wu, N. Brown, C. Naud, D. Mayou, T. B. Li, J. Hass, A. N. Marchenkov, E. H. Conrad, P. N. First, and W. A. de Heer, "Electronic confinement and coherence in patterned epitaxial graphene," *Science*, vol. 312, pp. 1191-1196, May 2006.
- [58] J. Hass, F. Varchon, J. E. Millan-Otoya, M. Sprinkle, N. Sharma, W. A. De Heer, C. Berger, P. N. First, L. Magaud, and E. H. Conrad, "Why multilayer graphene on 4H-SiC(000(1) $\overline{00}$ ) behaves like a single sheet of graphene," *Physical Review Letters*, vol. 100, Mar 2008.

- [59] S. Stankovich, D. A. Dikin, R. D. Piner, K. A. Kohlhaas, A. Kleinhammes, Y. Jia, Y. Wu, S. T. Nguyen, and R. S. Ruoff, "Synthesis of graphene-based nanosheets via chemical reduction of exfoliated graphite oxide," *Carbon*, vol. 45, pp. 1558-1565, Jun 2007.
- [60] Z. W. Peng, Z. Yan, Z. Z. Sun, and J. M. Tour, "Direct growth of bilayer graphene on SiO<sub>2</sub> substrates by carbon diffusion through nickel," *Acs Nano*, vol. 5, pp. 8241-8247, Oct 2011.
- [61] Y. M. Lin, K. A. Jenkins, A. Valdes-Garcia, J. P. Small, D. B. Farmer, and P. Avouris, "Operation of graphene transistors at gigahertz frequencies," *Nano Letters*, vol. 9, pp. 422-426, Jan 2009.
- [62] L. Liao, Y. C. Lin, M. Q. Bao, R. Cheng, J. W. Bai, Y. A. Liu, Y. Q. Qu, K. L. Wang, Y. Huang, and X. F. Duan, "High-speed graphene transistors with a self-aligned nanowire gate," *Nature*, vol. 467, pp. 305-308, Sep 2010.
- [63] Y. Q. Wu, Y. M. Lin, A. A. Bol, K. A. Jenkins, F. N. Xia, D. B. Farmer, Y. Zhu, and P. Avouris, "High-frequency, scaled graphene transistors on diamond-like carbon," *Nature*, vol. 472, pp. 74-78, Apr 2011.
- [64] Y. M. Lin, A. Valdes-Garcia, S. J. Han, D. B. Farmer, I. Meric, Y. N. Sun, Y. Q. Wu, C. Dimitrakopoulos, A. Grill, P. Avouris, and K. A. Jenkins, "Wafer-scale graphene integrated circuit," *Science*, vol. 332, pp. 1294-1297, Jun 2011.
- [65] X. Y. Chen, D. Akinwande, K. J. Lee, G. F. Close, S. Yasuda, B. C. Paul, S. Fujita, J. Kong, and H. S. P. Wong, "Fully integrated graphene and carbon nanotube interconnects for gigahertz high-speed CMOS electronics," *IEEE Transactions on Electron Devices*, vol. 57, pp. 3137-3143, Nov 2010.

- [66] D. Sarkar, C. A. Xu, H. Li, and K. Banerjee, "High-frequency behavior of graphene-based interconnects-part I: impedance modeling," *IEEE Transactions on Electron Devices*, vol. 58, pp. 843-852, Mar 2011.
- [67] D. Sarkar, C. A. Xu, H. Li, and K. Banerjee, "High-frequency behavior of graphene-based interconnects-part II: impedance analysis and implications for inductor design," *IEEE Transactions on Electron Devices*, vol. 58, pp. 853-859, Mar 2011.
- [68] A. Naeemi and J. D. Meindl, "Compact physics-based circuit models for graphene nanoribbon interconnects," *IEEE Transactions on Electron Devices*, vol. 56, pp. 1822-1833, Sep 2009.
- [69] C. A. Xu, H. Li, and K. Banerjee, "Modeling, analysis, and design of graphene nano-ribbon interconnects," *IEEE Transactions on Electron Devices*, vol. 56, pp. 1567-1578, Aug 2009.
- [70] E. H. Sondheimer, "The mean free path of electrons in metals," *Advances in Physics*, vol. 1, pp. 1-42, 1952.
- [71] A. Ceyhan, A. Naeemi, and IEEE, "Multilevel interconnect networks for the end of the roadmap: conventional Cu/low-k and emerging carbon based interconnects," *2011 IEEE International Interconnect Technology Conference and Materials for Advanced Metallization (Iitc/Mam)*, 2011.
- [72] M. Tsutsui, Y. Taninouchi, S. Kurokawa, and A. Sakai, "Electrical breakdown of short multiwalled carbon nanotubes," *Journal of Applied Physics*, vol. 100, Nov 2006.

- [73] P. C. Collins, M. S. Arnold, and P. Avouris, "Engineering carbon nanotubes and nanotube circuits using electrical breakdown," *Science*, vol. 292, pp. 706-709, Apr 2001.
- [74] Y. X. Yang and R. Murali, "Impact of size effect on graphene nanoribbon transport," *IEEE Electron Device Letters*, vol. 31, pp. 237-239, Mar 2010.
- [75] L. Y. Jiao, X. R. Wang, G. Diankov, H. L. Wang, and H. J. Dai, "Facile synthesis of high-quality graphene nanoribbons," *Nature Nanotechnology*, vol. 5, pp. 321-325, May 2010.
- [76] D. V. Kosynkin, A. L. Higginbotham, A. Sinitskii, J. R. Lomeda, A. Dimiev, B. K. Price, and J. M. Tour, "Longitudinal unzipping of carbon nanotubes to form graphene nanoribbons," *Nature*, vol. 458, pp. 872-U5, Apr 2009.
- [77] X. L. Li, X. R. Wang, L. Zhang, S. W. Lee, and H. J. Dai, "Chemically derived, ultrasmooth graphene nanoribbon semiconductors," *Science*, vol. 319, pp. 1229-1232, Feb 2008.
- [78] P. Blake, E. W. Hill, A. H. C. Neto, K. S. Novoselov, D. Jiang, R. Yang, T. J. Booth, and A. K. Geim, "Making graphene visible," *Applied Physics Letters*, vol. 91, Aug 2007.
- [79] Y. Q. Wu, P. D. Ye, M. A. Capano, Y. Xuan, Y. Sui, M. Qi, J. A. Cooper, T. Shen, D. Pandey, G. Prakash, and R. Reifengerger, "Top-gated graphene field-effect-transistors formed by decomposition of SiC," *Applied Physics Letters*, vol. 92, Mar 2008.

- [80] A. Pachoud, M. Jaiswal, P. K. Ang, K. P. Loh, and B. Ozyilmaz, "Graphene transport at high carrier densities using a polymer electrolyte gate," *Epl*, vol. 92, Oct 2010.
- [81] F. Molitor, A. Jacobsen, C. Stampfer, J. Guttinger, T. Ihn, and K. Ensslin, "Transport gap in side-gated graphene constrictions," *Physical Review B*, vol. 79, Feb 2009.
- [82] Y. C. Lin, C. Y. Lin, and P. W. Chiu, "Controllable graphene N-doping with ammonia plasma," *Applied Physics Letters*, vol. 96, Mar 2010.
- [83] D. C. Wei, Y. Q. Liu, Y. Wang, H. L. Zhang, L. P. Huang, and G. Yu, "Synthesis of N-doped graphene by chemical vapor deposition and its electrical properties," *Nano Letters*, vol. 9, pp. 1752-1758, May 2009.
- [84] D. B. Farmer, R. Golizadeh-Mojarad, V. Perebeinos, Y. M. Lin, G. S. Tulevski, J. C. Tsang, and P. Avouris, "Chemical doping and electron-hole conduction asymmetry in graphene devices," *Nano Letters*, vol. 9, pp. 388-392, Jan 2009.
- [85] K. Pi, K. M. McCreary, W. Bao, W. Han, Y. F. Chiang, Y. Li, S. W. Tsai, C. N. Lau, and R. K. Kawakami, "Electronic doping and scattering by transition metals on graphene," *Physical Review B*, vol. 80, Aug 2009.
- [86] D. B. Farmer, Y. M. Lin, A. Afzali-Ardakani, and P. Avouris, "Behavior of a chemically doped graphene junction," *Applied Physics Letters*, vol. 94, May 2009.
- [87] C. Coletti, C. Riedl, D. S. Lee, B. Krauss, L. Patthey, K. von Klitzing, J. H. Smet, and U. Starke, "Charge neutrality and band-gap tuning of epitaxial graphene on SiC by molecular doping," *Physical Review B*, vol. 81, Jun 2010.

- [88] X. R. Wang, Y. J. Ouyang, X. L. Li, H. L. Wang, J. Guo, and H. J. Dai, "Room-temperature all-semiconducting sub-10-nm graphene nanoribbon field-effect transistors," *Physical Review Letters*, vol. 100, May 2008.
- [89] Q. Shao, G. Liu, D. Teweldebrhan, and A. A. Balandin, "High-temperature quenching of electrical resistance in graphene interconnects," *Applied Physics Letters*, vol. 92, May 2008.
- [90] S. Ghosh, I. Calizo, D. Teweldebrhan, E. P. Pokatilov, D. L. Nika, A. A. Balandin, W. Bao, F. Miao, and C. N. Lau, "Extremely high thermal conductivity of graphene: Prospects for thermal management applications in nanoelectronic circuits," *Applied Physics Letters*, vol. 92, Apr 2008.
- [91] F. Munoz-Rojas, J. Fernandez-Rossier, L. Brey, and J. J. Palacios, "Performance limits of graphene-ribbon field-effect transistors," *Physical Review B*, vol. 77, Jan 2008.
- [92] M. C. Lemme, T. J. Echtermeyer, M. Baus, and H. Kurz, "A graphene field-effect device," *IEEE Electron Device Letters*, vol. 28, pp. 282-284, Apr 2007.
- [93] Z. H. Chen, Y. M. Lin, M. J. Rooks, and P. Avouris, "Graphene nano-ribbon electronics," *Physica E-Low-Dimensional Systems & Nanostructures*, vol. 40, pp. 228-232, Dec 2007.
- [94] B. Huard, N. Stander, J. A. Sulpizio, and D. Goldhaber-Gordon, "Evidence of the role of contacts on the observed electron-hole asymmetry in graphene," *Physical Review B*, vol. 78, Sep 2008.

- [95] C. C. Yang and W. C. Chen, "The structures and properties of hydrogen silsesquioxane (HSQ) films produced by thermal curing," *Journal of Materials Chemistry*, vol. 12, pp. 1138-1141, 2002.
- [96] S. Ryu, M. Y. Han, J. Maultzsch, T. F. Heinz, P. Kim, M. L. Steigerwald, and L. E. Brus, "Reversible basal plane hydrogenation of graphene," *Nano Letters*, vol. 8, pp. 4597-4602, Dec 2008.
- [97] D. Kang, N. Park, J. H. Ko, E. Bae, and W. Park, "Oxygen-induced p-type doping of a long individual single-walled carbon nanotube," *Nanotechnology*, vol. 16, pp. 1048-1052, Aug 2005.
- [98] G. U. Sumanasekera, C. K. W. Adu, S. Fang, and P. C. Eklund, "Effects of gas adsorption and collisions on electrical transport in single-walled carbon nanotubes," *Physical Review Letters*, vol. 85, pp. 1096-1099, Jul 2000.
- [99] F. N. Xia, T. Mueller, R. Golizadeh-Mojarad, M. Freitag, Y. M. Lin, J. Tsang, V. Perebeinos, and P. Avouris, "Photocurrent Imaging and Efficient Photon Detection in a Graphene Transistor," *Nano Letters*, vol. 9, pp. 1039-1044, Mar 2009.
- [100] T. L. J. R. Williams, M. S. Lundstrom, C. M. Marcus, "Gate-controlled guiding of electrons in graphene," *Nature Nanotechnology*, 2011.
- [101] F. M. Zhang, Y. He, and X. Chen, "Guided modes in graphene waveguides," *Applied Physics Letters*, vol. 94, May 2009.
- [102] S. V. Morozov, K. S. Novoselov, M. I. Katsnelson, F. Schedin, D. C. Elias, J. A. Jaszczak, and A. K. Geim, "Giant intrinsic carrier mobilities in graphene and its bilayer," *Physical Review Letters*, vol. 100, Jan 2008.



- [103] E. H. Hwang, S. Adam, and S. Das Sarma, "Carrier transport in two-dimensional graphene layers," *Physical Review Letters*, vol. 98, May 2007.
- [104] A. Das, S. Pisana, B. Chakraborty, S. Piscanec, S. K. Saha, U. V. Waghmare, K. S. Novoselov, H. R. Krishnamurthy, A. K. Geim, A. C. Ferrari, and A. K. Sood, "Monitoring dopants by Raman scattering in an electrochemically top-gated graphene transistor," *Nature Nanotechnology*, vol. 3, pp. 210-215, Apr 2008.
- [105] D. K. Efetov and P. Kim, "Controlling electron-phonon interactions in graphene at ultrahigh carrier densities," *Physical Review Letters*, vol. 105, Dec 2010.
- [106] F. Chen, J. L. Xia, and N. J. Tao, "Ionic screening of charged-impurity scattering in graphene," *Nano Letters*, vol. 9, pp. 1621-1625, Apr 2009.
- [107] T. Fang, A. Konar, H. L. Xing, and D. Jena, "Carrier statistics and quantum capacitance of graphene sheets and ribbons," *Applied Physics Letters*, vol. 91, Aug 2007.
- [108] O. Leenaerts, B. Partoens, and F. M. Peeters, "Adsorption of H<sub>2</sub>O, NH<sub>3</sub>, CO, NO<sub>2</sub>, and NO on graphene: a first-principles study," *Physical Review B*, vol. 77, Mar 2008.
- [109] D. W. Boukhvalov and M. I. Katsnelson, "Chemical functionalization of graphene with defects," *Nano Letters*, vol. 8, pp. 4373-4379, Dec 2008.
- [110] B. Biel, F. Triozon, X. Blase, and S. Roche, "Chemically induced mobility gaps in graphene nanoribbons: a route for upscaling device performances," *Nano Letters*, vol. 9, pp. 2725-2729, Jul 2009.

- [111] F. Cervantes-Sodi, G. Csanyi, S. Piscanec, and A. C. Ferrari, "Edge-functionalized and substitutionally doped graphene nanoribbons: Electronic and spin properties," *Physical Review B*, vol. 77, Apr 2008.
- [112] Z. F. Wang, Q. X. Li, H. X. Zheng, H. Ren, H. B. Su, Q. W. Shi, and J. Chen, "Tuning the electronic structure of graphene nanoribbons through chemical edge modification: A theoretical study," *Physical Review B*, vol. 75, Mar 2007.
- [113] R. Sharma, J. H. Baik, C. J. Perera, and M. S. Strano, "Anomalously large reactivity of single graphene layers and edges toward electron transfer chemistries," *Nano Letters*, vol. 10, pp. 398-405, Feb 2010.
- [114] D. E. Jiang, B. G. Sumpter, and S. Dai, "Unique chemical reactivity of a graphene nanoribbon's zigzag edge," *Journal of Chemical Physics*, vol. 126, Apr 2007.
- [115] X. R. Wang, X. L. Li, L. Zhang, Y. Yoon, P. K. Weber, H. L. Wang, J. Guo, and H. J. Dai, "N-doping of graphene through electrothermal reactions with ammonia," *Science*, vol. 324, pp. 768-771, May 2009.
- [116] H. Lim, J. S. Lee, H. J. Shin, H. S. Shin, and H. C. Choi, "Spatially resolved spontaneous reactivity of diazonium salt on edge and basal plane of graphene without surfactant and its doping effect," *Langmuir*, vol. 26, pp. 12278-12284, Jul 2010.
- [117] D. Estrada, S. Dutta, A. Liao, and E. Pop, "Reduction of hysteresis for carbon nanotube mobility measurements using pulsed characterization," *Nanotechnology*, vol. 21, p. 085702, Feb 2010.

- [118] M. G. Albrecht and C. Blanchette, "Materials issues with thin film hydrogen silsesquioxane low K dielectrics," *Journal of the Electrochemical Society*, vol. 145, pp. 4019-4025, Nov 1998.
- [119] H. J. Lee, E. K. Lin, H. Wang, W. L. Wu, W. Chen, and E. S. Moyer, "Structural comparison of hydrogen silsesquioxane based porous low-k thin films prepared with varying process conditions," *Chemistry of Materials*, vol. 14, pp. 1845-1852, Apr 2002.
- [120] M. J. Loboda, C. M. Grove, and R. F. Schneider, "Properties of a-SiO<sub>x</sub> : H thin films deposited from hydrogen silsesquioxane resins," *Journal of the Electrochemical Society*, vol. 145, pp. 2861-2866, Aug 1998.
- [121] J. S. Arellano, L. M. Molina, A. Rubio, and J. A. Alonso, "Density functional study of adsorption of molecular hydrogen on graphene layers," *Journal of Chemical Physics*, vol. 112, pp. 8114-8119, May 2000.
- [122] R. F. Egerton, P. Li, and M. Malac, "Radiation damage in the TEM and SEM," *Micron*, vol. 35, pp. 399-409, 2004.
- [123] P. M. Ajayan, V. Ravikumar, and J. C. Charlier, "Surface reconstructions and dimensional changes in single-walled carbon nanotubes," *Physical Review Letters*, vol. 81, pp. 1437-1440, Aug 1998.
- [124] R. F. Egerton, F. Wang, and P. A. Crozier, "Beam-induced damage to thin specimens in an intense electron probe," *Microscopy and Microanalysis*, vol. 12, pp. 65-71, Feb 2006.

- [125] Y. Niimi, T. Matsui, H. Kambara, K. Tagami, M. Tsukada, and H. Fukuyama, "Scanning tunneling microscopy and spectroscopy studies of graphite edges," *Applied Surface Science*, vol. 241, pp. 43-48, Feb 28 2005.
- [126] X. W. Sha and B. Jackson, "The location of adsorbed hydrogen in graphite nanostructures," *Journal of the American Chemical Society*, vol. 126, pp. 13095-13099, Oct 2004.
- [127] T. Wassmann, A. P. Seitsonen, A. M. Saitta, M. Lazzeri, and F. Mauri, "Structure, stability, edge states, and aromaticity of graphene ribbons," *Physical Review Letters*, vol. 101, Aug 2008.
- [128] Y. H. Lu, R. Q. Wu, L. Shen, M. Yang, Z. D. Sha, Y. Q. Cai, P. M. He, and Y. P. Feng, "Effects of edge passivation by hydrogen on electronic structure of armchair graphene nanoribbon and band gap engineering," *Applied Physics Letters*, vol. 94, Mar 2009.
- [129] Y. Kobayashi, K. Fukui, T. Enoki, and K. Kusakabe, "Edge state on hydrogen-terminated graphite edges investigated by scanning tunneling microscopy," *Physical Review B*, vol. 73, Mar 2006.
- [130] F. Banhart, "Irradiation effects in carbon nanostructures," *Reports on Progress in Physics*, vol. 62, pp. 1181-1221, 1999.
- [131] H. C. Barshilia, S. Sah, B. R. Mehta, V. D. Vankar, D. K. Avasthi, Jaipal, and G. K. Mehta, "Microstructural modifications in diamond-like carbon thin-films caused by high-energy ion irradiation," *Thin Solid Films*, vol. 258, pp. 123-127, Mar 1995.

- [132] H. X. Zheng and W. Duley, "First-principles study of edge chemical modifications in graphene nanodots," *Physical Review B*, vol. 78, 2008.
- [133] S. E. Stein and R. L. Brown, "Pi-electron properties of large condensed polyaromatic hydrocarbons," *Journal of the American Chemical Society*, vol. 109, pp. 3721-3729, Jun 1987.
- [134] K. Tanaka, S. Yamashita, H. Yamabe, and T. Yamabe, "Electronic-properties of one-dimensional graphite family," *Synthetic Metals*, vol. 17, pp. 143-148, Jan 1987.
- [135] M. Fujita, K. Wakabayashi, K. Nakada, and K. Kusakabe, "Peculiar localized state at zigzag graphite edge," *Journal of the Physical Society of Japan*, vol. 65, pp. 1920-1923, Jul 1996.
- [136] C. O. Girit, J. C. Meyer, R. Erni, M. D. Rossell, C. Kisielowski, L. Yang, C. H. Park, M. F. Crommie, M. L. Cohen, S. G. Louie, and A. Zettl, "Graphene at the edge: stability and dynamics," *Science*, vol. 323, pp. 1705-1708, Mar 2009.
- [137] Y. Niimi, T. Matsui, H. Kambara, K. Tagami, M. Tsukada, and H. Fukuyama, "Scanning tunneling microscopy and spectroscopy of the electronic local density of states of graphite surfaces near monoatomic step edges," *Physical Review B*, vol. 73, Feb 2006.
- [138] Y. Kobayashi, K. Fukui, T. Enoki, K. Kusakabe, and Y. Kaburagi, "Observation of zigzag and armchair edges of graphite using scanning tunneling microscopy and spectroscopy," *Physical Review B*, vol. 71, May 2005.

- [139] K. A. Ritter and J. W. Lyding, "The influence of edge structure on the electronic properties of graphene quantum dots and nanoribbons," *Nature Materials*, vol. 8, pp. 235-242, Mar 2009.
- [140] P. L. Giunta and S. P. Kelty, "Direct observation of graphite layer edge states by scanning tunneling microscopy," *Journal of Chemical Physics*, vol. 114, pp. 1807-1812, Jan 2001.
- [141] A. K. Gupta, T. J. Russin, H. R. Gutierrez, and P. C. Eklund, "Probing Graphene Edges via Raman Scattering," *Acs Nano*, vol. 3, pp. 45-52, Jan 2009.
- [142] G. Giovannetti, P. A. Khomyakov, G. Brocks, V. M. Karpan, J. van den Brink, and P. J. Kelly, "Doping graphene with metal contacts," *Physical Review Letters*, vol. 101, Jul 2008.
- [143] T. Mueller, F. Xia, M. Freitag, J. Tsang, and P. Avouris, "Role of contacts in graphene transistors: a scanning photocurrent study," *Physical Review B*, vol. 79, Jun 2009.
- [144] Y. Y. Shao, S. Zhang, M. H. Engelhard, G. S. Li, G. C. Shao, Y. Wang, J. Liu, I. A. Aksay, and Y. H. Lin, "Nitrogen-doped graphene and its electrochemical applications," *Journal of Materials Chemistry*, vol. 20, pp. 7491-7496, 2010.
- [145] T. Fang, A. Konar, H. Xing, and D. Jena, "Mobility in semiconducting graphene nanoribbons: Phonon, impurity, and edge roughness scattering," *Physical Review B*, vol. 78, Nov 2008.
- [146] Y. J. Ren, S. S. Chen, W. W. Cai, Y. W. Zhu, C. F. Zhu, and R. S. Ruoff, "Controlling the electrical transport properties of graphene by in situ metal deposition," *Applied Physics Letters*, vol. 97, Aug 2010.

- [147] X. C. Dong, D. L. Fu, W. J. Fang, Y. M. Shi, P. Chen, and L. J. Li, "Doping single-layer graphene with aromatic molecules," *Small*, vol. 5, pp. 1422-1426, Jun 2009.
- [148] X. L. Li, H. L. Wang, J. T. Robinson, H. Sanchez, G. Diankov, and H. J. Dai, "Simultaneous nitrogen doping and reduction of graphene oxide," *Journal of the American Chemical Society*, vol. 131, pp. 15939-15944, Nov 2009.
- [149] L. S. Panchokarla, K. S. Subrahmanyam, S. K. Saha, A. Govindaraj, H. R. Krishnamurthy, U. V. Waghmare, and C. N. R. Rao, "Synthesis, structure, and properties of boron- and nitrogen-doped graphene," *Advanced Materials*, vol. 21, pp. 4726-+, Dec 2009.
- [150] A. C. Ferrari, J. C. Meyer, V. Scardaci, C. Casiraghi, M. Lazzeri, F. Mauri, S. Piscanec, D. Jiang, K. S. Novoselov, S. Roth, and A. K. Geim, "Raman spectrum of graphene and graphene layers," *Physical Review Letters*, vol. 97, Nov 2006.
- [151] L. Brey and H. A. Fertig, "Electronic states of graphene nanoribbons studied with the Dirac equation," *Physical Review B*, vol. 73, Jun 2006.
- [152] M. Ezawa, "Peculiar width dependence of the electronic properties of carbon nanoribbons," *Physical Review B*, vol. 73, Jan 2006.
- [153] Y. Miyamoto, K. Nakada, and M. Fujita, "First-principles study of edge states of H-terminated graphitic ribbons," *Physical Review B*, vol. 59, pp. 9858-9861, Apr 1999.
- [154] R. Ramprasad, P. von Allmen, and L. R. C. Fonseca, "Contributions to the work function: A density-functional study of adsorbates at graphene ribbon edges," *Physical Review B*, vol. 60, pp. 6023-6027, Aug 1999.

- [155] P. Koskinen, S. Malola, and H. Hakkinen, "Self-passivating edge reconstructions of graphene," *Physical Review Letters*, vol. 101, Sep 2008.
- [156] P. Koskinen, S. Malola, and H. Hakkinen, "Evidence for graphene edges beyond zigzag and armchair," *Physical Review B*, vol. 80, Aug 2009.
- [157] B. Huang, M. Liu, N. H. Su, J. Wu, W. H. Duan, B. L. Gu, and F. Liu, "Quantum manifestations of graphene edge stress and edge instability: a first-principles study," *Physical Review Letters*, vol. 102, Apr 2009.
- [158] L. L. Song, X. H. Zheng, R. L. Wang, and Z. Zeng, "Dangling bond states, edge magnetism, and edge reconstruction in pristine and B/N-terminated zigzag graphene nanoribbons," *Journal of Physical Chemistry C*, vol. 114, pp. 12145-12150, Jul 2010.
- [159] S. F. Huang, K. Terakura, T. Ozaki, T. Ikeda, M. Boero, M. Oshima, J. Ozaki, and S. Miyata, "First-principles calculation of the electronic properties of graphene clusters doped with nitrogen and boron: analysis of catalytic activity for the oxygen reduction reaction," *Physical Review B*, vol. 80, Dec 2009.
- [160] S. S. Yu, W. T. Zheng, Q. B. Wen, and Q. Jiang, "First principle calculations of the electronic properties of nitrogen-doped carbon nanoribbons with zigzag edges," *Carbon*, vol. 46, pp. 537-543, Mar 2008.
- [161] G. M. Rutter, J. N. Crain, N. P. Guisinger, T. Li, P. N. First, and J. A. Stroscio, "Scattering and interference in epitaxial graphene," *Science*, vol. 317, pp. 219-222, Jul 2007.
- [162] J. R. Hahn and H. Kang, "Vacancy and interstitial defects at graphite surfaces: scanning tunneling microscopic study of the structure, electronic property, and



- yield for ion-induced defect creation," *Physical Review B*, vol. 60, pp. 6007-6017, Aug 1999.
- [163] A. J. Stone and D. J. Wales, "Theoretical-studies of icosahedral c60 and some related species," *Chemical Physics Letters*, vol. 128, pp. 501-503, Aug 1986.
  - [164] C. P. Ewels, R. H. Telling, A. A. El-Barbary, M. I. Heggie, and P. R. Briddon, "Metastable Frenkel pair defect in graphite: source of Wigner energy?," *Physical Review Letters*, vol. 91, Jul 2003.
  - [165] F. Chen, J. L. Xia, D. K. Ferry, and N. J. Tao, "Dielectric screening enhanced performance in graphene FET," *Nano Letters*, vol. 9, pp. 2571-2574, Jul 2009.
  - [166] L. A. Ponomarenko, R. Yang, T. M. Mohiuddin, M. I. Katsnelson, K. S. Novoselov, S. V. Morozov, A. A. Zhukov, F. Schedin, E. W. Hill, and A. K. Geim, "Effect of a high-kappa environment on charge carrier mobility in graphene," *Physical Review Letters*, vol. 102, May 2009.
  - [167] J. Kong, N. R. Franklin, C. W. Zhou, M. G. Chapline, S. Peng, K. J. Cho, and H. J. Dai, "Nanotube molecular wires as chemical sensors," *Science*, vol. 287, pp. 622-625, Jan 2000.
  - [168] K. Yano, T. Ishii, T. Hashimoto, T. Kobayashi, F. Murai, and K. Seki, "Room-temperature single-electron memory," *IEEE Transactions on Electron Devices*, vol. 41, pp. 1628-1638, Sep 1994.
  - [169] M. S. Fuhrer, B. M. Kim, T. Durkop, and T. Brintlinger, "High-mobility nanotube transistor memory," *Nano Letters*, vol. 2, pp. 755-759, Jul 2002.
  - [170] R. H. Baughman, A. A. Zakhidov, and W. A. de Heer, "Carbon nanotubes - the route toward applications," *Science*, vol. 297, pp. 787-792, Aug 2002.

- [171] L. T. Zhuravlev, "The surface chemistry of amorphous silica. Zhuravlev model," *Colloids and Surfaces a-Physicochemical and Engineering Aspects*, vol. 173, pp. 1-38, Nov 10 2000.
- [172] A. Gupta, G. Chen, P. Joshi, S. Tadigadapa, and P. C. Eklund, "Raman scattering from high-frequency phonons in supported n-graphene layer films," *Nano Letters*, vol. 6, pp. 2667-2673, Dec 2006.
- [173] S. Adam, E. H. Hwang, V. M. Galitski, and S. Das Sarma, "A self-consistent theory for graphene transport," *Proceedings of the National Academy of Sciences of the United States of America*, vol. 104, pp. 18392-18397, 2007.
- [174] W. Kim, A. Javey, O. Vermesh, O. Wang, Y. M. Li, and H. J. Dai, "Hysteresis caused by water molecules in carbon nanotube field-effect transistors," *Nano Letters*, vol. 3, pp. 193-198, Feb 2003.
- [175] A. Robert-Peillard and S. V. Rotkin, "Modeling hysteresis phenomena in nanotube field-effect transistors," *IEEE Transactions on Nanotechnology*, vol. 4, pp. 284-288, Mar 2005.
- [176] S. Kar, A. Vijayaraghavan, C. Soldano, S. Talapatra, R. Vajtai, O. Nalamasu, and P. M. Ajayan, "Quantitative analysis of hysteresis in carbon nanotube field-effect devices," *Applied Physics Letters*, vol. 89, p. 132118, Sep 2006.
- [177] J. S. Lee, S. Ryu, K. Yoo, I. S. Choi, W. S. Yun, and J. Kim, "Origin of gate hysteresis in carbon nanotube field-effect transistors," *Journal of Physical Chemistry C*, vol. 111, pp. 12504-12507, Aug 2007.

- [178] D. J. Dimaria, E. Cartier, and D. Arnold, "Impact ionization, trap creation, degradation, and breakdown in silicon dioxide films on silicon," *Journal of Applied Physics*, vol. 73, pp. 3367-3384, Apr 1 1993.